

Active Interrogation using Photofission Technique for Nuclear Materials Control and Accountability

Fuel Cycle Research and Development

Haori Yang
Oregon State University

Dan Vega, Federal POC
Mike Miller, Technical POC

FINAL REPORT

Project Title: Active Interrogation using Photofission Technique for Nuclear Materials Control and Accountability

Covering Period: November, 2011 - November, 2015

Contract Number: 120873

Date of Report: March 11, 2016

Principal Investigator: Haori Yang, haori.yang@oregonstate.edu

Co-PI: Daren Norman, daren.norman@inl.gov
Dante Nakazawa, dante.nakazawa@canberra.com

Submitted by:

Haori Yang, Ph.D.

School of Nuclear Science and Engineering

Oregon State University

Prepared by: Xianfei Wen, Haori Yang

Abstract

Innovative systems with increased sensitivity and resolution are in great demand to detect diversion and to prevent misuse in support of nuclear materials management for the U.S. fuel cycle. Nuclear fission is the most important multiplicative process involved in non-destructive active interrogation. This process produces the most easily recognizable signature for nuclear materials. In addition to thermal or high-energy neutrons, high-energy gamma rays can also excite a nucleus and cause fission through a process known as photofission. Electron linear accelerators (linac) are widely used as the interrogating photon sources for inspection methods involving photofission technique. After photofission reactions, prompt signals are much stronger than the delayed signals, but it is difficult to quantify them in practical measurements. Delayed signals are easily distinguishable from the interrogating radiation. linac-based, advanced inspection techniques utilizing the delayed signals after photofission have been extensively studied for homeland security applications. Previous research also showed that a unique delayed gamma ray energy spectrum exists for each fissionable isotope.

In this work, high-energy delayed γ -rays were demonstrated to be signatures for detection, identification, and quantification of special nuclear materials. Such γ -rays were measured in between linac pulses using independent data acquisition systems. A list-mode system was developed to measure low-energy delayed γ -rays after irradiation. Photofission product yields of ^{238}U and ^{239}Pu were determined based on the measured delayed γ -ray spectra. The differential yields of delayed γ -rays were also proven to be able to discriminate nuclear from non-nuclear materials. The measurement outcomes were compared with Monte Carlo simulation results. It was demonstrated that the current available codes have capabilities and limitations in the simulation of photofission process. A two-fold approach was used to address the high-rate challenge in used nuclear fuel assay based on photofission technique. First, a standard HPGe preamplifier was modified to improve its capabilities in high-rate pulsed photofission environment. Second, advanced pulse processing algorithms were shown to greatly improve throughput rate without large sacrifice in energy resolution at ultra-high input count rate. Two customized gamma spectroscopy systems were also developed in real-time on FPGAs. They were shown to have promising performance matching available commercial units.

TABLE OF CONTENTS

1 Literature review	1
1.1 Passive and active non-destructive techniques.....	1
1.2 Differential yields of delayed signatures.....	3
1.3 Photofission product yields	4
1.4 Monte Carlo simulation of photofission process.....	5
1.5 High-rate challenges in pulsed photofission environment	6
1.6 Real-time signal processing on FPGAs.....	7
2 Measurement of delayed γ -rays from photofission.....	8
2.1 Initial Test at Idaho National Laboratory	8
2.1.1 Equipment and experimental setup.....	8
2.1.2 Interlace mode measurement	10
2.1.3 Delayed gamma spectrum measured in between linac pulses	11
2.1.4 High-speed digitization system	12
2.1.5 Conclusions	14
2.2 Energy spectra and differential yields of delayed γ -rays	14
2.2.1 Equipment and experimental setup.....	14
2.2.2 Delayed fission gamma energy spectra measured with a Canberra LYNX	16
2.2.3 Delayed fission gamma spectra measured with a Fast ComTec list-mode system	17
2.2.4 Delayed fission gamma spectra measured with a customized high-speed digitizer	19
2.2.5 Spectra comparison.....	20
2.2.6 Differential yields measurements with the liquid scintillator.....	22
2.3 Photofission product yields of ^{238}U and ^{239}Pu	24
2.3.1 Experimental setup	24
2.3.2 Photofission product yields measured based on the high-energy delayed γ -rays spectra	26
2.3.3 Development of the list-mode system	29
2.3.4 Photofission product yields measured using the list-mode system	30
3 Monte Carlo simulation of photofission process	36
3.1 Simulation of delayed γ -rays from photofission using MCNPX 2.7.0	36
3.1.1 Embedded sources	36
3.1.2 Tally tagging.....	37
3.1.3 LCA	38
3.1.4 Description of theMCNP input file	38
3.1.5 Comaprison with the delayed γ -ray spectra measured in between linac pulse.....	39
3.1.6 Comaprison with the delayed γ -ray spectra measured after irradiation	41
3.1.7 Comparison between the delayed γ -rays spectra published by P. Sibczynski et al. and simulated results	46
3.2 Simulation of delayed γ -rays from photofission using FLUKA	48
4 High-throughput spectroscopy system for high-rate applications	52
4.1 Modifications to the HPGe preamplifier	52
4.1.1 Modifications to the feedback resistor.....	52

4.1.2 Modification to the tail time	55
4.1.3 Energy resolution after the modifications	57
4.1.4 Conclusions	59
4.2 Advanced pulse processing algorithms	60
4.2.1 Template-matching algorithm	60
4.2.1.1 Discussion of the algorithm	60
4.2.1.2 Implementation on signals from a NaI detector	61
4.2.1.3 Implementation on signals from a silicon drift detector	63
4.2.1.4 Implementation on signals from a HPGe detector	64
4.2.1.5 Conclusions	66
4.2.2 De-randomization technique	66
4.2.2.1 Deconvolution of pulses from HPGe preamplifier	66
4.2.2.2 Digital synthesis of exponential signals	69
4.2.2.3 The effect of the deconvolution and synthesis on energy resolution	70
4.2.2.4 The impact of the background noise on energy resolution	71
4.2.2.5 Implementation of the algorithm on high-rate HPGe data	71
4.2.3 Kalman filtering	73
4.2.3.1 Savitzky-Golay and Kalman filters	73
4.2.3.2 State space model for preamplifier signal	77
4.2.3.3 Energy spectra reconstructed using the Kalman filtering method	78
4.2.4 Time-variant trapezoidal filtering	80
5 Digital gamma spectroscopy system development on FPGAs	84
5.1 National Instruments PXIe-7966R	84
5.1.1 Hardware description	84
5.1.2 Design procedures	85
5.1.3 Results and discussion	87
5.2 Xilinx ML605 evaluation kit	89
5.2.1 Design flow	89
5.2.2 Results and discussion	93
6 Conclusions	95
References	97
Appendices	99
A Publications and Presentations	99

LIST OF FIGURES

Figure 1.1 Mass distributions of fission products from thermal neutrons induced fission of ^{233}U , ^{235}U , and ^{239}Pu [17].	3
Figure 1.2 Energy spectra reconstructed using the traditional and time-variant trapezoidal filtering methods at input count rate of 1.03×10^6 cps [29].	6
Figure 2.1 Varitron linear accelerator used in the initial test.	8
Figure 2.2 HPGe detectors used in the initial test.	9
Figure 2.3 High speed digitization system based NI PXIe-5122.	9
Figure 2.4 Experimental setup of the initial test.	10
Figure 2.5 Spectra measured using the interlace mode.	10
Figure 2.6 Measurement in between linac pulses.	11
Figure 2.7 Spectra measured in between linac pulses.	12
Figure 2.8 LABVIEW interface used to control the data acquisition process.	13
Figure 2.9 HPGe preamplifier output showing the saturation.	13
Figure 2.10 The 25-MeV linac at IAC.	14
Figure 2.11 The HPGe detectors used in the test at IAC.	15
Figure 2.12 The boron-loaded liquid scintillator EJ-339A.	15
Figure 2.13 A picture of the experimental setup.	16
Figure 2.14 The high-speed data acquisition system.	16
Figure 2.15 Delayed γ -ray spectra measured from photofission of DU.	17
Figure 2.16 Delayed γ -ray spectra measured from photofission of ^{239}Pu .	17
Figure 2.17 Delayed γ -ray spectra acquired using gate time of 10 ms, 20 ms, and 30 ms (DU).	18
Figure 2.18 Delayed γ -ray spectra acquired using gate time of 10 ms, 20 ms, and 30 ms (^{239}Pu).	18
Figure 2.19 Delayed γ -ray spectra acquired during irradiation and after irradiation (DU).	19
Figure 2.20 Delayed γ -ray spectra acquired during irradiation and after irradiation (^{232}Th).	19
Figure 2.21 Energy spectrum measured with the high-speed digitizer (calibration source).	20
Figure 2.22 Energy spectrum measured with the high-speed digitizer (^{232}Th).	20
Figure 2.23 Delayed γ -ray spectra measured with the Canberra LYNX and the Fast ComTec list-mode system (DU, 0.2 MeV-4.0 MeV).	21
Figure 2.24 Delayed γ -ray spectra measured with the Canberra LYNX and the Fast ComTec list-mode system (DU, 0.2 MeV-2.0 MeV).	21
Figure 2.25 Delayed γ -ray spectra measured with the Canberra LYNX and the Fast ComTec list-mode system (^{232}Th).	22
Figure 2.26 Signals acquired in between linac pulses (DU, ^{232}Th , lead).	23
Figure 2.27 Illustration of threshold value choice.	23
Figure 2.28 Differential yields of delayed γ -rays from nuclear and non-nuclear materials.	24
Figure 2.29 Experimental setup for the testing campaign at IAC.	25
Figure 2.30 A block diagram of the data-acquisition systems.	26
Figure 2.31 Delayed γ -ray spectra measured with the Canberra Lynx system (DU, HEU and Pu).	27
Figure 2.32 Delayed γ -ray spectra measured with the Canberra Lynx system (2.6 MeV-3.2 MeV).	28
Figure 2.33 Delayed γ -ray spectra measured with the Canberra Lynx system (2.6 MeV-3.2 MeV).	28

Figure 2.34 Delayed γ -ray spectra measured with the Canberra Lynx system (3.9 MeV-4.5 MeV).	28
Figure 2.35 Measured delayed gamma spectra with the list-mode system (0.2 MeV-0.5 MeV, Pu).	31
Figure 2.36 Measured delayed gamma spectra with the list-mode system (0.5 MeV-0.9 MeV, Pu).	31
Figure 2.37 Measured delayed gamma spectra with the list-mode system (0.9 MeV-1.5 MeV, Pu).	32
Figure 2.38 Measured delayed gamma spectra with the list-mode system (1.5 MeV-2.2 MeV, Pu).	32
Figure 2.39 Measured delayed gamma spectra with the list-mode system (0.3 MeV-1.0 MeV, DU).	33
Figure 2.40 Measured delayed gamma spectra with the list-mode system (1.0 MeV-1.9 MeV, DU).	33
Figure 2.41 Measured delayed gamma spectra with the list-mode system (2.0 MeV-2.7 MeV, DU).	34
Figure 2.42 Measured delayed gamma spectra with the list-mode system (2.8 MeV-4.2 MeV, DU).	34
Figure 3.1 Examples of tally tagging in MCNPX 2.7.0[31].	37
Figure 3.2 Comparison between the measured delayed gamma spectra and simulated results (2.6 MeV-3.5 MeV, ^{238}U).	39
Figure 3.3 Comparison between the measured delayed gamma spectra and simulated results (3.5 MeV-5.0 MeV, ^{238}U).	40
Figure 3.4 Comparison between measured and simulated delayed gamma spectra (0.6 MeV-0.9 MeV, ^{238}U).	41
Figure 3.5 Comparison between measured and simulated delayed gamma spectra (0.9 MeV-1.2 MeV, ^{238}U).	41
Figure 3.6 Comparison between measured and simulated delayed gamma spectra (1.2 MeV-1.5 MeV, ^{238}U).	42
Figure 3.7 Comparison between measured and simulated delayed gamma spectra (1.5 MeV-1.8 MeV, ^{238}U).	42
Figure 3.8 Comparison between measured and simulated delayed gamma spectra (1.8 MeV-2.1 MeV, ^{238}U).	42
Figure 3.9 Comparison between measured and simulated delayed gamma spectra (2.1 MeV-2.6 MeV, ^{238}U).	43
Figure 3.10 Comparison between measured and simulated delayed gamma spectra (2.6 MeV-3.1 MeV, ^{238}U).	43
Figure 3.11 Comparison between measured and simulated delayed gamma spectra (3.1 MeV-3.6 MeV, ^{238}U).	43
Figure 3.12 Comparison between measured and simulated delayed gamma spectra (3.6 MeV-4.5 MeV, ^{238}U).	44
Figure 3.13 Comparison between measured and simulated delayed gamma spectra (0.6 MeV-0.9 MeV, ^{239}Pu).	44
Figure 3.14 Comparison between measured and simulated delayed gamma spectra (0.9 MeV-1.2 MeV, ^{239}Pu).	44

Figure 3.15 Comparison between measured and simulated delayed gamma spectra (1.2 MeV-1.5 MeV, ^{239}Pu).....	45
Figure 3.16 Comparison between measured and simulated delayed gamma spectra (1.5 MeV-1.8 MeV, ^{239}Pu).....	45
Figure 3.17 Comparison between measured and simulated delayed gamma spectra (1.8 MeV-2.1 MeV, ^{239}Pu).....	45
Figure 3.18 Comparison between measured and simulated delayed gamma spectra (2.1 MeV-2.7 MeV, ^{239}Pu).....	46
Figure 3.19 Comparison between the delayed γ -ray spectra published by P. Sibczynski et al. and simulation results (0.3 MeV-0.9 MeV, HEU).....	46
Figure 3.20 Comparison between the delayed γ -ray spectra published by P. Sibczynski et al. and simulation results (0.9 MeV-1.5 MeV, HEU).....	47
Figure 3.21 Comparison between the delayed γ -ray spectra published by P. Sibczynski et al. and simulation results (1.5 MeV-2.1 MeV, HEU).....	47
Figure 3.22 Comparison between the delayed γ -ray spectra published by P. Sibczynski et al. and simulation results (2.1 MeV-2.7 MeV, HEU).....	47
Figure 3.23 Comparison between the delayed γ -ray spectra published by P. Sibczynski et al. and simulation results (2.7 MeV-3.3 MeV, HEU).....	48
Figure 3.24 Comparison between the delayed γ -ray spectra published by P. Sibczynski et al. and simulation results (3.3 MeV-4.2 MeV, HEU).....	48
Figure 3.25 Beam description in the FLUKA simulation.....	49
Figure 3.26 Geometry description in the FLUKA simulation.....	50
Figure 3.27 Material description in the FLUKA simulation.....	50
Figure 3.28 Photonuclear physics description in the FLUKA simulation.....	50
Figure 3.29 Tally description in the FLUKA simulation.....	51
Figure 3.30 Simulated delayed gamma spectrum from photofission of ^{238}U using FLUKA.....	51
Figure 4.1 The standard and modified preamplifiers.....	53
Figure 4.2 Simulated saturation times of the modified and standard preamplifiers with LTspice.....	54
Figure 4.3 Measured signals from both the modified and standard preamplifiers at a photofission environment.....	55
Figure 4.4 Comparison between signal waveforms measured with NI PXIe-5122.....	56
Figure 4.5 The effect of reduced tail time on baseline shift simulated in LTSpice.....	56
Figure 4.6 Illustration of the time and energy signal shaped in parallel in the trapezoidal filtering.....	58
Figure 4.7 Distribution of charge collection time at input count rate of 20 kcps.....	58
Figure 4.8 Energy resolution versus rise time in the trapezoidal filtering (flat top time was fixed at 0.8 μs).....	59
Figure 4.9 Energy spectra reconstructed at optimal rise times (flat top time was fixed at 0.8 μs).....	59
Figure 4.10 Application of the template-matching algorithm in simulated data.....	61
Figure 4.11 The anode output signal and template.....	62
Figure 4.12 Comparison between energy spectra measured with the Canberra Lynx system and reconstructed with the template-matching algorithm.....	62
Figure 4.13 Energy spectra at different Input Count Rates (ICR) with the template-matching algorithm.....	63

Figure 4.14 Comparison between the template-matching algorithm and the trapezoidal filter (Output Count Rate vs Input Count Rate).....	64
Figure 4.15 Comparison between the template-matching algorithm and the trapezoidal filter (FWHM vs Input Count Rate).	64
Figure 4.16 Verification of the reconstructed signal from preamplifier.	65
Figure 4.17 Energy spectra reconstructed with the template-matching algorithm.	65
Figure 4.18 A block diagram of the functionality of a typical RC-feedback commercial preamplifier unit.....	67
Figure 4.19 (a) A schematic drawing of a preamplifier with RC-feedback, (b) An equivalent presentation of the preamplifier.	67
Figure 4.20 The deconvolution of pulses from an HPGe preamplifier.....	69
Figure 4.21 Digital synthesis of exponential pulses from the detector current signals.	70
Figure 4.22 Energy spectrum reconstructed using the algorithm based on the de-randomization method (ICR=100 kcps).....	73
Figure 4.23 Energy spectrum reconstructed using the de-randomization method (ICR=300 kcps).	73
Figure 4.24 Comparison of a noisy current signal before and after Savitzky–Golay smoothing.	75
Figure 4.25 Illustration of the Kalman filtering (prediction and correction)	76
Figure 4.26 Preamplifier output and indicator signal (The indicator signal in the figure was scaled up by 5.)	79
Figure 4.27 Noisy current signal after the filtering and smoothing.....	79
Figure 4.28 Energy spectrum reconstructed using the advanced digital pulse processing algorithm (ICR =100 kcps).....	79
Figure 4.29 Energy spectrum reconstructed using the advanced digital pulse processing algorithm (ICR =300 kcps).	80
Figure 4.30 Trapezoidal filtering using different rise times (ICR=300 kcps).	81
Figure 4.31 Energy spectrum reconstructed using the time-variant trapezoidal filtering method (ICR=100 kcps).....	82
Figure 4.32 Energy spectrum reconstructed using the time-variant trapezoidal filtering method (ICR=300 kcps).....	82
Figure 5.1 Hardware for the development of customized digital gamma spectroscopy system... ..	84
Figure 5.2 The block diagram of the customized digital γ -ray spectroscopy.	86
Figure 5.3 A LabVIEW graphical user interface for the customized γ -ray spectroscopy.	86
Figure 5.4 Comparison of the ^{137}Cs spectra measured with the Canberra Lynx system and the customized γ -ray spectroscopy (1 μC).....	87
Figure 5.5 The ^{137}Cs spectra measured with the customized γ -ray spectroscopy (5 μC).	87
Figure 5.6 Energy spectrum measured with the customized system (HPGe detector).....	88
Figure 5.7 Energy spectra measured with the customized γ -ray spectroscopy developed on an HPGe platform (^{152}Eu).	88
Figure 5.8 Hardware ML605 evaluation kit and FMC151 for the FPGA design.	89
Figure 5.9 An example of constellation created with the StellarIP tool.	90
Figure 5.10 Illustration of the way the stars of a constellation communicate.	90
Figure 5.11 An example of ISE project generated using the StellarIP tool.	92
Figure 5.12 A simulink model for the traditional trapezoidal filtering.....	93
Figure 5.13 The traditional trapezoidal shaping on the Virtex-6 FPGA in real-time.	93

Figure 5.14 Energy spectrum measured with the FPGA platform based on the ML605 evaluation board and FMC 151.	94
---	----

LIST OF TABLES

Table 1.1 Delayed neutron fractions for various nuclides [20].	4
Table 2.1 Measured peak ratios for the DU, HEU and Pu samples.....	27
Table 2.2 Measured photofission product yields of ^{238}U based on high-energy delayed γ -rays. .	29
Table 2.3 Measured photofission product yields of ^{239}Pu using the list-mode system.....	32
Table 2.4 Measured photofission product yields of ^{238}U using the list-mode system.	34
Table 3.1 Efficiency corrected intensities relative to the 3287.6 keV peak.	40
Table 4.1 Comparison between the template-matching algorithm and the trapezoidal filter (HPGe data).....	65
Table 4.2 Energy resolution vs rise time (Input count rate =100 kcps).....	81
Table 4.3 Energy resolution vs rise time (Input count rate =300 kcps).....	81
Table 4.4 Comparison between the traditional trapezoidal filtering and time-variant trapezoidal filtering.....	83
Table 5.1 The parameters of the NI FPGA module PXIe-7966R.....	85
Table 5.2 The parameters of the NI adapter module 5761.	85

1 Literature review

1.1 Passive and active non-destructive techniques

In homeland security and nuclear safeguards applications, there is an urgent need to find accurate, efficient, and practical ways to stop smuggling of special nuclear materials [1]. Non-invasive methods to detect and identify nuclear materials are of great interest to both domestic and international nuclear safeguards communities [2-3]. Although nuclear materials of interest naturally emit neutrons and/or γ -rays, the intensities of such spontaneous radiation are normally low and the energies of the γ -rays are fairly low in most cases [4]. Furthermore, in homeland security applications, it is prudent to assume that the materials are well shielded to circumvent passive detection. Accurate detection and quantification of well-shielded nuclear materials using passive techniques is almost impossible. Active interrogation techniques based on measurement of high-energy γ -rays or neutrons have been identified as an effective approach [5-7]. Such active techniques rely on neutrons or high-energy photons to induce nuclear reactions in the object under inspection. Unique signatures following induced fission (prompt neutrons, prompt γ -rays, delayed neutrons, delayed γ -rays) are then utilized as the basis for detection, identification, and quantification of nuclear materials [8-11]. On average, two fission products are produced in each fission reaction. Two to three prompt neutrons and approximately eight prompt γ -rays are emitted. These radiations are emitted within 10^{-15} s from the time of fission. The fission products are usually produced in unstable states and have excess neutrons. They continue to generate another six to seven γ -rays and approximately 0.01 to 0.02 neutrons per fission to reach stable states [12]. Although intensities of prompt radiation signals are much stronger, most active interrogation techniques rely on the delayed signals to avoid large interference from the probing radiation. Delayed neutrons emitted by neutron-rich fission products are a well-established, reliable and unique signature for nuclear materials [13]. However, they can be easily shielded by hydrogenous materials and their yield is fairly low. In addition to delayed neutrons, delayed γ -rays are emitted during the β -decay of many fission products. Delayed γ -rays have some advantages over the delayed neutron. First, the intensity of high-energy delayed γ -rays ($E_\gamma > 3$ MeV) is much stronger than that of delayed neutrons. Second, high-energy γ -rays are highly penetrating. They typically undergo 10-100 times less attenuation than delayed neutrons in hydrogenous materials. Third, emission of intense high-energy delayed γ -rays is unique for nuclear materials. They are not usually observed after the irradiation of benign materials using low-energy photon source, nor are they produced in significant amounts by neutron activation in surrounding materials when neutron energy is less than 10 MeV. Thus, delayed γ -rays and delayed neutrons can complement each other to achieve the greatest sensitivity and accuracy. It is worth noticing that the high-energy neutrons generated by the relative high-energy (e.g. 22 MeV) bremsstrahlung x-rays can activate major nuclides like ^{16}O and some minor nuclides present in common materials producing gamma rays with energies and time constants similar to the delayed γ -rays. The impact of secondary neutrons on measurement of delayed γ -rays from fission reactions can be limited by carefully designing experimental setup and shielding. For example, one way to address this issue is to start the

measurement only after the shut-off of the interrogation source for tens of milliseconds to avoid the interference from neutron-capture γ -rays and probing source. The measurement can be achieved by the use of a gate signal.

When high-energy photons are used as the interrogating source, photofission reactions are induced uniquely in nuclear materials. Photofission products are normally produced in their excited energy states and de-excite to lower energy levels by emitting delayed neutrons and/or γ -rays. In contrast, neutrons can be produced in both fissionable and non-fissionable materials through photonuclear reactions. These neutrons are moderated and eventually absorbed by surrounding materials. Delayed γ -rays will be emitted during this absorption process as well. Thus, for any measurement technique based on delayed γ -rays detection, it is necessary to distinguish delayed fission γ -rays from those created by other nuclear reactions. Detection of delayed γ -rays with energies larger than 3 MeV has been proposed, investigated, and implemented as a method for detection of fissionable materials using neutrons or photons. Furthermore, it is important to note that unique γ -ray energy distributions exist for each fissionable isotope [14-15], which can be used to differentiate nuclear materials. Delayed γ -ray energy spectra are rich and complex, but it is possible to resolve individual spectral lines with high-resolution detectors, such as High-Purity Germanium (HPGe) detectors. The relative intensities of certain lines vary significantly between nuclides due to the difference in fission fragment mass distributions, as shown in Figure 1.1 Based on spectral line intensities, discrimination ratios on the order of 3 have been reported between ^{235}U , ^{239}Pu , and ^{238}U . Some of the previous work involving the detection of delayed fission γ -rays focused on a so-called “interlace” inspection cycle, consisting of an irradiation period, followed by a cooling period of a few seconds to minutes, and a counting period of minutes to hours [8]. As a result, the measured delayed γ -ray spectra are normally dominated by fission products with medium to long half-lives lasting tens of seconds to minutes or even hours. However, the authors and researchers from Idaho Accelerator Center (IAC) as well as others, e.g. J. Stevenson, have independently demonstrated the capability to measure delayed fission γ -rays in between linac pulses [26, 41-42]. Regarding delayed γ -ray energy spectroscopy, a research group from the University of Michigan focused on delayed γ -rays with energies below 2 MeV [16]. Multiple fission products were identified based on discrete γ -ray lines in this region. Using known fission yield data, fission reaction rate in the sample was predicted. Based on the efficiency-corrected line ratio of the 186 keV and the 1001 keV lines, the sample was confirmed to be a depleted uranium sample. The intensity ratios between delayed γ -ray peaks below 1.5 MeV were thoroughly measured and studied previously.

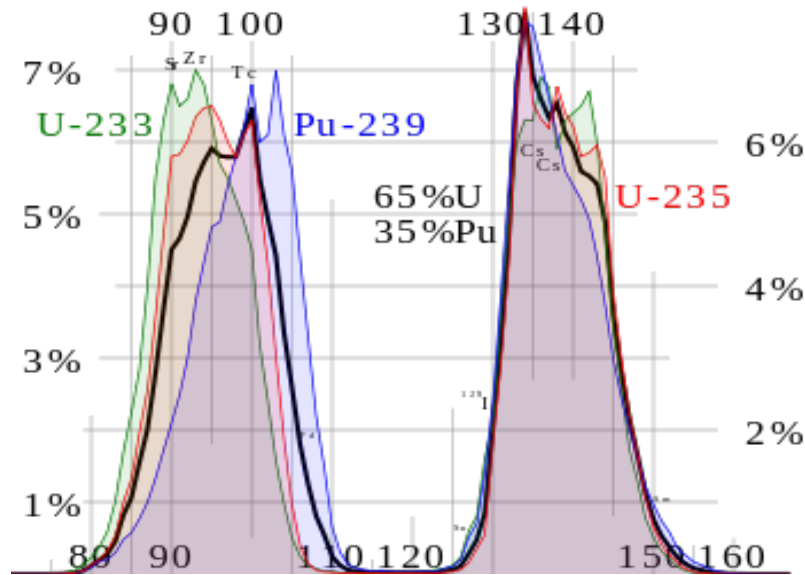


Figure 1.1 Mass distributions of fission products from thermal neutrons induced fission of ^{233}U , ^{235}U , and ^{239}Pu [17].

1.2 Differential yields of delayed signatures

In nuclear safeguards and homeland security applications, it is also of interest to use the differential yields of delayed neutrons or delayed γ -rays to discriminate between nuclear and non-nuclear materials in homeland security applications [18]. In a measurement based on this feature, energy resolution of the detector is not critical. However, the detector response time should be as fast as possible to maximize the throughput rate and minimize the recovery time immediately after each linac pulse. Boron-loaded liquid scintillation detectors are good candidates for this type of application. In contrast, detectors with superior energy resolution, such as HPGe detectors, are required for isotope identification based on spectroscopy measurement of delayed γ -rays. These two different types of detectors can be used simultaneously as complementary components in the same detection system.

The differential yields of these delayed signals have been utilized to discriminate nuclear from non-nuclear materials. Fission products produced via photofission reaction in nuclear materials are mostly unstable. Delayed neutrons and/or delayed gamma rays will be emitted during the de-excitation process. Delayed neutrons are traditionally represented by 6 groups with different mean half-lives [86]. The delayed neutron fractions for various nuclides are shown in Table 1.1. These delayed neutrons are unique signatures of nuclear materials. No delayed fission neutrons are produced when non-nuclear materials, such as lead, are irradiated by high-energy bremsstrahlung x-rays. However, photoneutrons can be produced via (γ, xn) reactions in both nuclear and non-nuclear materials when irradiated by high-energy photons (e.g. 22-MeV bremsstrahlung). One method to discriminate between photoneutrons and delayed fission

neutrons is to start the measurement only after the bremsstrahlung x-rays beam has been turned off for tens of milliseconds, due to the photoneutron population decreasing much faster than that of delayed fission neutrons. The detected neutron signals are almost entirely from delayed fission neutrons approximately several milliseconds after each linac pulse. Similar to photoneutrons, neutron-capture γ -rays are produced in both nuclear and non-nuclear materials. They can be differentiated from delayed fission γ -rays with the same method as described above. Shortly after each linac pulse, the measured counts from all samples are primary due to photoneutrons and neutron-capture γ -rays. Fission signatures are buried by these much stronger signals. Thus, similar die-away curves could be observed from nuclear and non-nuclear materials. Long after each linac pulse, delayed fission neutrons and γ -rays from fission products start to dominate over photoneutrons and neutron-capture γ -rays, respectively. For non-nuclear materials, such as lead, no delayed fission neutrons or delayed fission γ -rays are observed, the counts drop quickly to the background level. However, they maintain at a level well above background as to nuclear materials. High neutron and/or photon count rate long after irradiation (\sim several milliseconds) is a unique signature of nuclear materials [19].

Table 1.1 Delayed neutron fractions for various nuclides [20].

Group	Half-Life (sec)	Uranium-235	Uranium-238	Plutonium-239
1	55.6	0.00021	0.0002	0.00021
2	22.7	0.00141	0.0022	0.00182
3	6.22	0.00127	0.0025	0.00129
4	2.30	0.00255	0.0061	0.00199
5	0.61	0.00074	0.0035	0.00052
6	0.23	0.00027	0.0012	0.00027
TOTAL	-	0.00650	0.0157	0.00200

1.3 Photofission product yields

Design and development of active assay systems based on photofission technique largely rely on the availability of nuclear data, especially photofission product yields. While yields for neutron-induced fission of most nuclear materials (e.g. ^{232}Th , ^{235}U , ^{238}U , ^{239}Pu) have been well studied, verified, and made available in various nuclear databases, such as the Evaluated Nuclear Data File, results on photofission product yields are relatively scarce. Non-exhaustive examples of the photofission yields measurement are summarized here. Meason et al. reported photofission yields of ^{238}U back in 1965 [21]. In their study, monoenergetic γ -rays (17.5 MeV) were produced through the ^7Li (p, γ) $2\ ^4\text{He}$ reaction. Low-level β counting techniques were used to determine the yields. Photofission yields of ^{235}U and ^{238}U were measured by Jacobs et al. with 12-, 15-, 20-, 30-, and 70-MeV bremsstrahlung photon sources [22-23]. The fission product mass distribution

for ^{235}U at different bremsstrahlung beam energies was shown to have a doubly peaked shape without fine structure. The authors also observed a strong dependence of the symmetric mass yields and near independence of the asymmetric yields on the end-point energy of the bremsstrahlung source. Photofission yields of ^{238}U were also determined by Wehe et al. using a 9-MeV bremsstrahlung x-rays [16]. Delayed γ -rays were measured using HPGe and NaI (TI) detectors after photon irradiation of a ^{238}U sample. Cumulative yields of photofission products (e.g. ^{93}Sr , ^{132}Sb , $^{132\text{m}}\text{Sb}$, ^{89}Rb , ^{133}Sb) were reported. In the effort to characterize nuclear waste packages using photon activation analysis techniques, several measurement campaigns were performed by Carrel et al. to determine the photofission yields for optimizing the system design. Photofission yields of ^{235}U and ^{238}U induced by 16.3-MeV and 19.4-MeV bremsstrahlung x-rays were recently published by this group [24]. To the best of the authors' knowledge, no data concerning the photofission yields of ^{239}Pu is previously available. This poses a great challenge of application of photofission techniques in homeland security and nuclear safeguards applications.

1.4 Monte Carlo simulation of photofission process

Having the ability to accurately simulate delayed γ -rays and neutrons from fission reactions is also long-overdue and highly desired for homeland security and nuclear safeguards applications. In 2006, the US nuclear data program released a new photonuclear data library as part of the ENDF/B-VII. Although largely based on the earlier released IAEA photonuclear library, this new data library includes new or improved data for 24 isotopes. The improved actinide data now contains prompt and delayed-fission neutron spectra. Due to the lack of data and theoretical models for photofission, the photofission library used by MCNPX is primarily based on neutron-induced data [25]. The model used by MCNPX assumes that target nuclei will produce fission in the same way, regardless of the type of the incident particle (e.g., neutron or photon). Reedy et al. generated delayed γ -ray spectra using fission yield from ENDF/B-VII.0 and line emission data from ENSDF. Similar discrepancies between measured results and simulation data were reported. To enable the production of photons and neutrons from photofission reactions, the *ispn* entry of the *phys:p* card has to be changed from the default value (*ispn*=0) to enable photonuclear collision sampling [25]. Also, the *fism* entry of the *phys:p* card should be set to 1 to ensure that photofission secondaries are sampled only when a photofission event occurs if one prefers analog production of delayed neutrons and γ -rays. This is different from the default value (i.e. *fism*=0), where high-energy photons can produce secondary particles via a photonuclear interaction that is not necessarily from the same reaction. The energies and directions of the secondary particles are averaged over all possible photonuclear interactions including photofission. This default setting is only correct on average over a large number of interactions, thus its use is not suitable for applications where detail of secondary particles production is important, such as coincidence counting. In MCNPX, the physics module requires the ENDF/B-VII photonuclear data library *endf7u*. The *xsd* file for MCNPX installation has to be modified to include this library for MCNPX to access this photonuclear data library [25]. Both the *xsd*

file and the data library have to be present in the data file directory specified by the environmental variable DATAPATH. In addition to the settings discussed above, in order to enable photofission interactions and secondary emissions, the *DG* entry on the *ACT* card must be set to *LINES* if individual line-amplitude details are desired. This is important to the simulation of delayed γ -ray energy spectra. However, enabling this option makes the simulation significantly slower [25].

1.5 High-rate challenges in pulsed photofission environment

Gamma spectroscopy systems with high-rate capability are in great demand in the applications of active interrogation techniques in homeland security and nuclear safeguards. For example, during an assay of used nuclear fuel assemblies, the input γ -rays count rate can reach 10^6 counts per second (cps) or higher even after a few years of cooling. Many efforts were devoted to develop high-throughput high-resolution gamma spectroscopy systems for such measurements. The ADONIS system developed by CEA was designed to balance the trade-off between energy resolution and throughput rate using a bimodal Kalman smoother [26-28]. The highlight was the introduction of a hidden semi-Markov variable. A team from Pacific Northwest National Laboratory (PNNL) demonstrated that relatively good energy resolution (~ 8 keV at 662 keV) and high throughput (39%) could be achieved at an input count rate as high as 1.03×10^6 cps [29]. Figure 1.2 shows the comparison between energy spectra reconstructed using the traditional trapezoidal filtering method and time-variant trapezoidal filtering approach. To accomplish this, seven traditional time-invariant trapezoidal filters were implemented in parallel. For the best trade-off between energy resolution and throughput, the filters with the longest rise time without causing pile-up were used for energy measurement.

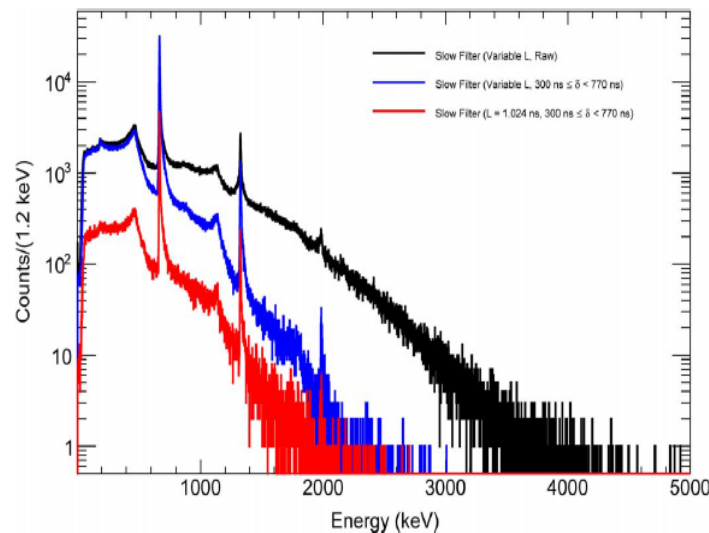


Figure 1.2 Energy spectra reconstructed using the traditional and time-variant trapezoidal filtering methods at input count rate of 1.03×10^6 cps [29].

On the other hand, to enhance sensitivity, pulsed photonuclear techniques are often utilized. For example, Idaho National Laboratory (INL) developed a nondestructive evaluation technique based on photoneutrons to detect nitrogen-rich explosives. Their system utilized a pulsed, high energy (2 to 12 MeV) linac and an HPGe-based gamma-ray spectroscopy system [30]. Highly penetrating bremsstrahlung x-rays were produced by the linac at a repetition rate of 47 Hz. Interrogating neutrons were generated in a photoneutron target (e.g. D₂O). Characteristic gamma rays were emitted upon absorption of interrogating neutrons by the object-of-interest. Gamma spectroscopy measurement was then performed in between linac pulses. To allow a fast recovery after each linac pulse, a transistor-reset preamplifier was modified in their detector system. Photonuclear techniques have also been studied for detection and quantification of special nuclear materials. The low intensities of spontaneous emission and the low energies of β -decay γ -rays make passive nondestructive assay difficult under many circumstances. Photonuclear techniques have been identified as an effective solution. Unique signatures following induced fission could be employed as the basis for detection, identification, and quantification of nuclear materials.

1.6 Real-time signal processing on FPGAs

Off-line processing is not practical when high sampling rate and long data acquisition time is necessary. Storing all raw data acquired with digitizers at high sampling rate (e.g. ~ 50 MSPS) will cause a storage overload problem in the case where the duration of an experiment lasts hours or even more. Real-time Digital Signal Processing (DSP) techniques are much more attractive since the amount of information needed to be stored could be greatly reduced. Modern FPGAs possess high computational power and large amount of hardware resource including dedicated DSP modules. They offer a wide variety of possibilities for real-time DSP.

2 Measurement of delayed γ -rays from photofission

An initial test was performed at Idaho National Laboratory (INL) in the week of June 4th, 2012. The purpose of this test was to establish a baseline of our current technical capabilities, which served as the basis for future improvement. The measurements of energy spectra and differential yields of delayed γ -rays from photofission of various nuclear materials were performed at Idaho Accelerator Center (IAC) from 11/5/2012 to 11/7/2012. Another photofission experiment campaign was also conducted at IAC from 7/21/2014 to 7/25/2014. Photofission product yields of ^{238}U and ^{239}Pu were determined based on the high-energy delayed γ -ray spectra measured in between linac pulses and the low-energy spectra acquired after irradiation.

2.1 Initial Test at Idaho National Laboratory

The test lasted five days, involving team members from the University of Utah and INL. Combinations of various electronics, detectors, and experimental setups were tested and evaluated. Overall, we achieved our goal and acquired valuable data for further analysis. Challenges have also been observed, which need to be addressed.

2.1.1 Equipment and experimental setup

In this test, the following equipment was available to the team.

Linac:

- INL's Varitron linear accelerator running at nominal 10 MeV.



Figure 2.1 Varitron linear accelerator used in the initial test.

HPGe detectors:

- Two Canberra GC2020 with RC pre-amplifier
- One ORTEC 24% detector with RC pre-amplifier
- One Princeton-Gamma-Tech 18% detector with modified TRP pre-amplifier
- One Princeton-Gamma-Tech 44% detector with TRP pre-amplifier



Figure 2.2 HPGe detectors used in the initial test

Data acquisition systems:

- NIM-based analog spectrometry system
- Canberra LYNX MCA
- Fast ComTec system
- High speed digitization system based National Instruments PXIe-5122



Figure 2.3 High speed digitization system based NI PXIe-5122.

The experimental setup is shown in Figure 2.4. The detector and front-end electronics were positioned in a shielding cavity built with lead and bismuth bricks. This detector and shielding assembly was located out of the linac beam in a backscattering angle. The detector was pointing at a sample placed in the beam. The distance between the Bremsstrahlung target and the sample was around 60". The distance between the sample and the front end of the detector was about 20".

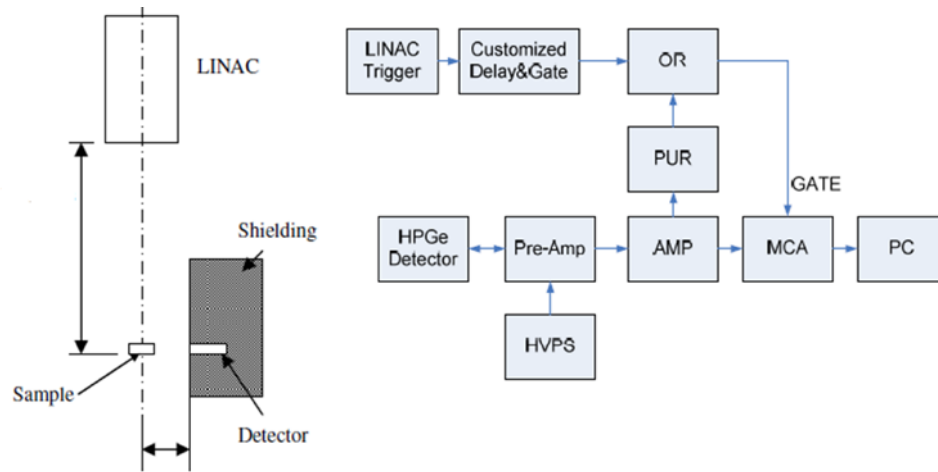


Figure 2.4 Experimental setup of the initial test.

2.1.2 Interlace mode measurement

The simplest and most straight-forward way to measure delayed gamma rays after photofission is to use interlace mode. In this mode, the sample is bombarded for a certain amount of time. Then the linac is turned off and the spectrometry measurement starts. This irradiation-counting sequence can be repeated indefinitely until satisfactory results are obtained.

Spectra shown in Figure 2.5 were measured using this method, with both DU and HEU samples. Full energy peaks from fission products have been observed and identified in these spectra. Although counting in interlace mode is easy to implement, short-lived fission products are hard to identify and quantify based on spectra measured this way. Shorter-lived isotopes die away faster after each linac pulse. Thus, after the irradiation period, the only short-lived isotopes measured were produced at the end of the irradiation. On the other hand, the measured activity of long-lived isotope is the integral activity over the whole irradiation period. As shown in Figure 2.5, the shorter-lived Sr-94 is less prominent than the longer-lived Cs-138, although Sr-94 has a larger fission yield.

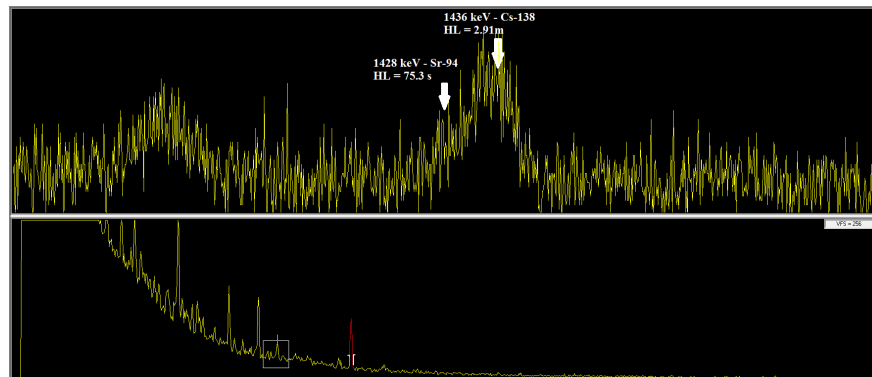


Figure 2.5 Spectra measured using the interlace mode.

2.1.3 Delayed gamma spectrum measured in between linac pulses

Interlace mode measurements described above are straight-forward and put less stress on the electronics and detectors. However, the majority of fission products have relatively short half-lives. After being produced during each linac pulse, these fission products quickly decay away. In interlace mode, for short-lived fission products, only the last few pulses would make contribution to the final spectrum. In order to capture short-lived isotopes and increase the sensitivity of the measurement, it is preferred that spectrometry measurements be performed in between LINAC pulses. As will be discussed later, we were able to observe the output signal from the HPGe detector preamplifier after each linac pulse. Because of the huge energy deposition during each pulse, the detector and front-end electronics are saturated for a relatively long time period (~tens of ms), as shown in Figure 2.6. After this, the baseline slowly returns to zero as shown below. Traditional shaping methods cannot handle this behavior very well, so the measurements have to be gated. In the following measurement, the linac was running at 20 Hz, i.e. the time interval between two adjacent pulses is 50 ms. After each pulse, the MCA waits for 20 ms before starting processing incoming signal. The counting continues for 20 ms before the MCA is disabled right before the next pulse hits.

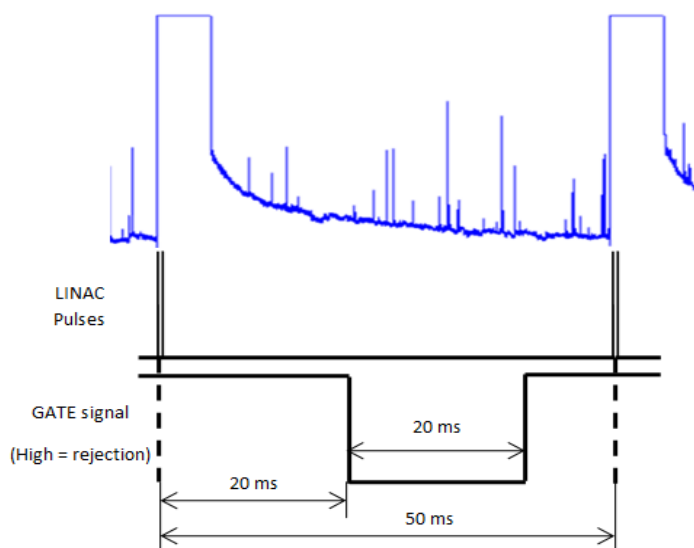


Figure 2.6 Measurement in between linac pulses.

Using this method, delayed gamma spectra were measured with both a DU sample and a HEU sample, as shown in Figure 2.7. Peaks from fission products (e.g. Sr-94 and Cs-138) are clearly observable, despite the fact that our counting time was quite limited (~ 500s with at least 50% dead time). Because of the poor counting statistics and the low detector efficiency at higher energies, we were not able to quantitatively study the difference between HEU and DU spectra. The degradation in energy resolution caused overlapping between gamma peaks from the check

source and fission products, which makes it even harder to analytically report the measurement results.

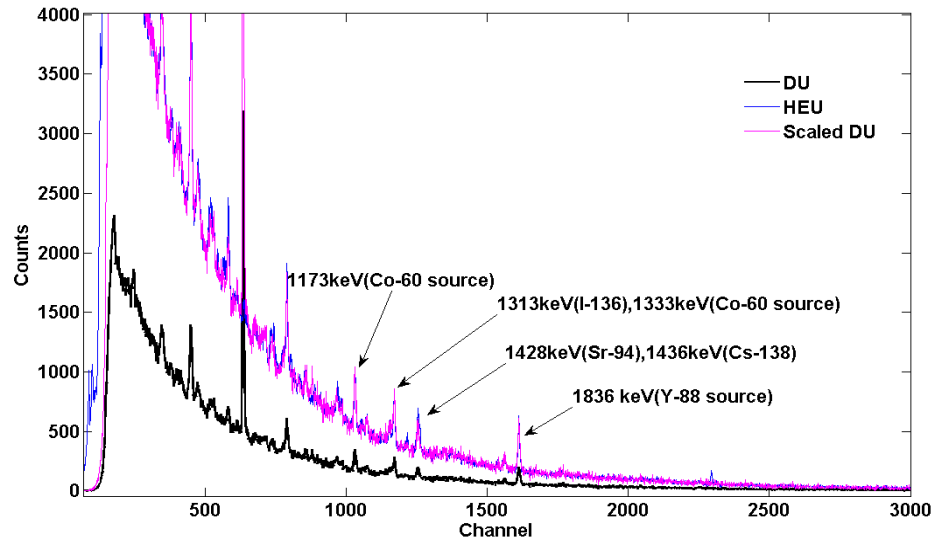


Figure 2.7 Spectra measured in between linac pulses.

2.1.4 High-speed digitization system

The ultimate goal of this task was to develop a real-time DSP algorithm suitable for high throughput applications and to implement it on a FPGA based system. For this purpose, we have purchased a standalone high-speed digitizer. The idea is to digitize and stream output signal from the detector to a PC, so that various algorithms can be developed and tested offline first. A FPGA module and a digitizer with compatible interface have also been ordered. Once optimal algorithms have been identified and developed, we plan to implement them on the FPGA module for real-time signal processing.

As a start, a LABVIEW interface shown in Figure 2.8 has been developed to enable streaming of digitized data to hard drive at full speed (100 MSPS, 14-bit) if one channel is utilized, or at half of the full speed (50 MSPS, 14-bit) if both channels on the digitizer are utilized. The speed of data streaming is mainly limited by the write speed of the hard drive. In our case, two Intel Solid State Disks are configured in RAID 0 array to maximize the transfer rate. The LABVIEW interface is shown below.

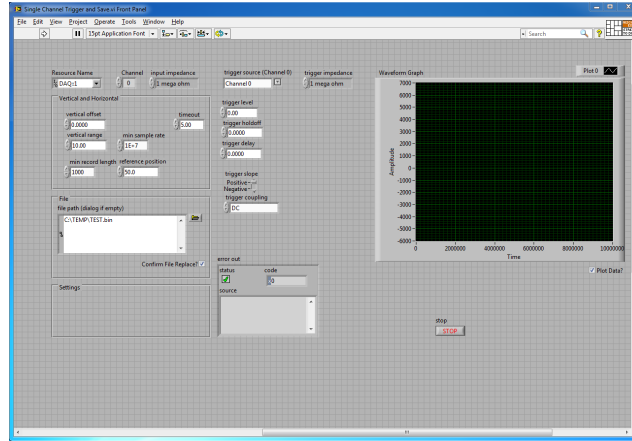


Figure 2.8 LABVIEW interface used to control the data acquisition process.

Using this interface, we were able to configure and control the digitizer. In the initial test, the digitizer was triggered by the linac pulses. During the measurements, the linac was running at 10 Hz, i.e. the time interval between two adjacent pulses is 100 ms. The digitizer was configured to record data for 120 ms each time it was triggered. Figure 2.9 shows the output signal from the preamplifier after a linac pulse.

As shown in Figure 2.9, the detector output is saturated for roughly 20 ms in this particular case. The recovery time is related to the energy deposition in the detector (i.e. beam current, beam energy, shielding around the detector, target in the beam, etc.). The baseline of the output signal slowly returns to normal after each linac pulse. The digitized data was recorded for further analysis that will be discussed below.

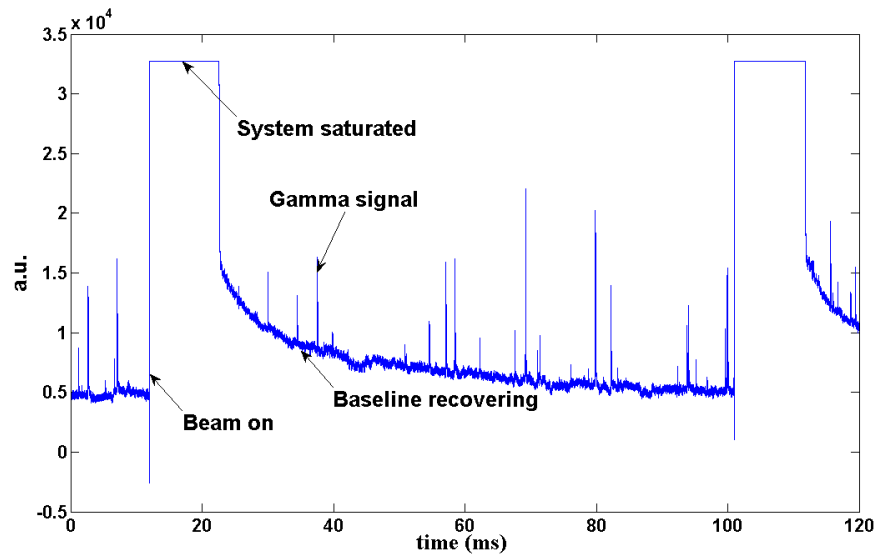


Figure 2.9 HPGc preamplifier output showing the saturation.

2.1.5 Conclusions

This initial test at INL was a big step forward for this project. The team has re-acquainted itself with the pulsed mode linac photonuclear counting scenario. Various data acquisition systems have been used to record data including a tradition analog setup, an off-the-shelf digital MCA and a high-speed digitization system. The challenges that we were facing here was the ultra-high count rate during each linac pulse, even with massive shielding around the detector. This high rate caused the detector to saturate for a long time period on the order of tens of ms in our case. Being able to observe and record the output signal using the digitization system allows us to develop electronics and algorithms that can optimize system performance in such a counting environment.

2.2 Energy spectra and differential yields of delayed γ -rays

The test was performed at IAC and lasted three days. The goal of this test was to obtain high-fidelity experimental data that could be used later on for various purposes, including benchmark of the Monte Carlo simulation results, testing of DSP algorithms being developed, etc. Various electronics systems were tested during this experiment, including commercially available Canberra LYNX system, NIM modules and our customized high-speed digitization system. Testing of these systems utilized the nuclear material inventory supplied by IAC including DU plates, ^{232}Th , and ^{239}Pu .

2.2.1 Equipment and experimental setup

The following equipment was available to the team during this experiment.

LINAC:

- IAC's 25-MeV linear electron accelerator



Figure 2.10 The 25-MeV linac at IAC.

HPGe detectors:

- Two Canberra GC2020 with RC pre-amplifier



Figure 2.11 The HPGe detectors used in the test at IAC.

Boron-loaded liquid scintillator:

- Eljen EJ-339A

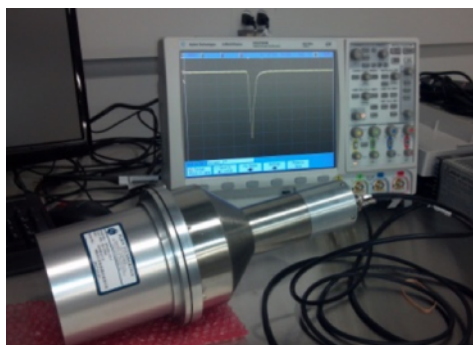


Figure 2.12 The boron-loaded liquid scintillator EJ-339A.

The accelerator was operated at 15Hz with 150nC charge per pulse. The linac was separated from the counting room by a 183 cm concrete wall. The photon beam was collimated to minimize interference with detectors and associated electronics. The scintillation and HPGe detectors were positioned at a 90 degree backscattering angle. In order to further reduce interference due to scattering from surrounding materials, the HPGe detector was shielded by lead bricks. For the scintillation detector, polyethylene bricks were used to absorb neutrons from background. In addition, lead bricks were included to shield the gamma rays and the neutrons slowed in polyethylene bricks. The experimental setup is shown in Figure 2.13. In the measurements, the scintillation detector used was a 5" by 5" boron loaded liquid scintillation detector, EJ-339. On the opposite side of the sample, one HPGe detector was used to measure the delayed gamma ray energy spectrum. The samples used in this experiment were depleted uranium (DU), Th-232, and lead. Each sample was placed on the centerline of the photon beam. The signals from the preamplifier were connected to a high-speed data acquisition system and the Genie 2000 gamma spectrum acquisition system. The high-speed data acquisition system was needed to handle the high count rate shortly after each linac pulse. Figure 2.14 shows the system used during the experiments performed at IAC, including a National Instruments high-speed digitizer PXIe-5122 and the host PC.

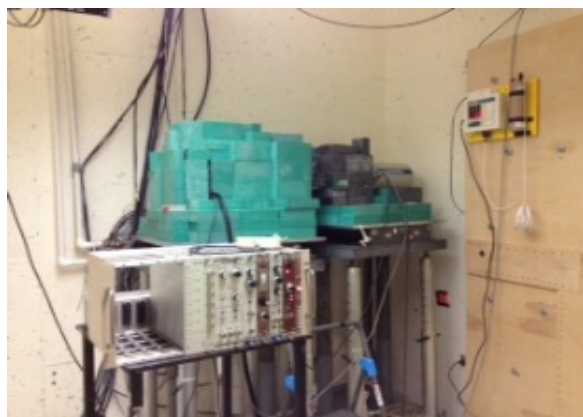


Figure 2.13 A picture of the experimental setup.



Figure 2.14 The high-speed data acquisition system.

2.2.2 Delayed fission gamma energy spectra measured with a Canberra LYNX

The commercial gamma spectroscopy system was a multi-channel analyzer from Canberra industry. The multi-channel analyzer was controlled by the Genie 2000 software. The coincidence mode was used to control the data acquisition in between the shutting off of linac 20 ms later till the next pulse. Approximately 46 ms between two successive pulses was used to measure the delayed gamma rays. The 20 ms gate time was set up by a Function Generator Agilent AFG3021C. As shown in our previous study, there are amount of interferences from neutron capture gamma rays which are produced by the neutron absorption of shielding materials, air, and surrounding concrete materials. However, these gamma rays decay much faster than delayed fission gamma rays. So it is beneficial to perform the measurements after the turning off of the linac pulse. The gate signal was also used in the measurement with the Fast ComTec list-mode system. The measurement time for DU was 2 hours, 100 minutes for Pu-239. Figures 2.15 and 2.16 show the delayed gamma rays energy spectra from DU and Pu-239 induced by high-energy photons. The active interrogation photon source from linac was produced by the de-accelerating of electrons with energy of 22 MeV when bombarding a 4.2

g/cm² thick tungsten. The accelerator was operated at 15 Hz with 150 nC charge per pulse. Every pulse had a width of 4 μ s. The measurement was performed after the shutting off of former pulse for 20 ms till the beginning of the next pulse in order to reduce the interference of non-fission gamma rays. As shown in Figures 2.15 and 2.16, there were delayed gamma rays with energy above 3 MeV from DU measurement, but this didn't happen in the Pu-239 measurement. One of the reasons was that it took two hours to measure the energy spectrum for DU target, while only about 100 minutes was used in the measurement for Pu-239 sample.

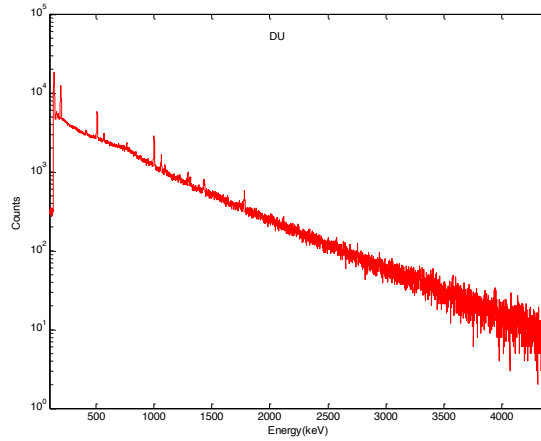


Figure 2.15 Delayed γ -ray spectra measured from photofission of DU.

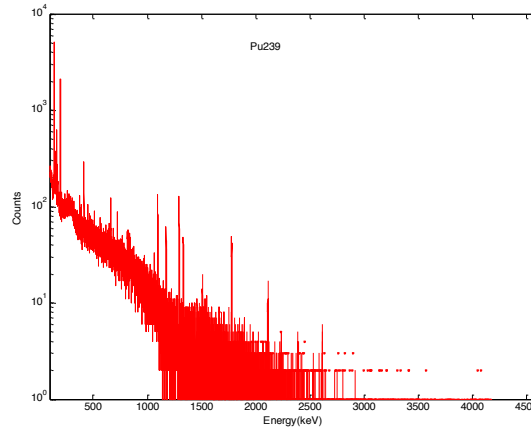


Figure 2.16 Delayed γ -ray spectra measured from photofission of ²³⁹Pu.

2.2.3 Delayed fission gamma spectra measured with a Fast ComTec list-mode system

The Fast ComTec list mode system was provided by Idaho Accelerator Center. It is an analog data acquisition system. One of the advantages of this system is that it can simultaneously record both energy and time information of every event, which can be used to obtain delayed gamma rays spectrum acquired during different time periods in between two successive pulses and the

energy spectrum with different gate time not less than the one already set before performing experiment. Therefore, it is possible to see the change of delayed gamma rays spectra with increasing time if the gate time is set to several ms and the detector should not be saturated after the gate time. This means that the prompt gamma rays energy spectrum can be measured if the gate time can be set to be about 1ms and the detector has such short response time that it will not be saturated. In this experiment, this cannot be done as the gate time was set to be 10ms. There are not obvious changes about delayed gamma rays spectra acquired after 10ms, 20ms, and 30ms for DU and Pu-239, as shown in Figures 2.17 and 2.18. Also, there are no obvious changes of delayed gamma rays spectra recorded during different time period in between pulses for DU. The above results show that the time width between two adjacent pulses can also be changed without affecting the measurement of delayed gamma rays energy spectrum, such as 30 ms.

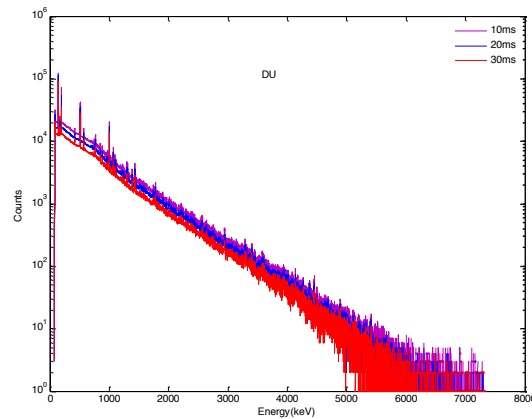


Figure 2.17 Delayed γ -ray spectra acquired using gate time of 10 ms, 20 ms, and 30 ms (DU).

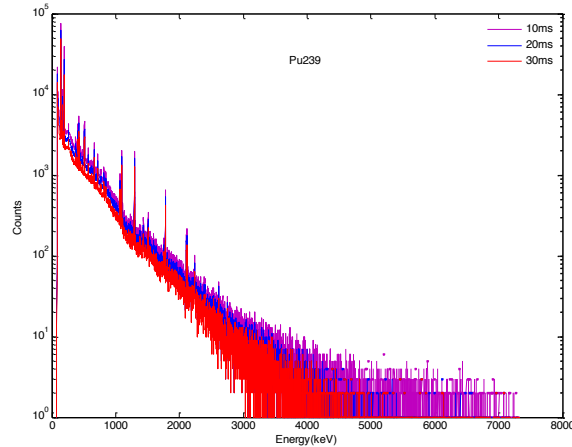


Figure 2.18 Delayed γ -ray spectra acquired using gate time of 10 ms, 20 ms, and 30 ms (^{239}Pu).

In our experiments, we also measured the gamma rays spectra immediately after the turning off the linac. As shown in Figures 2.19 and 2.20, the energy spectra acquired after the turning off of linac included much less high-energy gamma rays (above 3 MeV). This is because of the short half-lives of most fission fragments from photon induced fission.

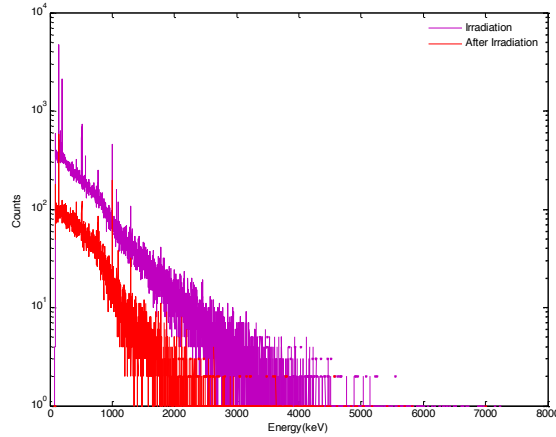


Figure 2.19 Delayed γ -ray spectra acquired during irradiation and after irradiation (DU).

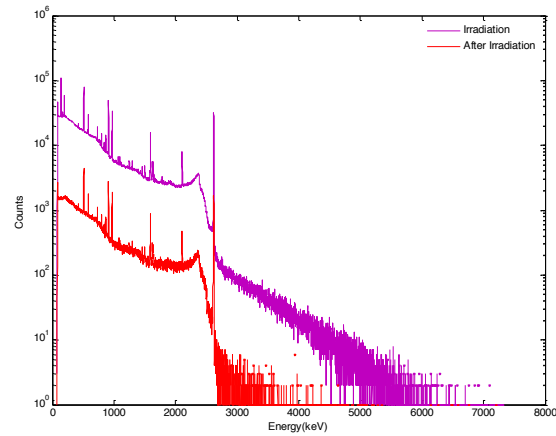


Figure 2.20 Delayed γ -ray spectra acquired during irradiation and after irradiation (^{232}Th).

2.2.4 Delayed fission gamma spectra measured with a customized high-speed digitizer

Figures 2.21 and 2.22 show the energy spectra measured using the high-speed digitizer system. All digitized data was processed off-line using customized digital signal processing techniques implemented in Matlab. One pile-up rejection algorithm was included to deal with the double pulses. If two pulses were added together, both of them were rejected. In our experiments, a mixed calibration source containing Co-60, Cs-137, and Eu-152 was first used to take the calibration measurement. As shown in the energy spectra of the calibration source, all of the energy peaks from Co-60 and Cs-137 source can be found. Some energy peaks from Eu-152 are not identified due to the less measurement time. The calibration energy spectra show that the energy resolution from the DAQ system is comparable to the commercial gamma spectroscopy system. The delayed gamma rays energy spectrum for Th-232 induced by high-energy photons was reconstructed from the digitized data and compared with the energy spectrum from the Fast ComTec list-mode system.

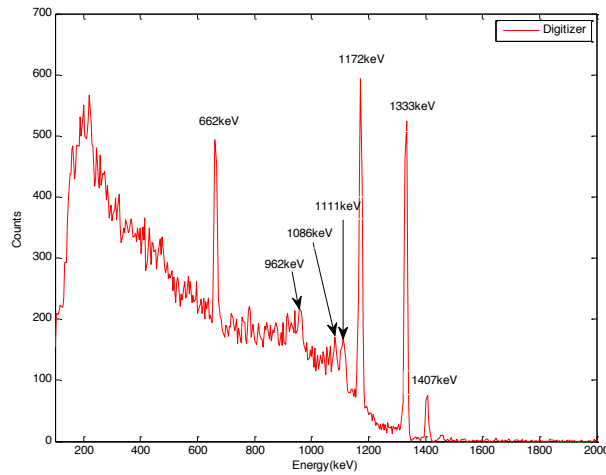


Figure 2.21 Energy spectrum measured with the high-speed digitizer (calibration source).

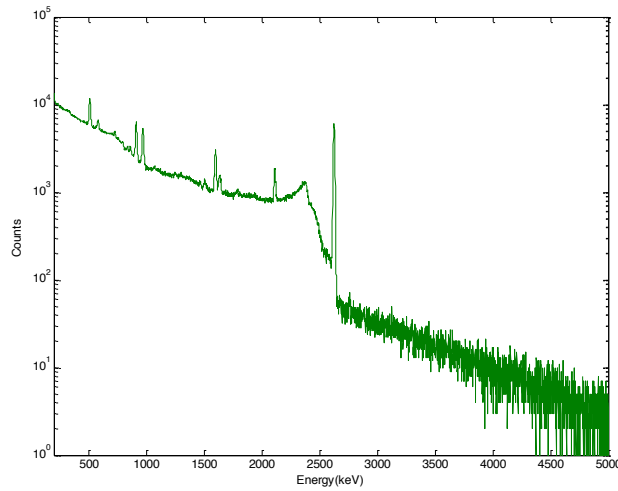


Figure 2.22 Energy spectrum measured with the high-speed digitizer (^{232}Th).

2.2.5 Spectra comparison

Figures 2.23-2.25 show the comparison of energy spectra measured with the commercial LYNX system and the Fast ComTec list-mode system. In our experiments, the output from one HPGe detector was sent to the LYNX system, the output from another HPGe detector was connected with the Fast ComTec list-mode system. The two detectors were the same with 20% efficiency. The other experimental setup, such as linac and geometry, were also the same. These two spectra are comparable with each other, which means the Fast ComTec list-mode system is also a good candidate for energy spectrum measurement.

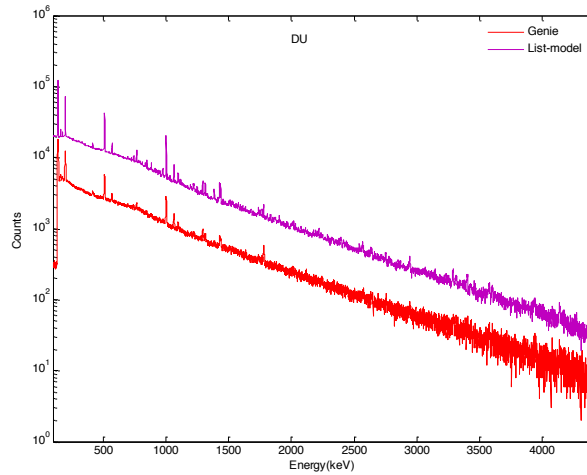


Figure 2.23 Delayed γ -ray spectra measured with the Canberra LYNX and the Fast ComTec list-mode system (DU, 0.2 MeV-4.0 MeV).

As the statistical error in high-energy region is higher than that in low-energy region, the comparison is highlighted in the energy range from 100 keV to 2000 keV. As can be seen from Figure 2.24, the energy peaks in the energy spectra from the commercial gamma spectroscopy system can also be found in the energy spectra from the Fast ComTec list-mode system.

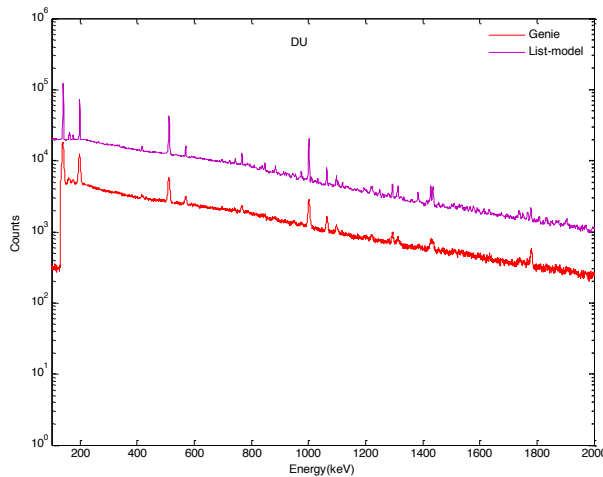


Figure 2.24 Delayed γ -ray spectra measured with the Canberra LYNX and the Fast ComTec list-mode system (DU, 0.2 MeV-2.0 MeV).

Figure 2.25 shows the comparison of energy spectra measured with the high-speed digitizer system and the Fast ComTec list-mode system. The results say that the DAQ system has a capability to measure the delayed gamma rays energy spectrum which is comparable to the Fast ComTec list-mode system and the LYNX system regarding the energy resolution. The one disadvantage of the customized system is that it needs large space to store the digitized data. Therefore, the next step is to implement the digitized data processing on FPGA in real-time.

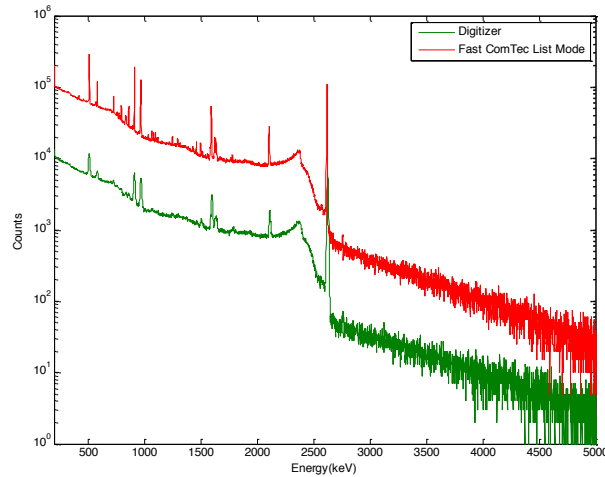
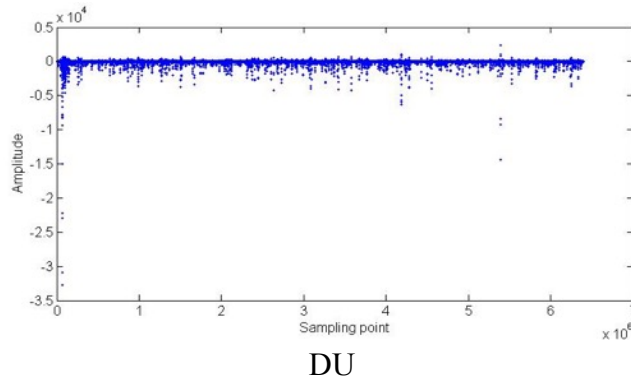


Figure 2.25 Delayed γ -ray spectra measured with the Canberra LYNX and the Fast ComTec list-mode system (^{232}Th).

2.2.6 Differential yields measurements with the liquid scintillator

A depleted uranium sample, a Th-232 sample and a lead sample were irradiated with a pulsed bremsstrahlung X-ray beam with endpoint energy of 22 MeV respectively. During the interrogation, neutrons can be produced in all samples through photonuclear reactions. Some of these neutrons are moderated and eventually absorbed by samples and surrounding materials. Neutron capture gamma rays can be emitted during this absorption process. On the other hand, photofission reactions are induced uniquely in nuclear materials. Fission fragments are normally produced in their excited energy states, and de-excite to lower energy states later on by emitting delayed neutrons and / or gamma rays. These delayed neutrons and gamma rays are signatures of nuclear materials. In this work, delayed neutrons and gamma rays emitted between linac pulses were measured with a boron-loaded liquid scintillation detector shown below. The signals from the anode of the PMT were digitized for post-processing using digital signal processing techniques. The digitized output signals from the anode of the PMT after a linac pulse from the DU sample, the Th-232 sample and the lead sample are shown in Figure 2.26.



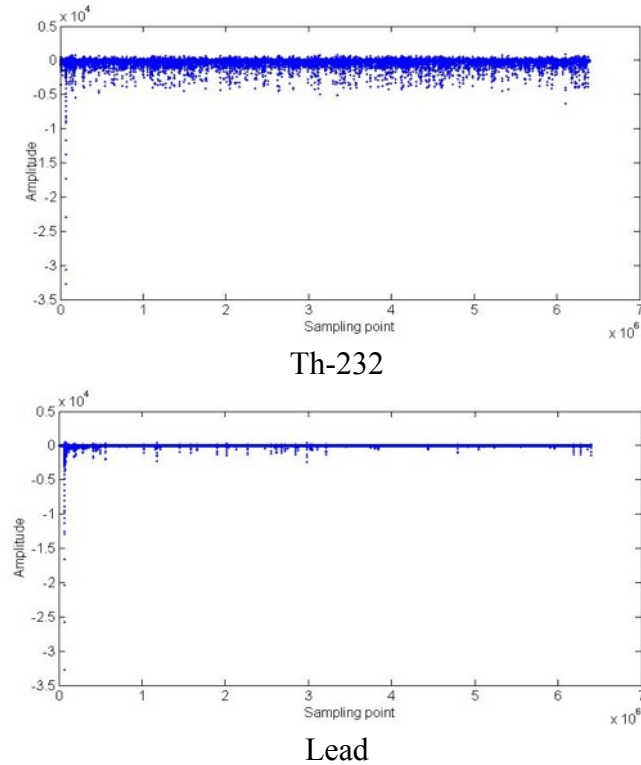


Figure 2.26 Signals acquired in between linac pulses (DU, 232Th, lead).

Due to mis-coupling and cable reflection, there is a small overshoot following every pulse recorded, as shown in Figure 2.27. All the data was processed offline using customized digital signal processing techniques implemented in Matlab. One important step is to appropriately choose a threshold. The amplitude of the threshold should be high enough to avoid double triggering by the small overshoot following the major pulse. For example threshold 2 is preferable to 1 because of the possibility of false triggering by the small overshoot.

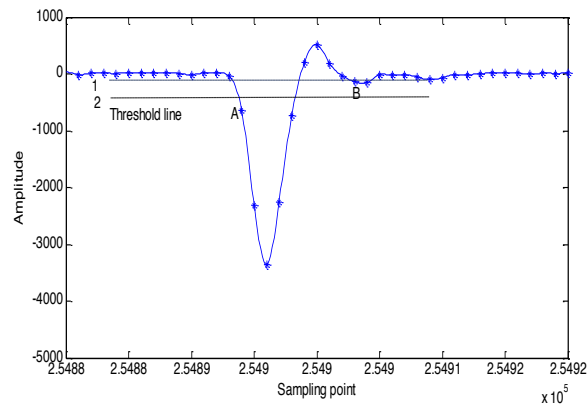


Figure 2.27 Illustration of threshold value choice.

Data from the digitizer was processed with a customized MATLAB script. Figure 2.28 shows the die-away of the relative count rate of neutrons and gamma rays as a function of time. For nuclear materials such as DU and Th-232, photoneutrons, delayed fission neutrons, neutron

capture gamma rays and delayed fission gamma rays contribute to the measured signal. On the other hand, there is only contribution from photoneutrons and neutron capture gamma rays for non-nuclear materials, such as Pb.

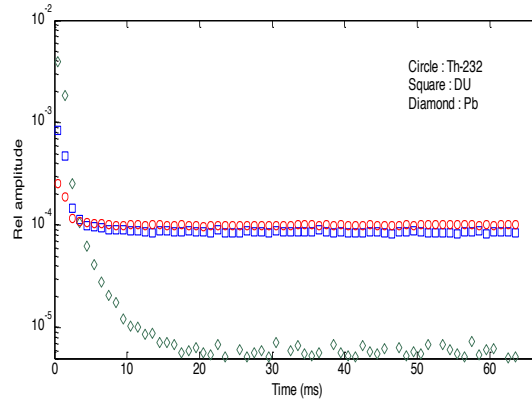


Figure 2.28 Differential yields of delayed γ -rays from nuclear and non-nuclear materials.

The counts for the Pb sample drop much faster than the DU and Th-232 samples and reach the background level around 20 ms after each linac pulse. However, the counts from the DU or Th-232 sample are much higher long after each linac pulse. The difference in these die-away curves can be explained by the difference in interactions between the interrogation photons and the sample materials. Shortly after each linac pulse, the measured counts for all samples come mainly from photoneutrons and neutron capture gamma rays. Fission signatures are buried by these much stronger signals. Thus, similar die-away curves have been observed from all three samples. Long after each linac pulse, delayed neutrons and gamma rays from photofission fragments start to dominate. For non-nuclear materials such as Pb, no delayed fission neutrons or delayed fission gamma rays are observed, the counts drop quickly to the background level. The temporal behavior of count rate of neutrons and photons is one effective way to discriminate nuclear materials from non-nuclear materials in order to interdict concealed nuclear materials for homeland security and nuclear nonproliferation.

2.3 Photofission product yields of ^{238}U and ^{239}Pu

The measurements were performed at IAC from 7/21/2014 to 7/25/2014. The objectives of the experimental campaign were to determine photofission product yields of ^{238}U and ^{239}Pu and verify the effect of the modification to feedback resistor of the preamplifier on the saturation time following each linac pulse in a photofission environment.

2.3.1 Experimental setup

The experimental setup is shown in Figure 2.29. The pulsed interrogation photon source used in these experiments was produced when electrons with energy of 22 MeV from the electron linac bombarded a tungsten radiator. The repetition frequency of the linac was set at 10 Hz. The

width of each linac pulse was 4 μ s. The time available for data acquisition between two adjacent pulses was approximately 100 ms. However, measurements were disabled till about 10 ms after the shut-off of a linac pulse to get rid of the interference from neutron-capture gamma rays. A signal generated from the arbitrary-function generator Agilent AFG3021C was used as the trigger signal. The amount of total charge contained in each linac pulse was 86 nC. The bremsstrahlung x-rays coming from the beam port had a maximum energy of 22 MeV. The bremsstrahlung beam had a diameter of approximately 7.5 cm at the target location. The targets included an 18.9 g/cm² DU plate, a 28.8 g/cm² lead brick, 3 g Plutonium (95% Pu-239, 5% Pu-240) and 3 g HEU with enrichment of around 20%. These targets were placed in the centerline of the x-rays beam with a distance of 47 cm from the beam port to the target. Two Canberra n-type coaxial high-purity germanium detectors (Model number GC4020, the size was 2.4" by 2.3") detectors with relative efficiency of 40% were used in the measurements. The HPGe detector on the right side was the detector with a modified preamplifier. The standard detector was placed on the left side. The entrance windows of the HPGe detectors which were positioned perpendicularly to the beam were kept at 8 cm away from the front surface of shielding and 21 cm from the target. The geometry setup was symmetrical about the centerline of the x-ray beam such that the two detectors received almost equal irradiation. The signals from the preamplifiers of the detectors were split after transferring to the data acquisition room so that the four DAQ systems could be simultaneously used to measure delayed γ -rays between adjacent linac pulses.

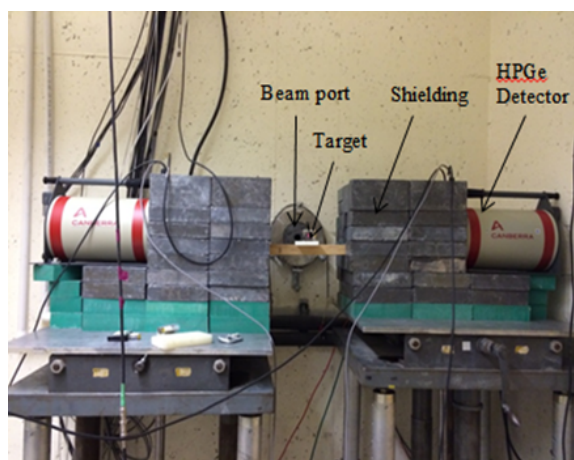


Figure 2.29 Experimental setup for the testing campaign at IAC.

Several DAQ systems including the Canberra Lynx system, the IAC FAST ComTec list-mode system, the customized system based on a National Instruments high-speed digitizer PXIe-5122, the CEA ADONIS system were utilized to measure delayed γ -rays between adjacent linac pulses. A list-mode system based on the ProSpect spectrum software from Canberra was also used to perform measurement after cooling down for about 15 minutes of the samples which were irradiated by the pulsed x-ray beams for about two hours. High-energy delayed gamma rays were measured between adjacent linac pulses using the four data-acquisition systems in parallel. A block diagram of the DAQ systems is shown in Figure 2.30. The DAQ systems were IAC FAST

ComTec list mode system, CEA ADONIS system, Canberra Lynx MCA system and customized system based on the National Instruments high-speed digitizer PXIe-5122. The IAC FAST ComTec list-mode system is an analog data acquisition system which includes a traditional shaping amplifier following a preamplifier. The shaping time for the Gaussian filtering of the shaping amplifier was 6 μ s. The shaped Gaussian signal was then sent to a digitizer from Ortec to extract the energy information. The data acquisition controlled by the software MPA-3 was set as a list mode such that both energy and time information for each individual γ -ray event were recorded. A script written in C++ by the Dr. Hunt's group from Idaho Accelerator Center was used to extract the energy and time information from the list-mode data. In the CEA ADONIS system, the signal from the preamplifier was conditioned and digitized by a modified Canberra Lynx without passing through its trapezoidal filtering part. The Canberra Lynx MCA system was controlled by the Canberra Genie2K software. The "coincidence mode" in the Genie2K was chosen to disable the acquisition process till the gate signal generated from the arbitrary-function generator was received by the Lynx system. The digitizer in the customized system was the PXIe-5122 from National Instruments. The signal from the preamplifier was connected to the analog channel A0 of the digitizer. The sampling rate used in the following experiments was 30 MSPS. A LabVIEW program was developed to stream digitized data onto a hard drive array for off-line processing in Matlab.

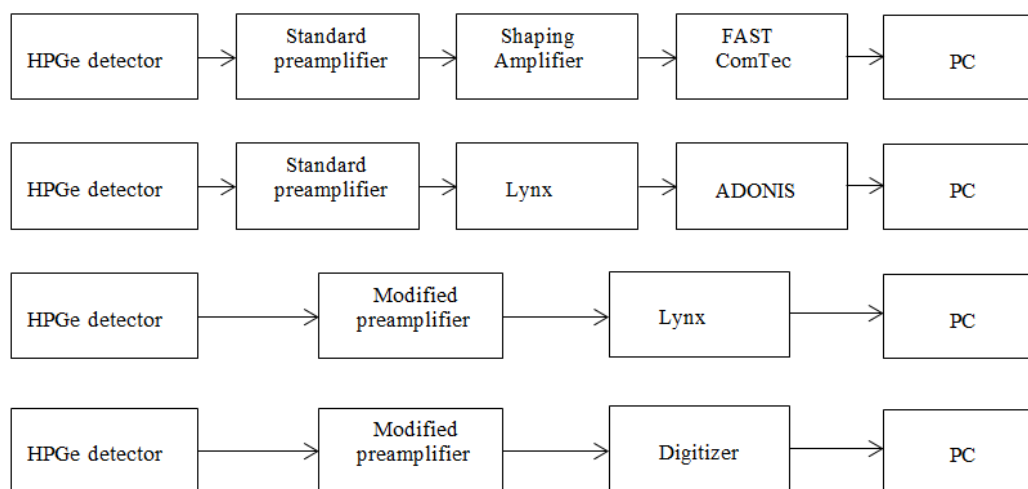


Figure 2.30 A block diagram of the data-acquisition systems.

2.3.2 Photofission product yields measured based on the high-energy delayed γ -rays spectra

The delayed gamma spectra from the DU and Plutonium and HEU samples shown in Figure 2.31 were measured with the Canberra Lynx system and the HPGe detector with a standard preamplifier. The rise time and flat top time for the trapezoidal filtering in the Lynx system were 11 μ s and 0.8 μ s, respectively. The measurement time of about 45 minutes for DU sample was long enough to have an acceptable statistics because of large mass of the DU plates being

irradiated. However, the Plutonium and HEU measurements last respectively 160 minutes and 130 minutes which were much longer compared to that of the DU measurement. The linac was operated at 10 Hz and the energy of electron was 22 MeV. The width of each linac pulse was about 4 μ s. The time available for data acquisition between two adjacent pulses was approximately 100 ms. A signal with gate time of 10 ms was used to disable the measurement during the saturation time. To better observe the difference among the delayed gamma spectra for DU, HEU and Pu the spectra shown in Figure 2.31 were divided into three regions. The photofission products related to the high-energy peaks presented in the measured delayed gamma spectra was identified using the database from URL <http://ie.lbl.gov/toi/index.htm>. These photofission products are also shown in the Figures 2.33-2.35.

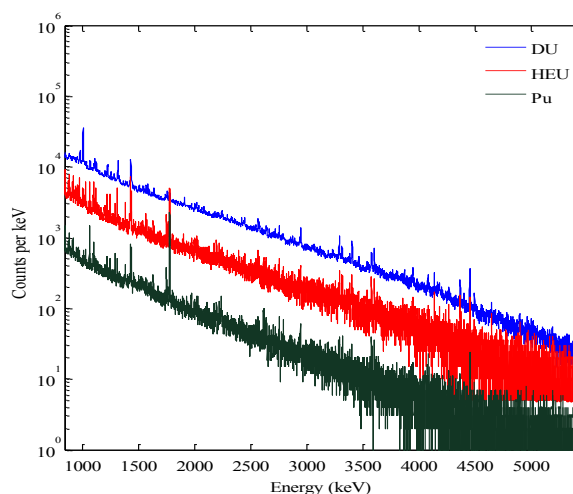


Figure 2.31 Delayed γ -ray spectra measured with the Canberra Lynx system (DU, HEU and Pu).

As shown in Figure 2.32, the peak pairs with energy of 2632.4 keV and 2639.6 keV have different ratios for DU, Pu and HEU. Figure 2.33 shows another peak pairs (i.e. 3576 keV and 3599.7 keV) which are sensitive to nuclear materials. The peak areas under the peaks were calculated using the add-on interactive peak fitting package of the Genie-2K spectrum analysis software. The VMS Standard Peak Search Fit with 4 background channels was chosen to locate the peaks. The calculated peak ratios for these two peak pairs are shown in the Table 2.1 below. The peak ratio between the peaks with energy of 2632.4 keV and 2639.6 keV for DU is 1.15 which is much larger compared with that for Pu. The peak ratios shown in Table 4 could be used to determine isotope compositions of a mixture in our future experimental study.

Table 2.1 Measured peak ratios for the DU, HEU and Pu samples.

Measured Peak ratio	DU	HEU	Pu
2632.4/2639.6	1.15	0.85	0.54
3576/3599.7	0.79	0.93	1.27

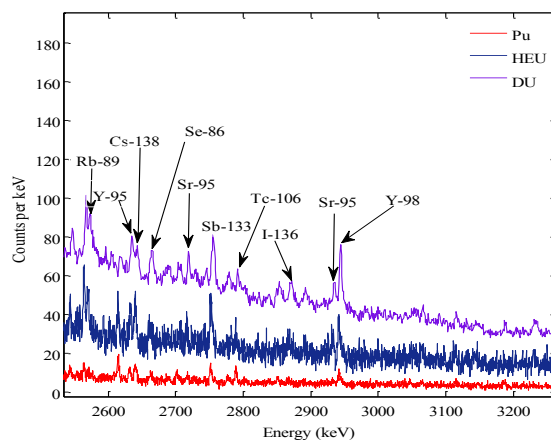


Figure 2.32 Delayed γ -ray spectra measured with the Canberra Lynx system (2.6 MeV-3.2 MeV).

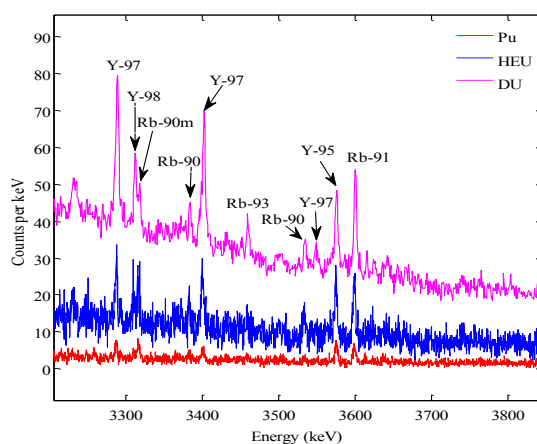


Figure 2.33 Delayed γ -ray spectra measured with the Canberra Lynx system (2.6 MeV-3.2 MeV).

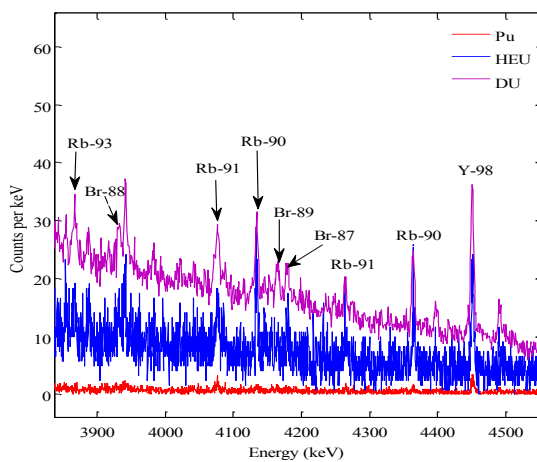


Figure 2.34 Delayed γ -ray spectra measured with the Canberra Lynx system (3.9 MeV-4.5 MeV).

Because of the small amount of Pu and HEU samples there were not enough counts to calculate the peak areas of the identified high-energy peaks. The photofission product yields were only calculated from the delayed gamma spectrum from the DU sample. The photofission products were assigned using the database from URL <http://ie.lbl.gov/toi/index.htm>. As shown in Table 2.2, the half-lives of these products were in the range from 0.548 s to 258 s which were much shorter compared with the measurement time of 45 minutes. Most of the photofission products decay away by the end of irradiation time.

Table 2.2 Measured photofission product yields of ^{238}U based on high-energy delayed γ -rays.

Nuclide	Half-life (seconds)	Energy (keV)	Relative yield	Uncertainty (%)
^{95}Sr	23.9	2717.3	0.102	12
		2933.1	0.116	7
^{106}Tc	35.6	2789.3	0.094	16
^{136}I	83.4	2868.9	0.160	7
^{98}Y	0.5	2941.3	0.076	4
		3310.0	0.076	7
		4450.2	0.079	4
^{97}Y	3.8	3287.6	0.070	3
		3401.3	0.078	4
		3549.5	0.072	16
$^{90\text{m}}\text{Rb}$	258	3317.0	0.019	10
^{90}Rb	158	3534.2	0.043	13
		4135.5	0.041	13
		4365.9	0.043	7
^{93}Rb	5.8	3458.2	0.050	14
		3867.6	0.059	26
^{91}Rb	58.4	3599.7	0.072	4
		4078.3	0.073	8
^{88}Br	16.3	3932.4	0.055	11
^{89}Br	4.3	4166.3	0.027	20
^{87}Br	55.6	4180.5	0.029	18

2.3.3 Development of the list-mode system

A list-mode system was built using the Canberra Lynx, ProSpect software and a data analysis script. The ProSpect software is an application that can be used to control, collect and analyze gamma spectroscopy data. Both Lynx and Osprey Multi-Channel Analyzers (MCA) are

supported by this application. The parameters in the detector, MCA and acquisition settings are accessible in an easily used graphical user interface. Gamma spectroscopy data can be exported to Text, Excel, PDF and Canberra CAM files. CAM files from the Genie 2K are also able to be imported to the ProSpect for spectrum post-analysis. Acquisition modes include digital oscilloscope used to view the raw and shaped signals, Single Channel Analyzers, PHA, LIST, etc. The LIST mode was chosen in our recent experiments at Idaho Accelerator Center. It allowed the time and energy information about each gamma event to be recorded simultaneously. The spectroscopy data was transferred to host PC through an Ethernet cable and stored in a hard drive in the format of text files for offline processing. A script provided by Canberra was used to extract the time and energy information from these text files. The delayed gamma spectra measured within different time windows were able to be obtained using this script in order to view the time-dependent spectra and make an estimation about the half-lives of the delayed gamma peaks, which was helpful to identify the photopeaks associated with photofission fragments. The delayed gamma ray spectra and yields from photofission of DU and Pu measured with the list-mode system are shown in Section 2.3.4.

2.3.4 Photofission product yields measured using the list-mode system

The delayed gamma spectra from photofission of Pu measured with the list-mode system in different time windows are shown in Figures 2.35-2.38. The photopeaks from the decay of photofission fragments are identified in these Figures. As shown in Figure 2.39, due to the small quantity of the Plutonium sample, there were not enough counts to quantify the photofission fragments associated with the gamma photopeaks with energy above 1500 keV. The photopeaks with energy ranging from 641.3 keV to 1435.8 keV were used to calculate the relative photofission yields. Table 2.3 shows the identified photofission fragments, their half-lives and relative yields. For the DU sample, Figures 2.39-2.42 present the measured delayed gamma spectra, the relative photofission yields are shown in Table 2.4. As shown in Figure 2.42, most of the high energy delayed gamma peaks ($E > 3$ MeV) were not observed in the measurement with the list-mode system because of the very short half-lives of photofission fragments emitting high energy gammas.

The relative photofission yields were derived from the formula below. An assumption made in the derivation was that photofission events occurred only at the beginning of each pulse. It could be a reasonable assumption since the pulse width was pretty small compared to the repetition period of the linac (i.e. 4 μ s vs 0.1 s). The number of net counts under a photopeak from the decay of photofission fragments formed due to the n th pulse can be calculated as follows:

$$N_n = FY\epsilon\eta e^{-\lambda(T_i - (n-1)\tau)} e^{-\lambda T_c} (1 - e^{-\lambda T_m})$$

The total net counts were obtained by taking the sum of N_n over all of the pulses.

$$N = \sum_{n=1}^{n=T/\tau} N_n = FY\epsilon\eta \frac{(e^{-\lambda T_i} - 1)e^{-\lambda T_c}(1 - e^{-\lambda T_m})}{1 - e^{-\lambda \tau}}$$

Where F is the number of photofission events in a single pulse. Y is defined as the photofission yield. ϵ is the absolute photopeak efficiency of the HPGGe detectors, η is the branching ratio of the photopeak, λ is the decay constant, T_i is the time difference between the beginning of the first pulse and the ending of the last pulse, T_c is the length of cooling time, T_m is the total measurement time.

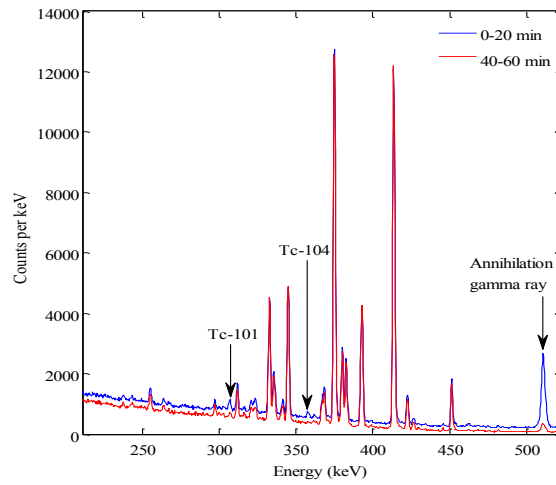


Figure 2.35 Measured delayed gamma spectra with the list-mode system (0.2 MeV-0.5 MeV, Pu).

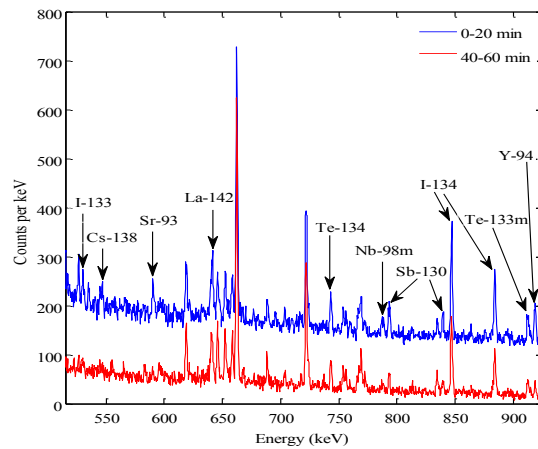


Figure 2.36 Measured delayed gamma spectra with the list-mode system (0.5 MeV-0.9 MeV, Pu).

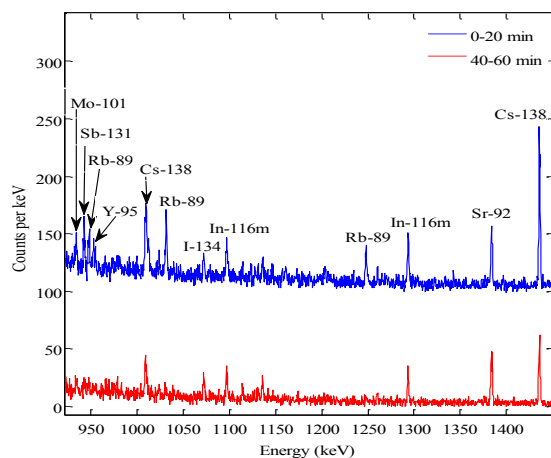


Figure 2.37 Measured delayed gamma spectra with the list-mode system (0.9 MeV-1.5 MeV, Pu).

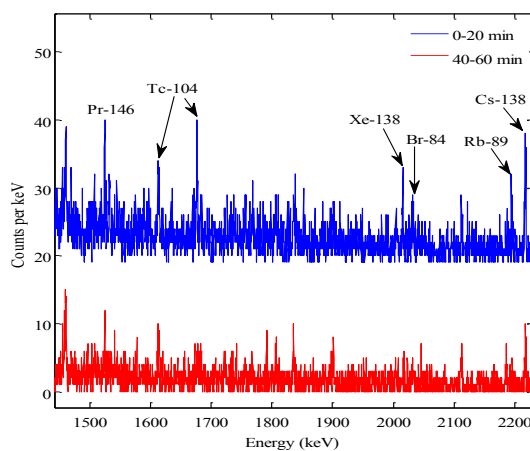


Figure 2.38 Measured delayed gamma spectra with the list-mode system (1.5 MeV-2.2 MeV, Pu).

Table 2.3 Measured photofission product yields of ^{239}Pu using the list-mode system.

Nuclide	Half-life	Energy (keV)	Relative yield	Uncertainty (%)
^{142}La	91.1 m	641.3	0.049	6
^{134}Te	41.8 m	742.6	0.116	7
$^{98\text{m}}\text{Nb}$	51.3 m	787.4	0.009	18
^{130}Sb	39.5 m	793.5	0.014	9
		839.5	0.011	10
^{134}I	52.5 m	847.0	0.060	2
		884.1	0.058	3
$^{133\text{m}}\text{Te}$	55.4 m	912.7	0.028	8
^{94}Y	18.7 m	918.7	0.046	7

^{131}Sb	23.0 m	943.4	0.021	16
^{95}Y	10.3 m	954.0	0.172	22
^{138}Cs	33.4 m	1009.8	0.050	8
		1435.8	0.060	3
^{89}Rb	15.2 m	1031.9	0.033	12
		1248.2	0.036	13
$^{116\text{m}}\text{In}$	54.3 m	1097.3	0.019	10
		1293.6	0.016	6
^{92}Sr	2.7 h	1383.9	0.040	5

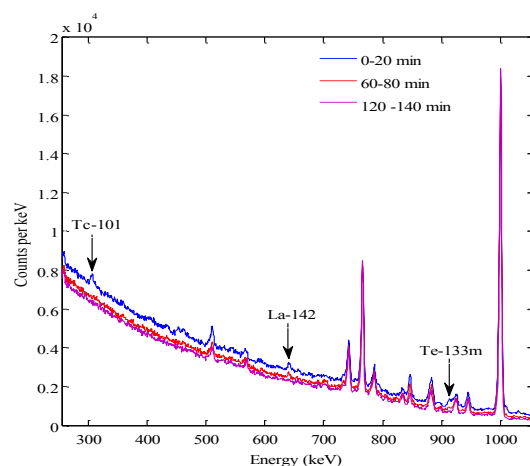


Figure 2.39 Measured delayed gamma spectra with the list-mode system (0.3 MeV-1.0 MeV, DU).

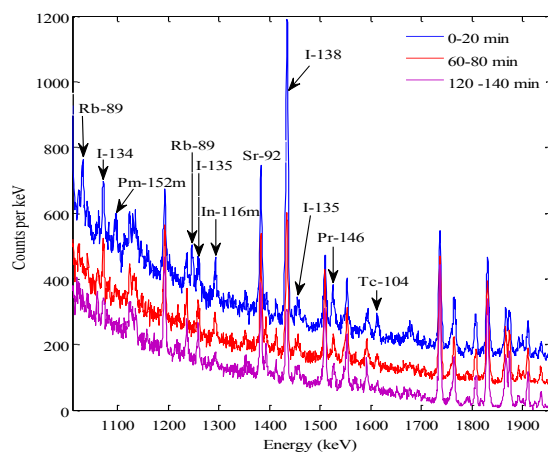


Figure 2.40 Measured delayed gamma spectra with the list-mode system (1.0 MeV-1.9 MeV, DU).

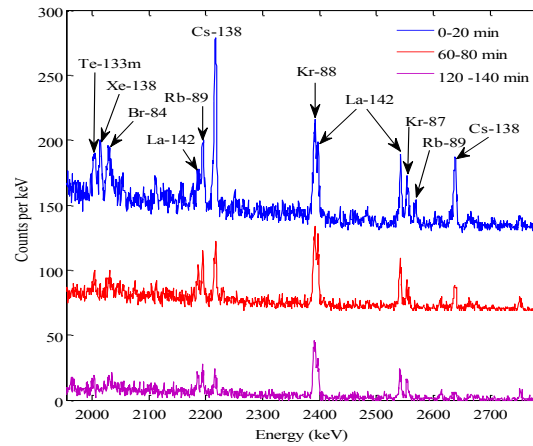


Figure 2.41 Measured delayed gamma spectra with the list-mode system (2.0 MeV-2.7 MeV, DU).

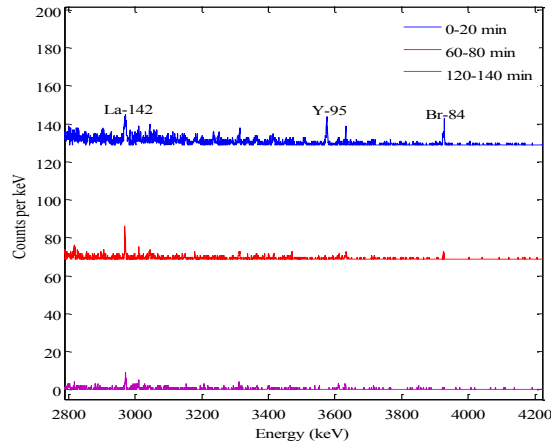


Figure 2.42 Measured delayed gamma spectra with the list-mode system (2.8 MeV-4.2 MeV, DU).

Table 2.4 Measured photofission product yields of ^{238}U using the list-mode system.

Nuclide	Half-life	Energy (keV)	Relative yield	Uncertainty (%)
^{89}Rb	15.2 m	1031.9	0.015	15
		1248.2	0.013	24
^{134}I	52.5 m	1072.6	0.031	6
^{135}I	6.6 h	1260.4	0.026	6
$^{116\text{m}}\text{In}$	54.3 m	1293.6	0.003	9
^{92}Sr	2.7 h	1383.9	0.017	1
$^{133\text{m}}\text{Te}$	55.4 m	2005.3	0.038	11
^{138}Xe	14.1 m	2015.8	0.018	23
^{142}La	91.1 m	2187.2	0.019	11

		2397.8	0.015	4
¹³⁸ Cs	33.4 m	2218.0	0.026	4
		2639.6	0.025	4
⁸⁸ Kr	2.8 h	2392.1	0.010	3
⁸⁷ Kr	76.3 m	2554.8	0.010	6

3 Monte Carlo simulation of photofission process

3.1 Simulation of delayed γ -rays from photofission using MCNPX 2.7.0

The measured delayed gamma spectra using the list-mode system and those published by P. Sibczynski et al. were compared with simulated results based on MCNPX 2.7.0. Three features including embedded source, tall tagging and LCA were first introduced because they played important roles in the simulation. Then the comparisons between measured and simulated spectra were followed.

3.1.1 Embedded sources

MCNPX 2.7.0 has the capability to allow source distributions to be embedded within each other. The embedded source feature was used to model the LINAC pulses. The format of specifying an embedded source is $sdef\ tme = (d11 < d12)$. Distributions $d11$ and $d12$ are both for the time variable. Distribution $d11$ covers a small time range. This range is repeated to exactly fill the larger time range of distribution $d12$. The parentheses on the definition of the embedded source are optional, which means $sdef\ tme = (d11 < d12)$ is equivalent to $sdef\ tme = d11 < d12$. For the embedded source $sdef\ tme = (d11 < d12)$, the embedded distributions including $d11$ and $d12$ must start at time zero or a fatal error message is issued. If there are three or more distributions defined in the embedded source, such as $sdef\ tme = (d11 < d12 < d13)$, the starting time of distributions $d11$ and $d12$ must be zero. However, distribution $d13$ can have any time range. The embedded distributions should also fit within each other exactly. A fatal error message, “*embedded distribution has improper range*” will appear in the output file of a MCNP run if they don't. The below shows an example of defining an embedded source.

Example:

```
sdef tme= d11<d12<d13
si11 0 1 2
sp11 0 1 0
si12 0 200 300
sp12 0 1 0
si13 0 900
sp13 0 1
```

In this example, there are three distributions defined in the embedded source, $d11$, $d12$ and $d13$. The distribution $d11$ defines a micro pulse in time range between 0 and 2 shakes. It is embedded in the distribution $d12$. The time range of the distribution $d12$ is from 0 to 300 shakes. The distribution $d12$ is then repeated to fill the distribution $d13$. The total time period of the embedded sources as defined in the distribution $d13$ is from 0 to 900 shakes.

3.1.2 Tally tagging

Tally tagging is a new feature in MCNPX 2.7.0. It provides the ability to separate a tally into components based on how and where the scoring particle is produced. However, this feature is only implemented for neutron, photon, and electron tallies. The new keyword, *tag*, is used to specify the tally tagging. The keyword is associated with the parameter, *a*, on the *FTn* tally special treatment card. The *FTn* card is associated with a standard *Fn* tally. The format of the *FTn* card is *FTn tag a*, where *n* is the neutron, electron, or photon tally number, and *a* specifies how scatter is to be treated. There are three choices for the value of the parameter *a*. If *a*=1, all collided particles will lose their tag and that bremsstrahlung and annihilation photons will be included in the bin of collided particles; If *a*=2, all collided particles will lose their tag, but that bremsstrahlung and annihilation photons will be given special tags that allow them to be segregated. If *a*=3, all collided particles will retain their production tag. The *FU* special tally card must be used to provide binning specifications for the tagged tally. Three distinct pieces of tagging information are given on each bin. First, a cell of interest where particles are produced should be known; second, a target nuclide from which the particle is emitted also needed to be provided; third, a reaction of interest should also be given.

The format of the *FU* card when used in association with the tagging treatment is *FUn bin1 bin2 ... binN*, where each tagging *bin_i* has the form *CCCCZZAAA.RRRRR*. *CCCC* is the cell number of interest. *ZZAAA* designates a five-digit isotope identifier for a target nuclide, where *ZZ* represents the atomic number and *AAA* the atomic mass number. The reaction identifier for library interactions is specified by *RRRRR*. Delayed particles from fission of *ZZAAA* in all cells are specified by *ZZAAA.99999*. A cell number can be added to only tally delayed particles produced in that cell. Figure 3.1 shows examples of tally tagging in MCNPX 2.7.0.

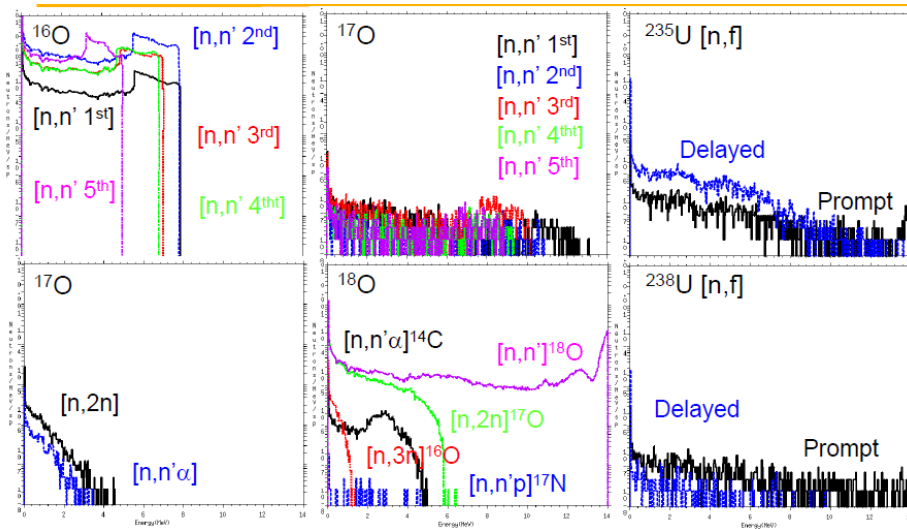


Figure 3.1 Examples of tally tagging in MCNPX 2.7.0[31].

3.1.3 LCA

LCA is used to select the Bertini, ISABEL, CEM03, or INCL4 model. The parameters used in Bertini and ISABEL can also be set by *LCA*. The form of *LCA* is *lca ielas ipreq iexisa ichoic jcoul nexite npidk noact icem ilaq*. The eighth entry on the *LCA* card was set at -2. All other entries on this card were kept at default values. The *LCA* card used in the simulation was *lca 7j -2*. If *noact*=-2 on the *lca* card, table physics is used whenever possible to get the differential data. If it is desired to only get differential data with models, table data can be turned off by setting the *tabl* parameters on the *phys:n* or *phys:h* cards.

3.1.4 Description of the MCNP input file

The simplified geometry model used in the simulations was a sphere with diameter of 1 cm surrounding by vacuum. The sphere was filled with homogenous target, such as DU, HEU and Pu. The enrichment of the HEU target was about 20%. The Plutonium consisted of 95% ²³⁹Pu and 5% ²⁴⁰Pu. The photon source with energy of 12 MeV was located in the center of the sphere. The importance of neutron and photon within the sphere was set as 1. Neutron was not tracked once it escaped out the target. The neutron physics card in the simulation was *phys: n 3j -101*. The third entry *dnb=-101* on this card was used to control delayed neutron production from fission using the CINDER90 models only. The ACE libraries were deprecated in this case. All other entries in the neutron physics card were kept at default values. The *phys: p 3j 1j -102* was the photon physics card in the simulation. The analog photonuclear particle production was enabled by setting the fourth entry (i.e. *ispn*) on this card to -1. The models based on line emission data controlled by the sixth entry *dgb=-102* was used to perform analog sampling of delayed gammas. Simulation time could be much longer when using the models based on line emission data compared with the models based on 25-group emission data. The Activation Control Card *act fission=all nonfiss=none dn=model dg=lines* was to control the production of delayed neutron and photon from residuals created by thermal fission or photofission. The entry *fission=all* on the *ACT* card enabled creation of all delayed particles from fission events. Production of delayed neutron and photon from non-fission events were disabled by the second entry *nonfiss=none*. The entries *dn=model* and *dg=lines* on the *ACT* card had the same functionality as the entries *dnb=-101* and *dgb=-102* on the physics cards. *LCA* is used to select the Bertini, ISABEL, CEM03 or INCL4 model. The parameters used in Bertini and ISABEL can also be set by *LCA*. The form of *LCA* is *lca ielas ipreq iexisa ichoic jcoul nexite npidk noact icem ilaq*. The eighth entry on the *LCA* card was set at -2. All other entries on this card were kept at default values. The *LCA* card used in the simulation was *lca 7j -2*. If *noact*=-2 on the *lca* card, table physics is used whenever possible to get the differential data. If it is desired to only get differential data with models, table data can be turned off by setting the *tabl* parameters on the *phys:n* or *phys:h* cards. The tally card F1 was used to count the delayed gammas on the sphere surface. The tally energy card *e1 1 6000i 5* restricted the energy range of the F1 tally from 1 MeV to 5 MeV and divided the F1 tally into 6002 bins. The tally time card *t1 100 1e37* separated the F1 tally into three time bins -∞ shakes to 100 shakes, 100 shakes to 1e37 shakes and 1e37

shakes to $+\infty$ shakes. Two special tally cards (i.e. *FT* card and *FU* card) were also added to enhance the functionality of the tally card *F1*. The combination of the *ft1 tag 1* and *ful ZZAAA.99999* separated delayed gammas created from fission of the isotope *ZZAAA* from the *F1* tally. The total number of histories to be run in the simulation was $1e8$ which was large enough to have statistical error of less than 0.1. Fig. 13 shows the comparison of the simulated delayed gamma spectra from fission of DU.

3.1.5 Comparison with the delayed γ -ray spectra measured in between linac pulse

The comparisons between the measured and simulated delayed gamma spectra ranging from 2.6 MeV to 5.0 MeV from photofission of ^{238}U are present in Figures 3.2 and 3.3. As shown in these Figures, the measured peaks were successfully predicted in the simulation. However, one notable peak (2971.0 keV) in the simulation results was not observed in the measured spectra. Table 3.1 shows the comparison between measured and simulated intensities with efficiency corrected of the identified peaks relative to the 3287.6 keV peak. The relative intensities of multiple peaks, 2717.3 keV (^{95}Sr), 2941.3 keV (^{98}Y), 3310.0 keV (^{98}Y), 3383.2 keV (^{90}Rb), 3401.3 keV (^{97}Y), 3534.2 keV (^{90}Rb), 3549.5 keV (^{97}Y), 3576.0 keV (^{95}Y), 3599.7 keV (^{91}Rb), 3932.4 keV (^{88}Br), 4078.3 keV (^{91}Rb), 4135.5 keV (^{90}Rb), 4166.3 keV (^{89}Br), 4180.5 keV (^{87}Br), 4365.9 keV (^{90}Rb), and 4450.2 keV (^{98}Y), obtained from the simulation agree well with those from the measured results. However, large discrepancies exist in many peaks, including 2789.3 keV (^{106}Tc), 2868.9 keV (^{136}I), 2933.1 keV (^{95}Sr), 3317.0 keV ($^{90\text{m}}\text{Rb}$), 3458.2 keV (^{93}Rb), and 3867.6 keV (^{93}Rb). The quantitative comparison provides evidence that the Monte Carlo simulation package MCNPX 2.7.0 has capabilities and limitations in the simulation of photofission process.

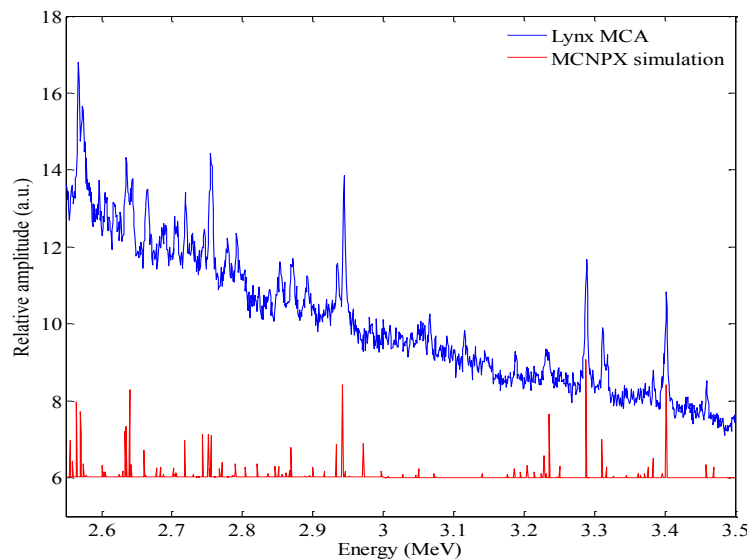


Figure 3.2 Comparison between the measured delayed gamma spectra and simulated results (2.6 MeV-3.5 MeV, ^{238}U).

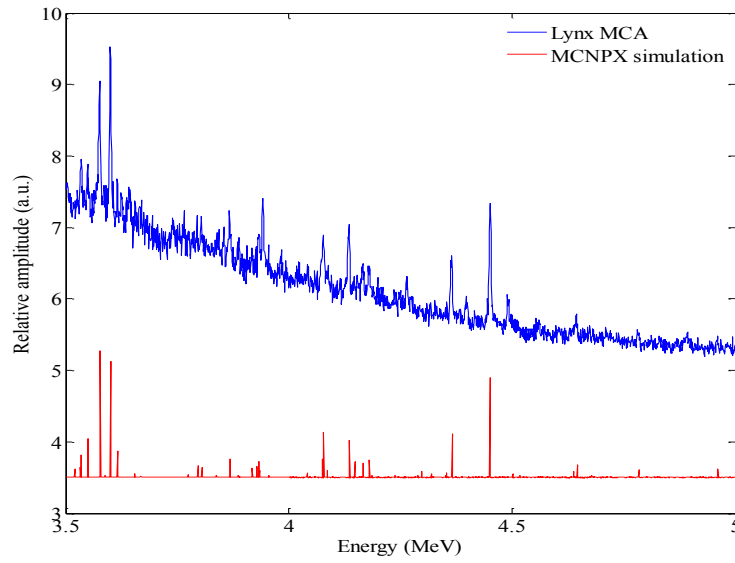


Figure 3.3 Comparison between the measured delayed gamma spectra and simulated results (3.5 MeV-5.0 MeV, ^{238}U).

Table 3.1 Efficiency corrected intensities relative to the 3287.6 keV peak.

Isotope	$T_{1/2}$ (seconds)	Energy (keV)	Measured (^{238}U)	Error (%)	Simulated (^{238}U)	Error (%)
^{95}Sr	23.90	2717.3	0.367	19	0.320	0.6
^{106}Tc	35.6	2789.3	0.585	11	0.165	1.0
^{136}I	83.4	2868.9	0.491	17	0.322	0.7
^{95}Sr	23.9	2933.1	0.375	18	0.282	0.7
^{98}Y	0.548	2941.3	0.997	9	0.784	0.5
^{97}Y	3.75	3287.6	1	6	1	0.4
^{98}Y	0.548	3310.0	0.428	13	0.323	0.6
$^{90\text{m}}\text{Rb}$	258	3317.0	0.213	20	0.088	1.1
^{90}Rb	158	3383.2	0.168	18	0.169	0.8
^{97}Y	3.75	3401.3	0.868	10	0.783	0.5
^{93}Rb	5.84	3458.2	0.170	21	0.113	1.0
^{90}Rb	158	3534.2	0.137	27	0.161	1.0
^{97}Y	3.75	3549.5	0.177	33	0.178	0.8
^{95}Y	618	3576.0	0.491	10	0.576	0.5
^{91}Rb	58.4	3599.7	0.590	10	0.529	0.5
^{93}Rb	5.84	3867.6	0.140	18	0.085	1.1
^{88}Br	16.34	3932.4	0.166	25	0.157	1.2
^{91}Rb	58.4	4078.3	0.235	17	0.206	0.8
^{90}Rb	158	4135.5	0.215	13	0.169	0.8

^{89}Br	4.35	4166.3	0.079	28	0.066	1.3
^{87}Br	55.6	4180.5	0.093	25	0.081	1.2
^{90}Rb	158	4365.9	0.266	13	0.198	0.8
^{98}Y	0.548	4450.2	0.559	9	0.456	0.6

3.1.6 Comparison with the delayed γ -ray spectra measured after irradiation

The comparisons between the MCNPX simulation results and the low-energy delayed γ -ray spectra measured from photofission of ^{238}U and ^{239}Pu using the list-mode system are shown in Figures 3.4-3.18. It is observed that some peak lines are measured in the experiments, however, they are not predicted by simulation or over-predicted/under-predicted. Also, some lines that are predicted by simulation are not observed in the measurements.

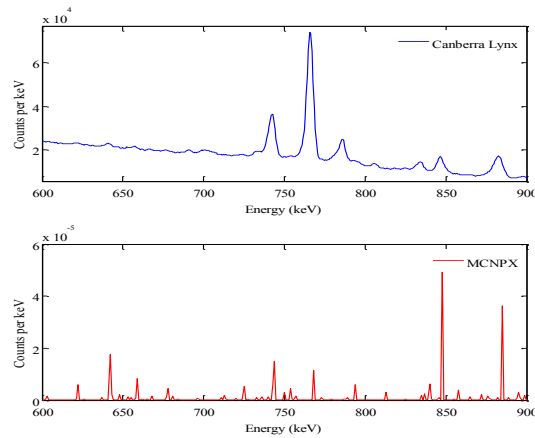


Figure 3.4 Comparison between measured and simulated delayed gamma spectra (0.6 MeV-0.9 MeV, ^{238}U).

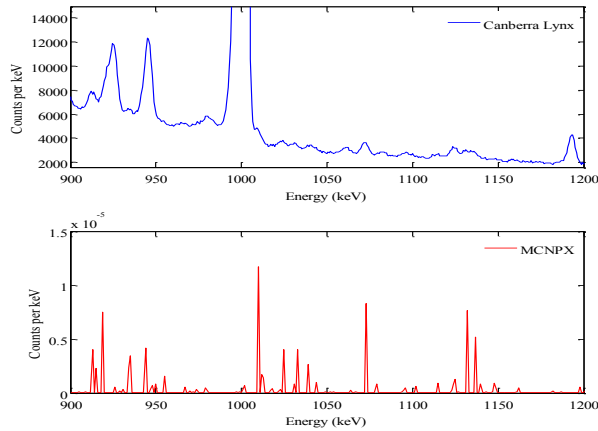


Figure 3.5 Comparison between measured and simulated delayed gamma spectra (0.9 MeV-1.2 MeV, ^{238}U).

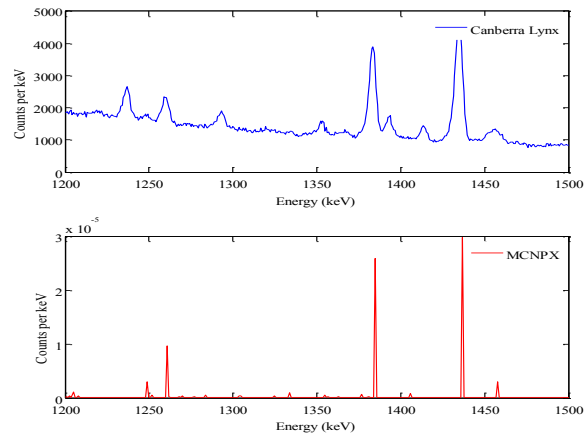


Figure 3.6 Comparison between measured and simulated delayed gamma spectra (1.2 MeV-1.5 MeV, ^{238}U).

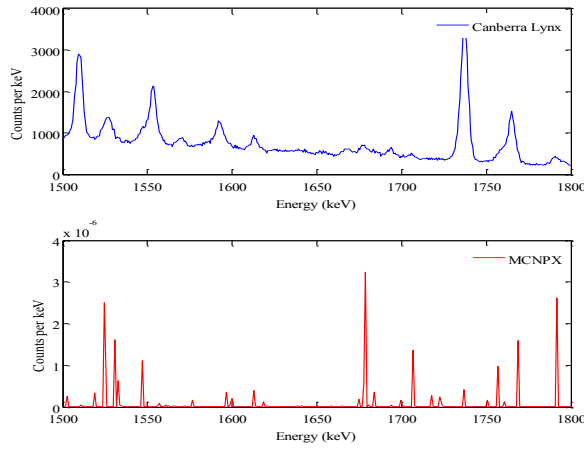


Figure 3.7 Comparison between measured and simulated delayed gamma spectra (1.5 MeV-1.8 MeV, ^{238}U).

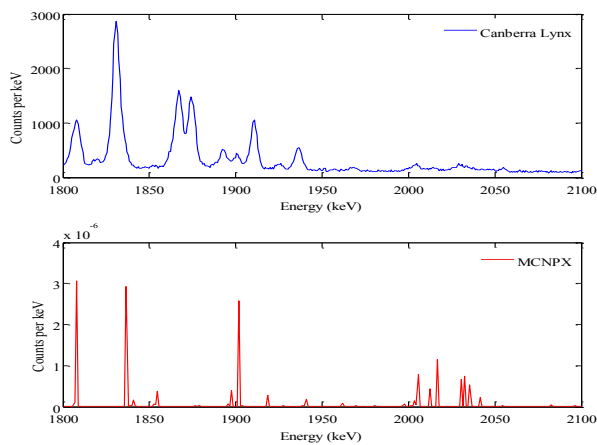


Figure 3.8 Comparison between measured and simulated delayed gamma spectra (1.8 MeV-2.1 MeV, ^{238}U).

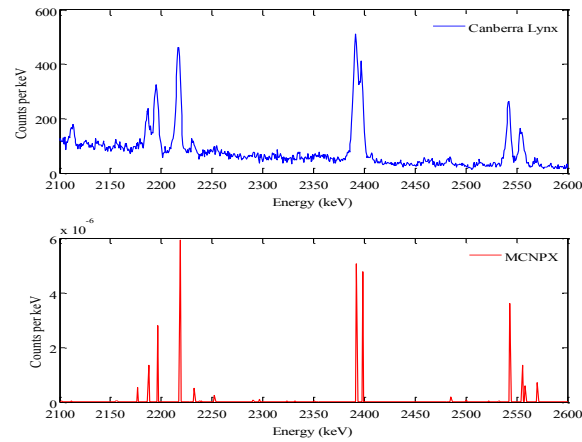


Figure 3.9 Comparison between measured and simulated delayed gamma spectra (2.1 MeV-2.6 MeV, ^{238}U).

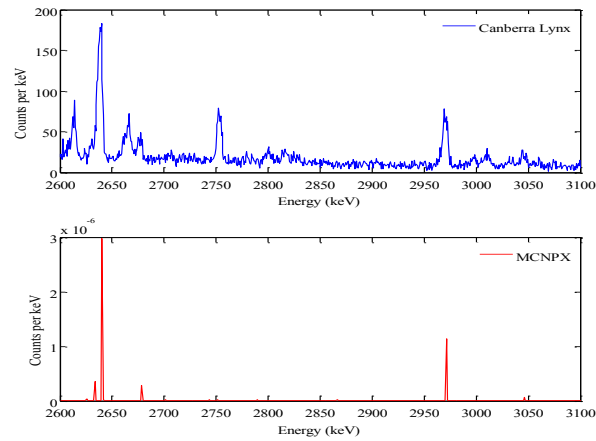


Figure 3.10 Comparison between measured and simulated delayed gamma spectra (2.6 MeV-3.1 MeV, ^{238}U).

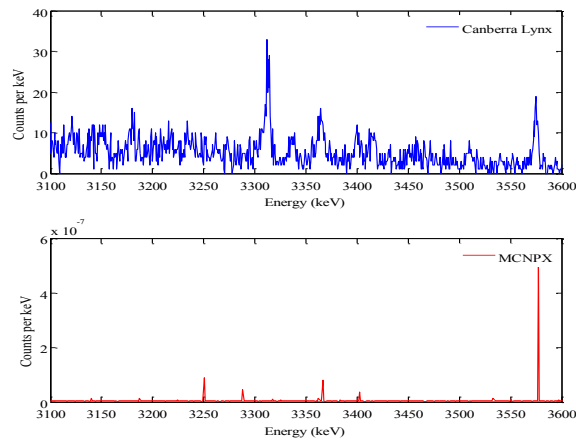


Figure 3.11 Comparison between measured and simulated delayed gamma spectra (3.1 MeV-3.6 MeV, ^{238}U).

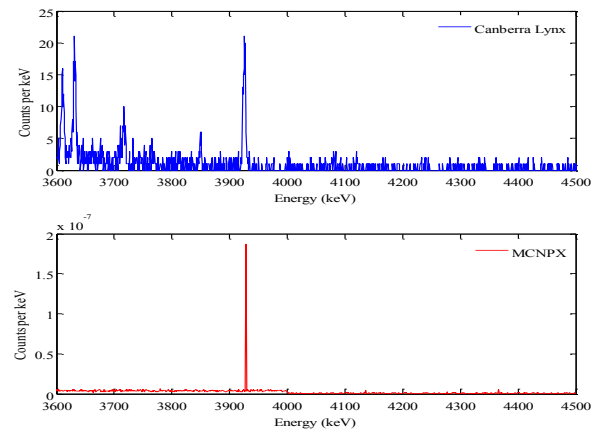


Figure 3.12 Comparison between measured and simulated delayed gamma spectra (3.6 MeV-4.5 MeV, ^{238}U).

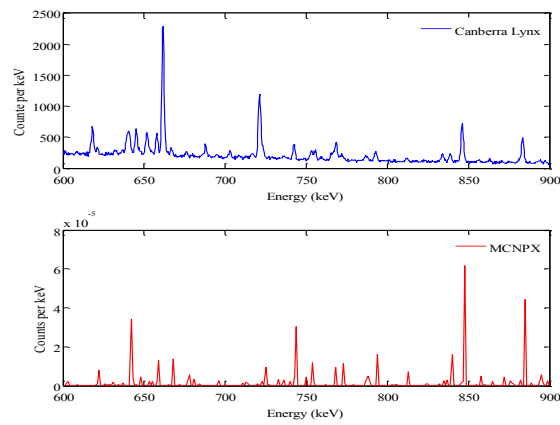


Figure 3.13 Comparison between measured and simulated delayed gamma spectra (0.6 MeV-0.9 MeV, ^{239}Pu).

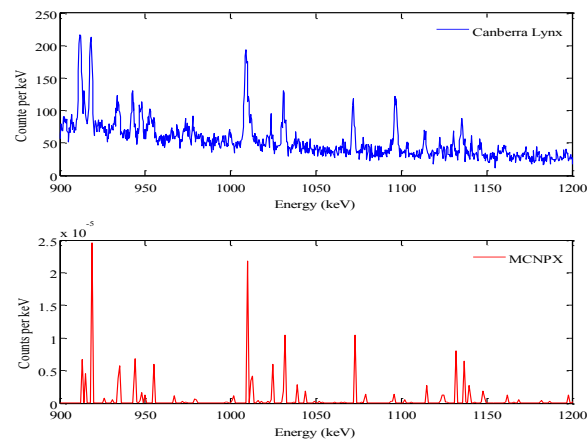


Figure 3.14 Comparison between measured and simulated delayed gamma spectra (0.9 MeV-1.2 MeV, ^{239}Pu).

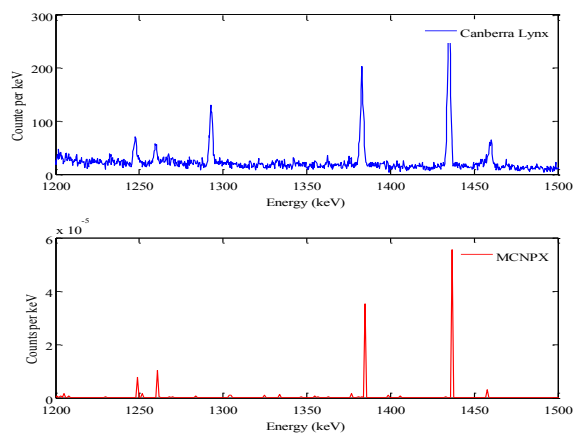


Figure 3.15 Comparison between measured and simulated delayed gamma spectra (1.2 MeV-1.5 MeV, ^{239}Pu).

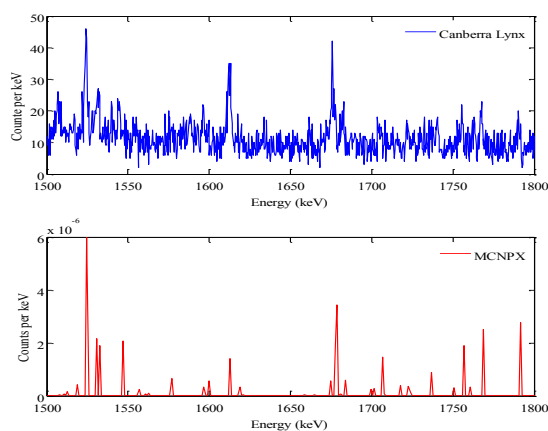


Figure 3.16 Comparison between measured and simulated delayed gamma spectra (1.5 MeV-1.8 MeV, ^{239}Pu).

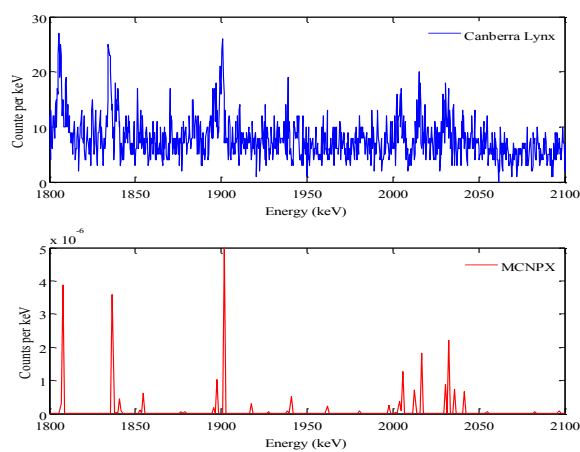


Figure 3.17 Comparison between measured and simulated delayed gamma spectra (1.8 MeV-2.1 MeV, ^{239}Pu).

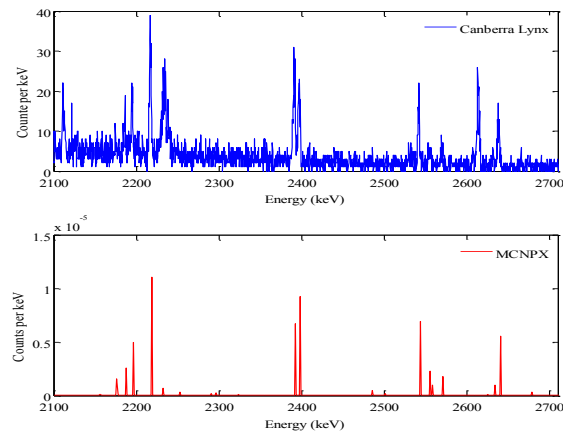


Figure 3.18 Comparison between measured and simulated delayed gamma spectra (2.1 MeV-2.7 MeV, ^{239}Pu).

3.1.7 Comparison between the delayed γ -rays spectra published by P. Sibczynski et al. and simulated results

The published delayed gamma spectra for HEU by P. Sibczynski et al. from the National Centre for Nuclear Research in Poland were also compared with simulation results based on MCNPX 2.7.0. The comparisons between measure and simulated delayed gamma spectra are shown in Figures 3.19-3.24. It was also observed that some peaks that were predicted in simulation were not present in measured spectra or over/under predicted and some peaks were not predicted in simulation but they were shown in measured spectra.

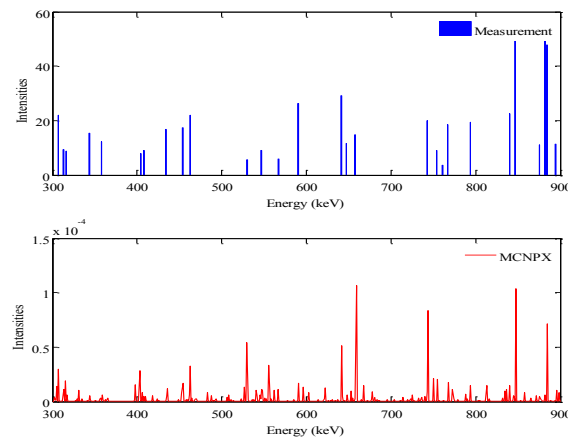


Figure 3.19 Comparison between the delayed γ -ray spectra published by P. Sibczynski et al. and simulation results (0.3 MeV-0.9 MeV, HEU).

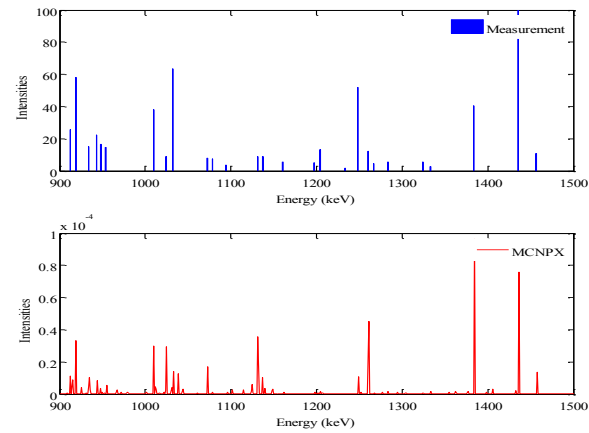


Figure 3.20 Comparison between the delayed γ -ray spectra published by P. Sibczynski et al. and simulation results (0.9 MeV-1.5 MeV, HEU).

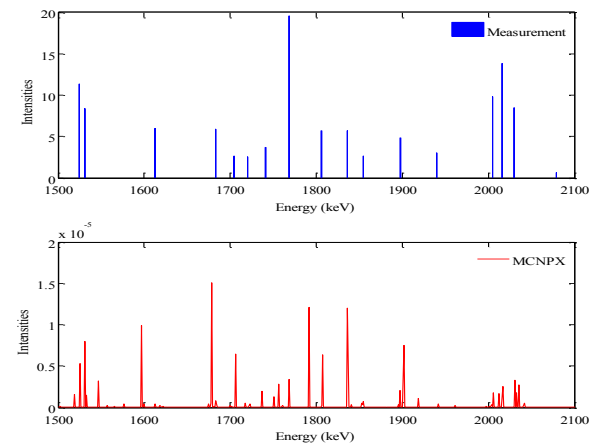


Figure 3.21 Comparison between the delayed γ -ray spectra published by P. Sibczynski et al. and simulation results (1.5 MeV-2.1 MeV, HEU).

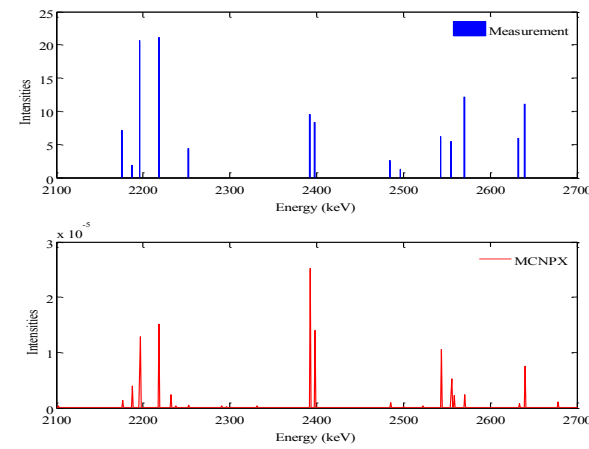


Figure 3.22 Comparison between the delayed γ -ray spectra published by P. Sibczynski et al. and simulation results (2.1 MeV-2.7 MeV, HEU).

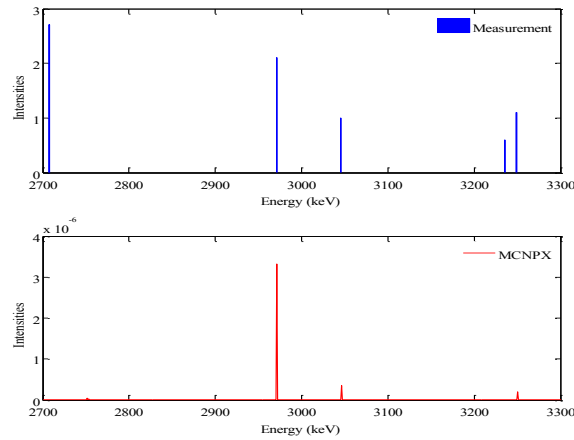


Figure 3.23 Comparison between the delayed γ -ray spectra published by P. Sibczynski et al. and simulation results (2.7 MeV-3.3 MeV, HEU).

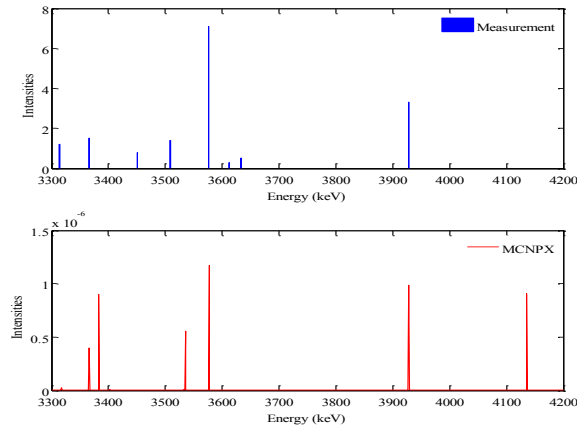


Figure 3.24 Comparison between the delayed γ -ray spectra published by P. Sibczynski et al. and simulation results (3.3 MeV-4.2 MeV, HEU).

3.2 Simulation of delayed γ -rays from photofission using FLUKA

FLUKA is a general purpose Monte Carlo simulation code designed for particle transport and interactions with matter over broad ranges of energies. It has a wide range of applications covering from proton and electron accelerator shielding to target design, calorimetry, activation, dosimetry, detector design, accelerator driven systems, cosmic rays, neutrino physics, radiotherapy etc. The delayed γ -rays from photofission of ^{238}U were simulated using FLUKA. The description of input file written using the graphical user interface flair is given in detail below.

Various physics settings are available in FLUKA for specific application. A summary of the physics settings is shown below. The physics setting and beam properties are present in Figure 3.25. In the simulation the physics setting used in the simulation was *PRECISIO*. The photon

beam energy was 12 MeV. The FWHM of the momentum distribution was zero. There were not beam spreadth along x and y directions (i.e. point-like source). The x, y and z coordinates of the source were 0, 0 and -2, respectively. The direction cosines with respect to the x-axis and y-axis were 0.

CALORIME: calorimeter simulations

EET/TRAN: Energy Transformer or transmutation calculations

EM-CASCA: pure EM cascades

ICARUS: studies related to the ICARUS experiment

HADROTHE: hadrotherapy calculations

NEUTRONS: pure low-energy neutron runs

NEW-DEFA: reasonable minimal set of generic defaults

PRECISIO: precision simulations

SHIELDIN: pure hadron shielding calculations

TITLE Photofission			
GLOBAL			
Max #reg:	Analogue:	DNear:	
Input:	Geometry:		
Set the defaults for precision simulations			
DEFAULTS PRECISIO			
Define the beam characteristics			
BEAM	Beam: Energy	E: 12.0	Part: PHOTON
Δp : Flat	Δp : 0.0	$\Delta \phi$: Flat	$\Delta \phi$: 0.0
Shape(X): Rectangular	Δx : 0.0	Shape(Y): Rectangular	Δy : 0.0
Define the beam position			
BEAMPOS	x: 0.0	y: 0.0	z: -2.0
	cosx: 0.0	cosy: 0.0	Type: POSITIVE

Figure 3.25 Beam description in the FLUKA simulation.

The geometry model is described in Figure 3.26. The target was a sphere with diameter of 1 cm. It was surrounded by a void sphere with diameter of 1×10^4 cm. A large sphere (diameter is 1×10^5 cm) was added to produce a blackbody. The importance of neutron and photon within the target and void were set at 1. It was set as 0 in the outside of the blackbody. Neutron and photon were not tracked once they exited the blackbody.

GEOBEGIN		Log:	Acc:	Opt:
Title:		Inp:	Out:	Fmt: COMBNAME
Black body				
SPH	blkbody	x: 0.0	y: 0.0	z: 0.0
		R: 100000.0		
Void sphere				
SPH	void	x: 0.0	y: 0.0	z: 0.0
		R: 10000.0		
SPH	target	x: 0.0	y: 0.0	z: 0.0
		R: 1.0		
END				

Black hole			
REGION BLKBODY		Neigh: 5	Volume:
expr: +blkbody -void			
Void around			
REGION VOID		Neigh: 5	Volume:
expr: +void -target			
Target			
REGION TARGET		Neigh: 5	Volume:
expr: +target			
END			
GEOEND			

Figure 3.26 Geometry description in the FLUKA simulation.

Figure 3.27 shows the material description in the simulation. The target was filled with ^{238}U . The density of the target was 19.1 g/cm^3 . The void and blackbody regions were filled with default materials (i.e. void, blkbody). The *LOW-MAT* card set the correspondence between FLUKA materials and low-energy neutron cross-sections. By default, the link is between the FLUKA material and the first material of the same name present in the library. In the simulation the material at temperature 296K was used.

MATERIAL	Name: U	#	p: 19.1
Z: 92.0	Am: 238.0	A:	dE/dx: ▼
LOW-MAT	Mat: U ▼	LowMat: 238U. Uranium 238, 296K ▼	
1...2...3...4...5...6...7..			
ASSIGNMA	Mat: BLCKHOLE ▼	Reg: BLKBODY ▼	to Reg: ▼
	Mat(Decay): ▼	Step: ▼	Field: ▼
ASSIGNMA	Mat: VACUUM ▼	Reg: VOID ▼	to Reg: ▼
	Mat(Decay): ▼	Step: ▼	Field: ▼
ASSIGNMA	Mat: U ▼	Reg: TARGET ▼	to Reg: ▼
	Mat(Decay): ▼	Step: ▼	Field: ▼

Figure 3.27 Material description in the FLUKA simulation.

The photonuclear physics was activated by the *PHOTONUC* card in the FLUKA simulation, as shown in Figure 3.28. *MUPHOTON* card instead of *PHOTONUC* card should be used to handle the muon photonuclear interactions via virtual photons. The analog simulations of photonuclear interactions are very inefficient because photonuclear cross-sections are much smaller than photon cross-sections for electromagnetic interactions with atoms and electrons. The *LAM-BIAS* card was combined with the *PHOTONUC* card to artificially increase the probability to have photonuclear reactions.

PHOTONUC	Type: ELECTNUC ▼	Quasi D On ▼	All E: off ▼
E>0.7GeV off ▼	Δ resonance On ▼	to Mat: ▼	Giant Dipole On ▼
	Mat: U ▼	x mean life: 0.0	Step: ▼
LAM-BIAS	Type: INEPRI ▼	to Part: ▼	x λ inelastic: 0.02
Mat: U ▼	Part: PHOTON ▼		Step: ▼
USRBDX	Reg: TARGET ▼	Unit: 21 BIN ▼	Name: Photon
Type: I1, LinE, LinΩ ▼	to Reg: VOID ▼	to Reg: VOID ▼	Area: 1.0
Part: PHOTON ▼	Emin: 0.001	Emax: 0.005	Ebins: 1096.0
	Qmin: ▼	Qmax: ▼	Qbins: ▼

Figure 3.28 Photonuclear physics description in the FLUKA simulation.

Figure 3.29 shows the tally description used in the FLUKA simulation. The *DCYTIMES* card defined the cooling time before tallying. The *DCYSCORE* card was used to associate scoring detectors (radio-nuclides, fluence, dose) with different cooling times. The *RANDOMIZ* card was

used to initialize the random seed sequences. Different sequences can be initialized by changing the *WHAT(2)* entry on the *RANDOMIZ* card. This card can also be used to perform parallel simulations. The *USRTRACK* card was used to tally delayed gammas. It defined a detector for a track-length fluence estimator. The results of the *USRTRACK* track-length estimator were given as differential distributions of fluence in energy, in units of $\text{cm}^{-2} \text{GeV}^{-1}$ per incident primary unit weight. If the generalised particle is 208.0 (ENERGY) or 211.0 (EM-ENRGY), the quantity scored is differential energy fluence, expressed in GeV per cm^2 per energy unit per primary. The maximum number of track-length collision detectors that can be defined in a single input file is 400. However, this value can be changed by modifying the parameter *MXUSTC* in the *flukaadd* library or directory and then re-compiling and linking Fluka. The number of particle histories defined in the *START* card was 500. When the stop card is inserted before *START* card it can be used to prevent reading input and de-activating all following cards. In this case no particle transport will be performed, this feature is useful for geometry debugging. After the *START* card, its presence is optional and has no effect. Figure 3.30 shows the simulated delayed gamma spectra from photofission of ^{238}U . As shown in Figure 3.30, there are not discrete gamma peak lines. This could be due to lack of line-emission data in the FLUKA data library.

DCYTIMES	t1: 0.00001 t4:	t2: t5:	t3: t6:
DCYSCORE	Cooling t: 0.00001 Det: Photon	Kind: USRTRACK to Det: Photon	Step:
USRTRACK	Type: Linear Part: PHOTON	Unit: 22 BIN Emin: 0.001 Emax: 0.005	Name: Photon Vol: 1.0 Bins: 4096.0
Set the random number seed			
RANDOMIZ	Unit 01	Seed: 1111111 0	
Set the number of primary histories to be simulated in the run			
START	No.: 500.0 Time:	Cor:	Report: default
STOP			

Figure 3.29 Tally description in the FLUKA simulation.

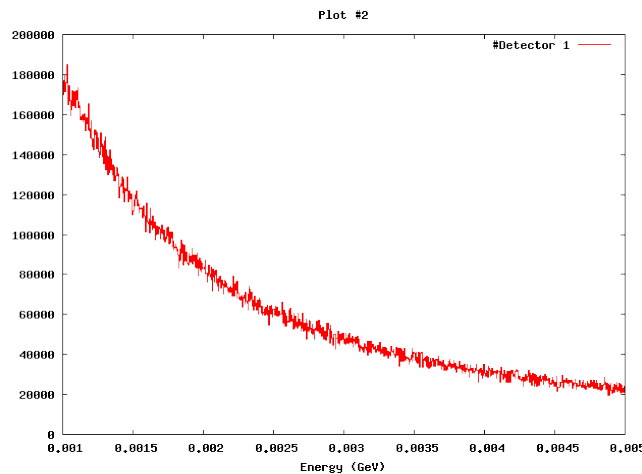


Figure 3.30 Simulated delayed gamma spectrum from photofission of ^{238}U using FLUKA.

4 High-throughput spectroscopy system for high-rate applications

4.1 Modifications to the HPGe preamplifier

4.1.1 Modifications to the feedback resistor

Two Canberra n-type coaxial high-purity germanium detectors (Model number GC4020, the size is 2.4" by 2.3") detectors with relative efficiency of 40% were used in our development of high-throughput high-resolution γ -ray spectroscopy system. In support of demonstrating the performance, such as throughput rate, energy resolution, of the detector with a modified pre-amplifier, modification was not made to one of the detectors so that it had a standard front-end electronics and could serve as a reference detector. A picture of the front-end electronics is shown in Figure 4.1. The FET, feedback resistor and capacitor which were originally mounted on the detector cryostat were moved to the warm side to make the modification practicable. As a result, a degradation of energy resolution could result from the exposure of the FET to room temperature. Before modifying the front-end electronics in practice, the responses of the pre-amplifier with different feedback resistor values and RC constants to a linac pulse plus the step current pulses were simulated with LTspice. The energy rate of RC feedback pre-amplifier is a function of the feedback resistor value and the dynamic output voltage range of the integrator. A lower value feedback resistor can substantially increase the energy rate limitation. After a change made to the feedback resistor, it was a requirement that the resistors in the pole-zero cancellation network be adjusted to make the pole due to the pulse decay time of the pre-amplifier cancelled by the zero of this network. An incomplete pole-zero cancellation could cause excessive dead time due to sufficiently large undershoot and degradation of energy resolution. A waveform of the output signal from the pre-amplifier with a single exponential decay time should be observed when pole-zero cancellation is completed. One disadvantage of performing measurement shortly after a linac pulse is the interference from neutron-capture γ -rays produced in surrounding materials and/or nuclear sample itself. As reported in our previous work, a significant amount of neutron-capture γ -rays were still being emitted within about 5 milliseconds after each linac pulse. An effective approach to address this issue is to measure active background from walls, shielding materials and so on by keeping the same experimental setup including interrogation source, detectors, geometry, shielding and DAQ system except removing nuclear sample from irradiation. The measured active background spectrum should then be subtracted to obtain a clean delayed γ -rays energy spectrum.

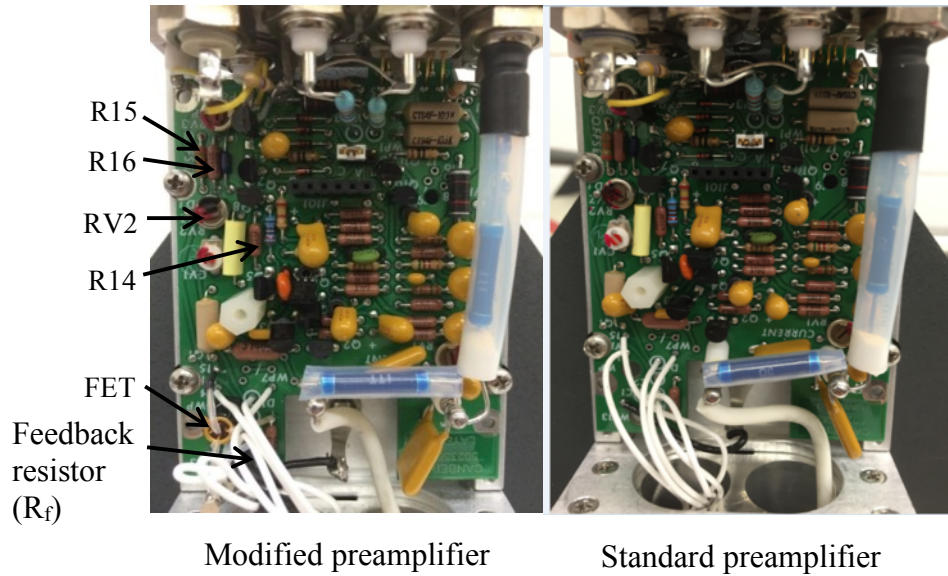


Figure 4.1 The standard and modified preamplifiers.

It is well known that the energy rate of a RC feedback preamplifier is a function of the feedback resistor value and the dynamic range of the output voltage range of the charge integrator. The energy rate can be derived from the equation below provided the value of feedback resistor and the voltage range.

$$\text{Energy rate} \left(\frac{\text{MeV}}{s} \right) \times 10^6 \left(\frac{eV}{\text{MeV}} \right) \times \frac{1}{W \left(\frac{eV}{\text{IonPair}} \right)} \times 1.6 \times 10^{-19} \left(\frac{\text{Coulombs}}{\text{IonPair}} \right) \times R_f (\text{Ohm}) = V (\text{Volt})$$

Recently, a group from Pacific Northwest National Laboratory demonstrated improvement of energy rate by changing the V in the equation above from -24 V to -100 V. In our work, a lower value feedback resistor (i. e. 0.5 GOhm vs 2 GOhm) was proved to substantially increase the energy rate limitation both in LTspice simulation and actual photofission environment. Before actual modification, the system response was first studied via simulation, with different feedback resistor values. A detailed model of the pre-amplifier was built in LTspice. Stimulus source was generated in the form of text file using a customized script developed in Visual Basic programming language. The stimulus used in the simulation was a current source of 2.5×10^{-5} Amp with duration of $4 \mu s$ simulating the large injection from linac and gamma rays of 1 MeV at input count rate of 50 kcps following the large injection. Both rise time and fall time of the current source were set to 10 ns. The stop time and maximum time step in the transient simulation mode of LTspice were 20 m and $10 \mu s$, respectively. As shown in Figure 4.2, the saturation time following each linac pulse was reduced from 8.7 milliseconds to about 1.8 milliseconds when the value of the feedback resistor of the preamplifier was changed from 2 GOhm to 0.5 GOhm. This means that the detector could recover more rapidly after saturation caused by large energy

deposition from the linac pulse. This is beneficial to many applications using photonuclear techniques such as measurements of delayed γ -rays emitted by fission fragment shortly after shutdown of the linac pulses after photon-induced fission and capture gamma rays from the (n, γ) reaction. The reduced saturation time of the preamplifier was verified in a photofission environment during the testing at Idaho Accelerator Center. Figure 4.3 presents the measured signals from both the modified and standard preamplifiers in the photofission environment. The 3 g Plutonium was used as the target. The other experimental setup could be referred to the description in the section 1. The signals from the preamplifiers were digitized by the digitizer PXIe-5122 from National Instruments at a sampling rate of 30 MHz and then transferred to PC for off-line processing in Matlab. The measured saturation time of the modified preamplifier following a linac pulse was 2.7 ms, which was much shorter than that of the standard preamplifier (i.e. 5.7 ms). One major factor for the discrepancy between the simulation and experimental results was that the LTspice simulation model could not exactly match the actual design of the preamplifier.

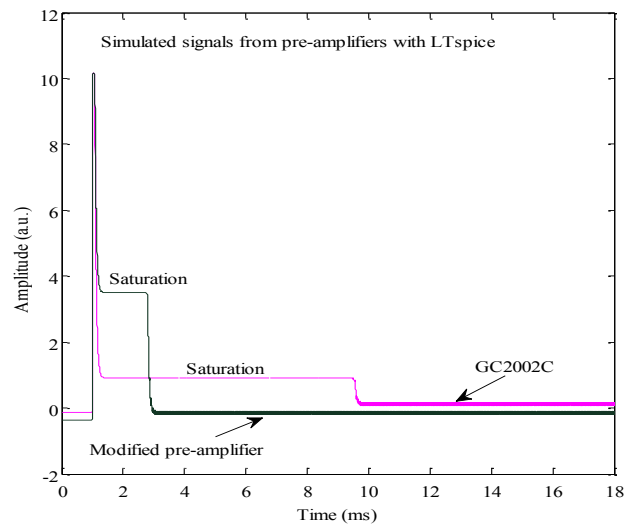


Figure 4.2 Simulated saturation times of the modified and standard preamplifiers with LTspice.

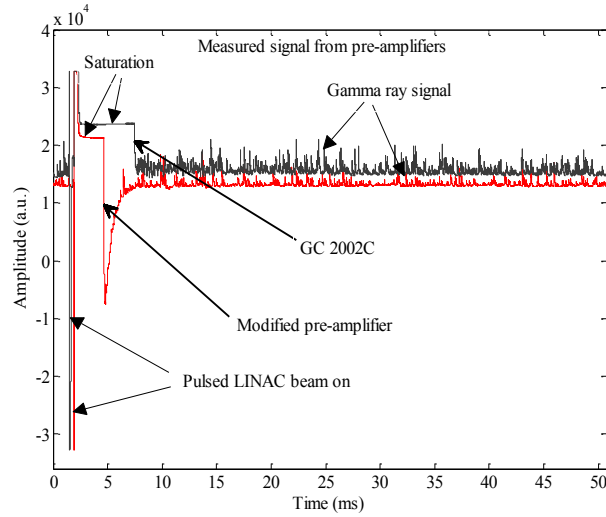


Figure 4.3 Measured signals from both the modified and standard preamplifiers at a photofission environment.

4.1.2 Modification to the tail time

The modification to reduce the tail time of the final output signal and its impact on baseline shift are described in detail below. In this work, the tail time was reduced from 50 μs to 10 μs . A comparison between the signals before and after this modification is illustrated in Figure 4.4. During the measurement, a ^{137}Cs source was placed close to the detectors to achieve an input count rate of 20 kcps. The NI PXIe-5122 system was used to acquire the signals from the preamplifiers at sampling rate of 50 MSPS. As shown in Figure 4.4, the signal from the modified preamplifier decays much faster than that from the standard preamplifier. For simplicity, the reduction of the tail time was achieved by changing the values of resistors R14 and R16 from 499 Ω to 99 Ω . This approach is easy to implement, however, it dramatically increases the DC gain and reduces the effective input dynamic range. In the future, the same reduction of the tail time can be achieved by reducing the value of the capacitor Cpz in the P/Z network, without affecting the DC gain. The effect of the reduced tail time (10 μs) by changing the capacitor on baseline shift was studied with LTSpice simulations. The stimulus source was a train of current pulses at rate of 5×10^6 cps, each of which simulated the charge produced by gamma ray of 1 MeV. The offset time of the stimulus source was 0.014 ms. The rise time and fall time of each current pulse were both set at 5 ns. The amplitude of a pulse was 511 nA with a duration of 100 ns. The simulation mode in LTSpice was set at transient to perform a time-domain computation. As shown in Figure 4.5, the baseline of the output signal from the standard preamplifier increases at a much higher rate than that from the modified one and reaches the saturation level within 0.046 ms. Instead, the baseline for the modified preamplifier is only shifted to 3.2 V. Significant reduction of baseline shift could be beneficial to many high-rate applications. For example, in spent nuclear fuel assay applications, the input count rate can often reach 106 cps or higher. Thus a preamplifier with nominal tail time (i.e. 50 μs) would be easily saturated. Instead, as a result of the reduced tail time, the modified preamplifier could potentially be used to

perform spectroscopy measurement and provide valuable information about spent fuel assemblies. In addition, the reduction of baseline shift can also be beneficial when a digitizer with small input range is utilized to acquire waveforms from preamplifiers. For example, a NI PXI-5152 digitizer (input range: ± 5 V) can be used to acquire data from the modified preamplifier at input count rate of 5×10^6 cps. However, the digitizer could be saturated due to the large baseline shift observed from the standard preamplifier.

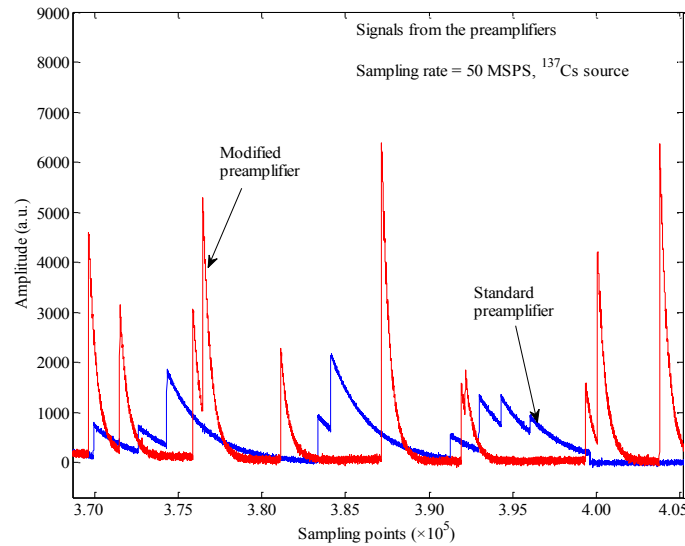


Figure 4.4 Comparison between signal waveforms measured with NI PXI-5122.

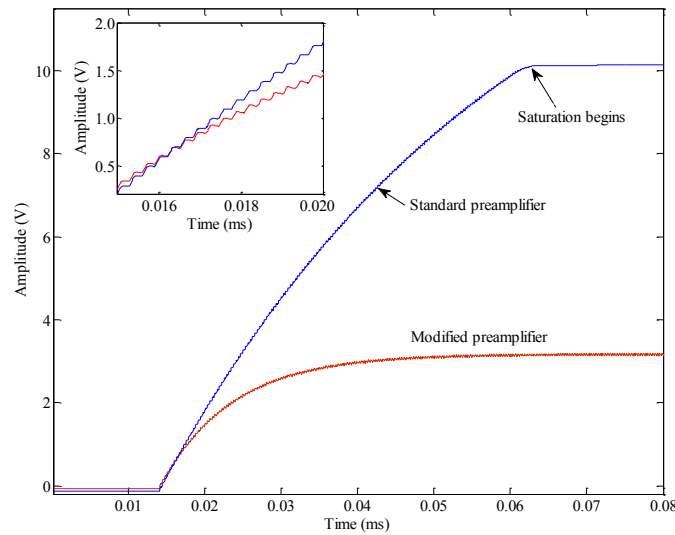


Figure 4.5 The effect of reduced tail time on baseline shift simulated in LTSpice.

In summary, the modifications to a standard preamplifier including reducing the value of feedback resistor and RC constant were demonstrated in our work to be a promising approach to achieve a high-throughput high-resolution gamma spectroscopy system.

4.1.3 Energy resolution after the modifications

The energy resolution of the system after the preamplifier modifications was evaluated using the traditional trapezoidal shaping methods in Matlab [32]. In these measurements, the input count rate from a ^{137}Cs source was kept close to 20 kcps by adjusting the source-to-detector distance. The NI PXIe-5122 system was used to acquire the signals with 14-bit resolution at sampling rate of 50 MSPS. The digitized data was transferred to a PC for off-line signal processing. As an illustration of trapezoidal filtering, Figure 4.6 shows the energy signal shaped with a long shaping times (5.6 μs rise time, 0.8 μs flat top time) to perform energy measurement and the time signal with shorter shaping times (0.1 μs , 0 μs) used to detect the time-of-arrival of each event and perform pile-up rejection. To reduce the impact of ballistic deficit on energy resolution, the flat top time of the trapezoidal filter needs to be longer than the charge collection time [119]. To find the appropriate flat top time empirically, the charge collection time for each event was first estimated using the recursive algorithm for digital pulse shaping [110]. The rise and flat top times used in the algorithm were set at 0.11 μs and 0 μs , respectively. As shown in the inset of Figure 4.10, the time the fast channel takes to reach its maximum after crossing the threshold is considered an estimation of the charge collection time. The result was used to build the histogram shown in Figure 4.7. Based on this histogram, the flat top time was chosen to be 0.8 μs to ensure complete charge collection regardless of the actual charge drifting process. This value was used in all the energy spectra reconstruction in following discussion. A local minimum collection time around 240 ns is observed in Figure 4.10. The observation is likely due to the low sampling rate (i.e. 50 MSPS) and the simplified approach to determine the collection time. In the slow channel for energy measurement, different rise times were used respectively for the standard and modified preamplifiers to optimize energy resolution. Figure 4.8 shows the energy resolution obtained using various rise times. As shown in Figure 4.8, the optimal rise times for the standard and modified preamplifiers were 8 μs and 6 μs , respectively. The energy spectra reconstructed at the optimal rise times are present in Figure 4.9. There was no significant degradation in resolution (2.4 keV vs 2.2 keV @ 662 keV) as a result of moving the FET to the warm side and reducing the feedback resistor and tail time. The authors believe that the smaller feedback resistor (0.5 G Ω vs 2 G Ω) exposed in room temperature environment is the main cause of the shift of the optimal rise time. The equation used to explain the shift is presented as follows [33]:

$$\left(\omega_{\text{parallel}}\right)^2 \propto \left(I_D + \frac{2kT}{R_f}\right) \times T_s$$

Where I_D is the total detector current, k is the Boltzmann constant, T is the temperature of the feedback resistor, R_f is the value of the feedback resistor, T_s is the rise time in the trapezoidal

shaping. As shown in the equation above, extra parallel noise from the feedback resistor needs to be compensated by a short shaping time to obtain the best energy resolution, which leads to the optimal rise time shift.

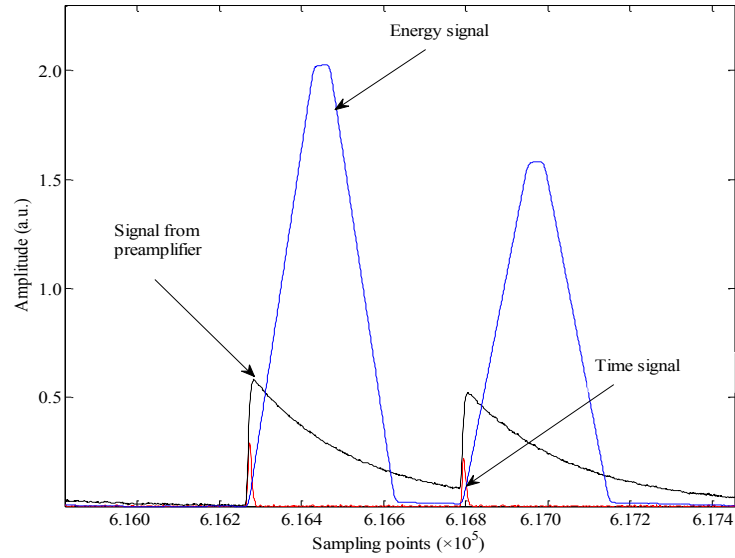


Figure 4.6 Illustration of the time and energy signal shaped in parallel in the trapezoidal filtering.

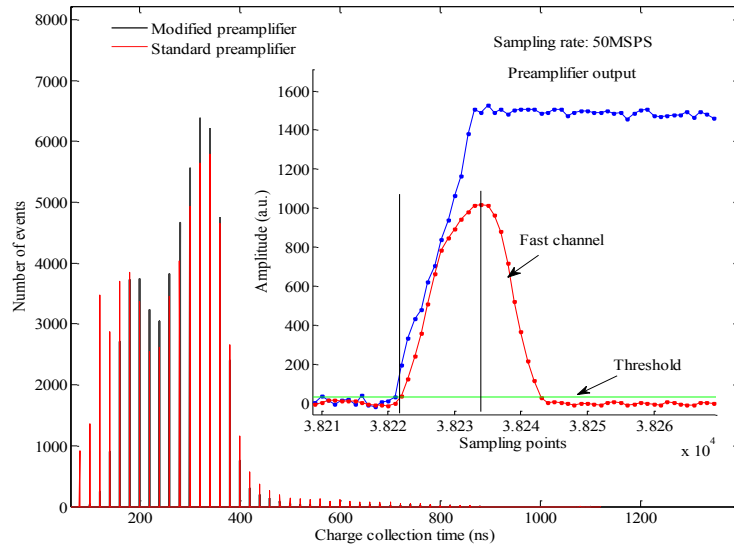


Figure 4.7 Distribution of charge collection time at input count rate of 20 kcps.

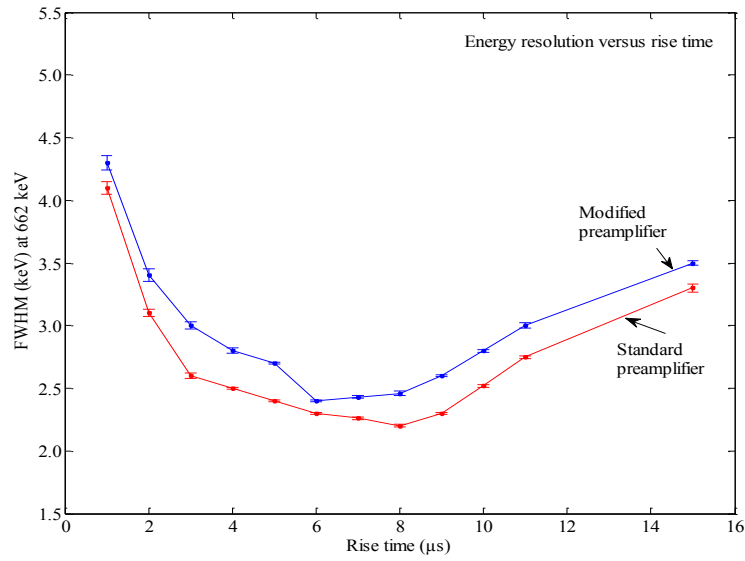


Figure 4.8 Energy resolution versus rise time in the trapezoidal filtering (flat top time was fixed at 0.8 μs).

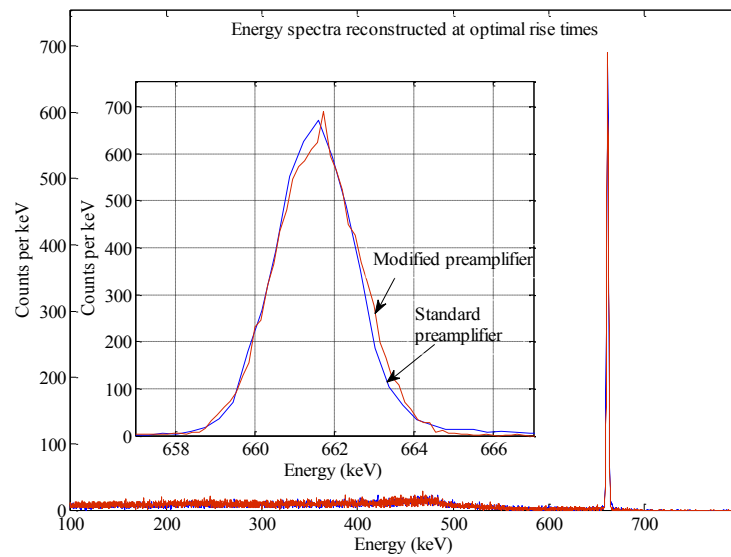


Figure 4.9 Energy spectra reconstructed at optimal rise times (flat top time was fixed at 0.8 μs).

4.1.4 Conclusions

In this work, the modification to the feedback resistor of an HPGe preamplifier were proven to be an effective approach to reduce the saturation time after each linac pulse in a pulsed photonuclear environment. Valuable information only available shortly after the irradiation can be obtained if the preamplifier recovers quickly. In addition, this improvement could be beneficial to applications where high linac repetition rate is utilized. The modification to the tail time can significantly decrease baseline shift, which is important for system stability and performance in high rate situations. After the modifications, only a small degradation in energy

resolution was observed. Moving the FET and feedback components back into the cryostat will likely improve the energy resolution.

4.2 Advanced pulse processing algorithms

4.2.1 Template-matching algorithm

A major challenge in utilizing spectroscopy techniques for nuclear safeguards is to perform high-resolution measurements at an ultra-high throughput rate. Traditionally, piled-up pulses are rejected to ensure good energy resolution. To improve throughput rate, high-pass filters are normally implemented to shorten pulses. However, this reduces signal-to-noise ratio and causes degradation in energy resolution. Recently, pulse pile-up recovery based on template-matching has been proved to be an effective approach to achieve high throughput rate gamma ray spectroscopy.¹ In this paper, we report our independent study on a similar pulse analysis algorithm.

4.2.1.1 Discussion of the algorithm

In an ideal model, the output signal $y(t)$ from a gamma-ray detector is the convolution of the incident signal $s(t)$ and the detector response matrix M : $y(t) = s(t) * M$. Thus, if the response matrix can be accurately determined, an estimation of the incident signal can be obtained via de-convolution. The incident signal is normally modeled as a train of delta functions, with random time of arrival and amplitude. The detector response is considered to be time-invariant and can be pre-determined. The first step of the algorithm discussed here is to determine the time of arrival for each pulse. This can greatly reduce the complexity of the problem. Once the time of arrival is determined, the detection process could be re-written as:

$$\begin{bmatrix} y_1 \\ \vdots \\ y_D \end{bmatrix} = \begin{bmatrix} t_{11} & \cdots & t_{1B} \\ \vdots & \ddots & \vdots \\ t_{D1} & \cdots & t_{DB} \end{bmatrix} \begin{bmatrix} s_1 \\ \vdots \\ s_B \end{bmatrix}$$

Here, s_j ($j = 1, \dots, B$) is a vector containing the amplitude of the B incident pulses, whose time of arrival has been determined in the previous step. y_i ($i = 1, \dots, D$) is the measured signal at time i . D is the length of the digitized waveform. The elements of the response matrix t_{ij} contain the contribution from the j th pulse to the measurement at the i th time point. Assuming the impulse response of the detector could be determined (i.e. the template), the matrix t_{ij} can then be calculated once the time of arrival for each pulse is determined. Each row of the matrix would just be the impulse response with various values of delay. Ideally, since y_i is measured and t_{ij} can be calculated based on the known impulse response, one could invert the response matrix and mathematically solve for the amplitude of the incident pulses (proportional to energy deposition of each incident gamma ray). In fact, this has been carried out in our study and gives reasonably good results. However, if direct approach is prohibitive, Maximum Likelihood Expectation

Maximization algorithm could be used to provide an estimation of the s_j vector using the well-known equation:

$$s_k^{(n+1)} = s_k^{(n)} \left\{ \frac{1}{\sum_{d=1}^D t_{dk}} \sum_{d=1}^D \left[\frac{y_d}{\sum_{b=1}^B t_{db} x_b^{(n)}} t_{dk} \right] \right\}.$$

The algorithm described above was first tested using simulated data. The impulse response function is assumed to be a double exponential function, simulating the anode signal from a PMT coupled with a scintillator detector. The rising edge time constant is determined by the PMT response (normally between 20 and 80 ns), while the falling edge has the decay constant of the scintillator (e.g. 230 ns for NaI). The amplitude and the time of arrival of each pulse are randomly generated. The simulated waveform is then the superposition of these individual pulses. In the de-convolution process, the shape (i.e. template) and the time of arrival of each pulse were assumed to be known. Using the algorithm discussed above, the amplitude of each pulse can be calculated. As shown in Figure 4.10, if the time of arrival and the template can be accurately determined, the de-convolution result is very good even when noise was added.

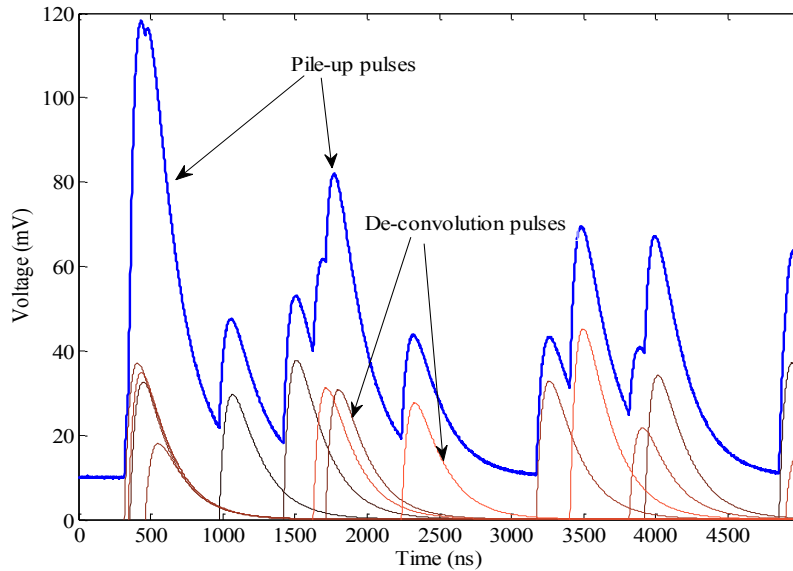


Figure 4.10 Application of the template-matching algorithm in simulated data.

4.2.1.2 Implementation on signals from a NaI detector

Firstly, the algorithm was implemented on signals obtained using a NaI detector. The detector used in these measurements was a Canberra Model 802 detector with a 2" by 2" crystal. The anode signal was directly digitized at a sampling rate of 100 MSPS using a National Instruments digitizer, model number PXIe-5122. A LabVIEW program was developed to enable streaming of digitized data onto a hard drive array at full speed for off-line processing. The digitized signal and the template are shown in Figure 4.11. Due to the large noise imposed on the anode signal,

matching result was not ideal. Also, the determination of the time of arrival was challenging. Because of the fast rising edge, an offset of one or two points could cause a large deviation between the template and the measured data. In this case, the signal measured at very low count rate was used as the template for deconvolution. The performance of the template-matching algorithm was compared with traditional shaping methods. The shaping parameters (i.e. rise time and flat top time) used in the measurement with the Canberra Lynx system were $1\ \mu\text{s}$ and $1\ \mu\text{s}$. At moderate count rate ($\sim 200\ \text{kcps}$), the results were comparable, as shown in Figure 4.12.

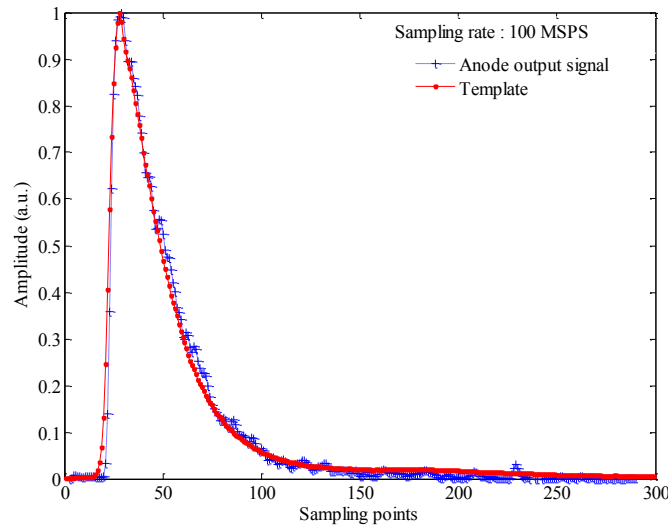


Figure 4.11 The anode output signal and template.

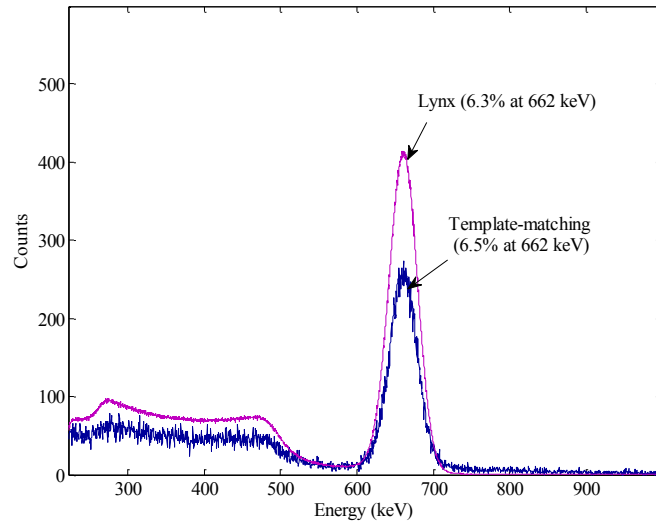


Figure 4.12 Comparison between energy spectra measured with the Canberra Lynx system and reconstructed with the template-matching algorithm.

4.2.1.3 Implementation on signals from a silicon drift detector

The performance of the algorithm was also tested on high rate data measured with a silicon drift detector, provided by Southern Innovation. During the measurements, a Mn foil was irradiated with photons generated from an Amptek Mini-X tube to produce characteristic x-rays with energy of 5.89 keV and 6.49 keV. The detector used was a Ketek 30 mm² silicon drift detector. Different input count rate (between 50 kcps and 500 kcps) was produced by tuning the tube current. The 50 kcps data was utilized to create a template by averaging over 200 pulses that did not suffer from pile-up. The energy resolution that the template-matching algorithm achieved at low input count rate (i.e. 50 kcps) was 131 eV at 5.89 keV. Good Gaussian peak shape and reasonable energy resolution could still be obtained even at very high input rate (e.g. 500 kcps), as shown in Figure 4.13. To compare the performance of the template-matching algorithm with traditional pulse processing using trapezoidal filters, we first adjusted shaping parameters to achieve comparable energy resolution and compared throughput rate at each input rate. As shown in Figure 4.14, a much higher throughput rate (e.g. 467 kcps vs 67 kcps at 500 kcps input rate) was achieved with the template-matching algorithm at very high input rate. The traditional pulse processing algorithm suffered huge decrease in throughput at high input rates due to pile-up rejection. The shaping parameters were then adjusted to achieve similar throughput rate using both algorithms at a certain input rate. Figure 4.15 shows the energy resolution as a function of input rate. As can be observed, using the template matching algorithm, resolution of less than 200 eV at 5.89 keV could be achieved even at 500 kcps. The resolution gradually degraded as input rate increased. This degradation is much more prominent for the traditional processing algorithm due to pile-up. In summary, Figures 4.13-15 clearly demonstrated the advantages of the template-match algorithm over traditional approaches: superior throughput with comparable energy resolution; superior energy resolution with comparable throughput.

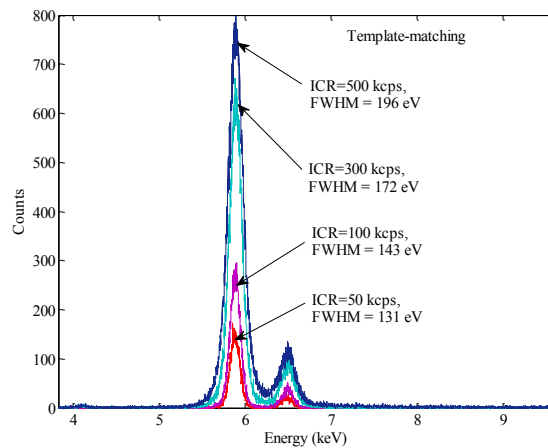


Figure 4.13 Energy spectra at different Input Count Rates (ICR) with the template-matching algorithm.

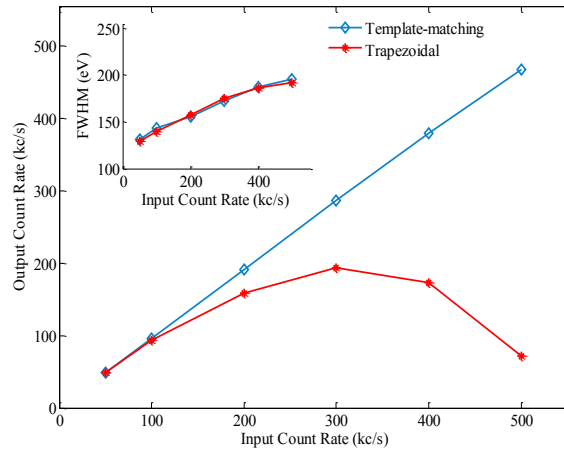


Figure 4.14 Comparison between the template-matching algorithm and the trapezoidal filter (Output Count Rate vs Input Count Rate).

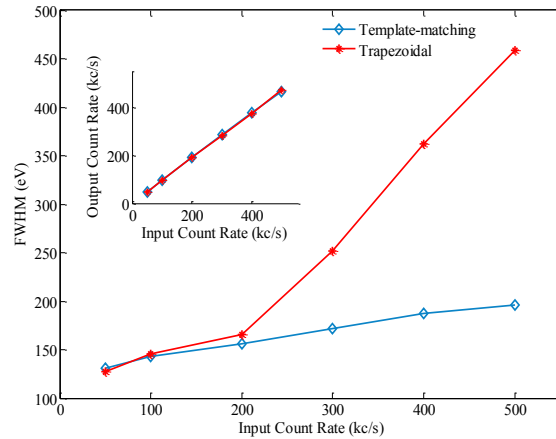


Figure 4.15 Comparison between the template-matching algorithm and the trapezoidal filter (FWHM vs Input Count Rate).

4.2.1.4 Implementation on signals from a HPGe detector

The HPGe detector is the only practical choice that can provide excellent energy resolution in a wide energy range as needed in measuring delayed gamma-ray spectra following active interrogation for nuclear safeguards applications. As discussed above, in such measurements, there are two issues that greatly limit the throughput of a HPGe detector: the long saturation after each linac pulse and the pulse pile-up due to high input rate. Our approaches to address this challenge include modification of the front-end electronics of a HPGe detector to allow fast return from saturation to baseline at high-energy input rate and the development of advanced digital signal processing techniques to improve the throughput rate with only small sacrifice in energy resolution. Here, we discuss the implementation of the template-matching algorithm on signals from a HPGe detector. It is quite challenging to implement the template-matching algorithm on HPGe signals because of the variation in pulse shape. To be specific, for a pulse from the pre-amplifier, the falling edge is determined by the RC constant of the pre-amplifier

(e.g. $\sim 50 \mu\text{s}$). On the other hand, the rising edge varies with the gamma-ray interaction position inside the detector. For simplicity, a generic template was used in current work. Pulses from the pre-amplifier were very well reconstructed at the falling edge, but a significant amount of deviation between the measured and reconstructed signals could be observed at the rising edge, as shown in Figure 4.16. In spite of this large deviation, good energy resolution at input rates up to 200 kcps was achieved, as shown in Figure 4.17. A performance comparison between the template-matching algorithm and the traditional trapezoidal shaping was again performed and summarized in Table 4.1. The results showed the advantage of the template-matching approach despite the fact that a good template is difficult to construct.

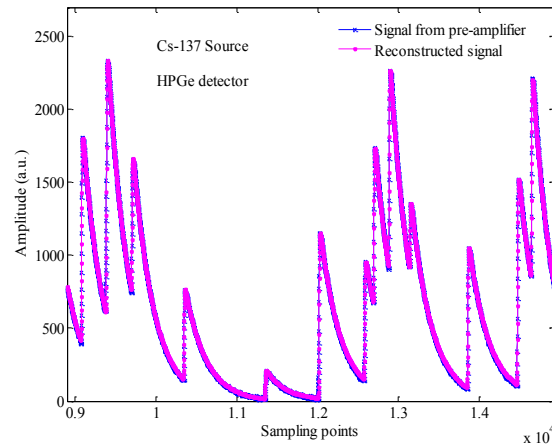


Figure 4.16 Verification of the reconstructed signal from preamplifier.

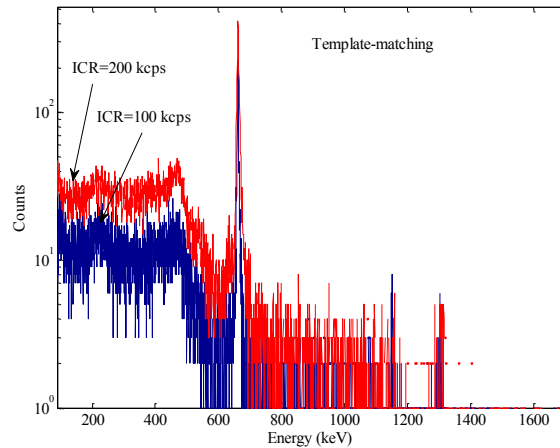


Figure 4.17 Energy spectra reconstructed with the template-matching algorithm.

Table 4.1 Comparison between the template-matching algorithm and the trapezoidal filter (HPGe data).

	Input Count	Output Count Rate	FWHM (keV)
--	-------------	-------------------	------------

	Rate (kc/s)	(kc/s)	at 662 keV
Trapezoidal	100	79.8	2.7
	200	141.0	3.9
Template-matching	100	96.6	2.8
	200	186.8	4.6

4.2.1.5 Conclusions

To perform high-resolution spectroscopy measurements at an ultra-high throughput rate is a major challenge in active interrogation techniques for nuclear safeguards application. In this work, the development of advanced digital signal processing technique based on template-matching has been shown as an effective approach to address this issue. The principle behind the algorithm was described in detail. This algorithm was first tested using simulated piled-up pulses from a PMT coupled with a scintillator detector. Using a NaI detector, at moderate count rate (~ 200 kcps), energy resolution comparable to traditional trapezoidal shaping was achieved (6.5 % at 662 keV). With high rate data acquired with a silicon drift detector, the advantages of this new algorithm were demonstrated through comparison with the traditional approach using trapezoidal filters. Superior performance in terms of throughput rate and energy resolution was observed at high input rates. The performance of the template-match algorithm was then evaluated using signals from a HPGe detector. Despite the difficulty to construct an ideal template for pre-amplifier pulses, energy resolution of 4.6 keV at 662 keV and live time of 93.4% were successfully achieved at input rate of 200 kcps.

4.2.2 De-randomization technique

4.2.2.1 Deconvolution of pulses from HPGe preamplifier

The technique for deconvolution of pulses from an HPGe preamplifier was used to obtain the current signals [34]. A detailed description of the deconvolution method is given below. In common spectroscopy systems, the detector-preamplifier configuration is followed by a pole-zeros cancellation and differentiation circuits. As a result, a pulse with short rise time and exponential tail is produced. The pulse is then amplified to increase signal-to-noise ratio. A block diagram of a typical RC feedback preamplifier is shown in Figure 4.18. A schematic drawing of the preamplifier is given in Figure 4.19(a). The configuration can also be present as an ideal current-voltage converter followed by a RC low-pass network, as shown in Figure 4.19(b). The voltage signal at the output of the current-voltage converter has the same shape as the detector current signal. Therefore, the current signal can be obtained by finding the inverse transfer function of the RC network. In other words, the purpose of the deconvolution is to cancel the effect of the convolution of the current signal with the impulse response of the RC network. In

this case, it is obvious that the impulse response of the RC network and deconvolver should be a delta function. To simplify the derivation of the deconvolution equation the detector current signal is assumed to be a delta function and the amplifiers A1 and A2 are considered ideal elements which do not affect the pulse shape.

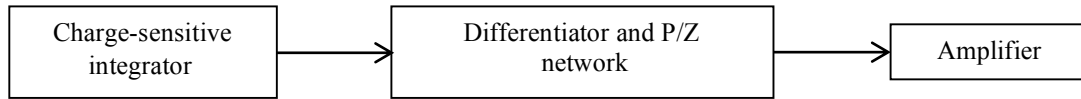
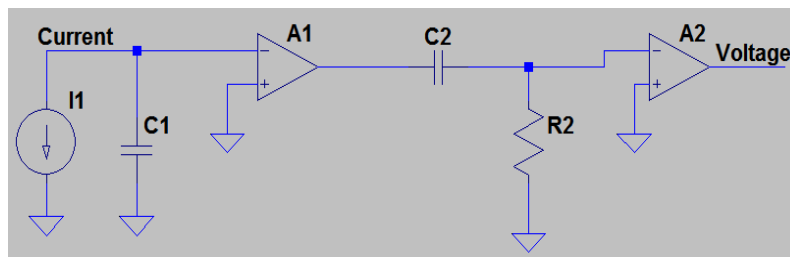
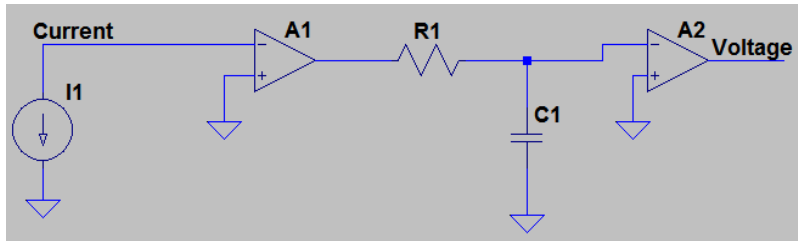


Figure 4.18 A block diagram of the functionality of a typical RC-feedback commercial preamplifier unit.



(a)



(b)

Figure 4.19 (a) A schematic drawing of a preamplifier with RC-feedback, (b) An equivalent presentation of the preamplifier.

The impulse response for the capacitor voltage in a RC low-pass network can be found by solving the following differential equation.

$$h_c(t) + \tau \frac{dh_c(t)}{dt} = \delta(t), t \geq 0 \quad (1)$$

The initial condition is $h_c(0) = 0$. Solving the above equation gives $h_c(t) = \frac{1}{\tau} e^{-\frac{t}{\tau}} u(t)$, where $\tau = RC$ is the time constant of the RC network, $u(t)$ is the step function. Similarly, the impulse response for the resistor voltage is $h_R(t) = \delta(t) - \frac{1}{\tau} e^{-\frac{t}{\tau}} u(t)$.

The impulse response for the capacitor voltage must satisfy the above equation. Therefore, the relationship between the input and output signals of the desired deconvolver should be expressed as follows:

$$v_{in}(t) + \tau \frac{dv_{in}(t)}{dt} = v_{out}(t) \quad (2)$$

The above equation written in discrete time domain is

$$v_{out}(k) = v_{in}(k) + (v_{in}(k) - v_{in}(k-1)) \times M \quad (3)$$

where k is the sampling point, M is a measure of the decay time constant τ of the preamplifier signal in the unit of sampling period τ_c that is given as $M = \left(e^{\frac{\tau_c}{\tau}} - 1 \right)^{-1}$. The deconvolution

algorithm can be easily implemented in a digital circuit. The digitized data from a preamplifier is delayed by one clock cycle and stored in a register. The delayed data is then subtracted from the prompt data. The subtract result is multiplied by the equivalent of the decay time constant, M . Finally, the result of the multiplication is added to the prompt data.

The algorithm was applied to digitized data obtained from an HPGe preamplifier. The exponential signal and deconvolution result are shown in Figure 4.20. Two major observations can be made from this Figure. First, the signal-to-noise ratio is significantly decreased after the deconvolution because the restoration of the current signal will inevitably cause restoration of noise. Second, the deconvolved signal does not exactly match the original current signal due to imperfections of the amplifiers (i.e. A1 and A2). In this case, the deconvolved pulse is a result of the convolution of the current signal with the impulse response of the system which accounts for the imperfections.

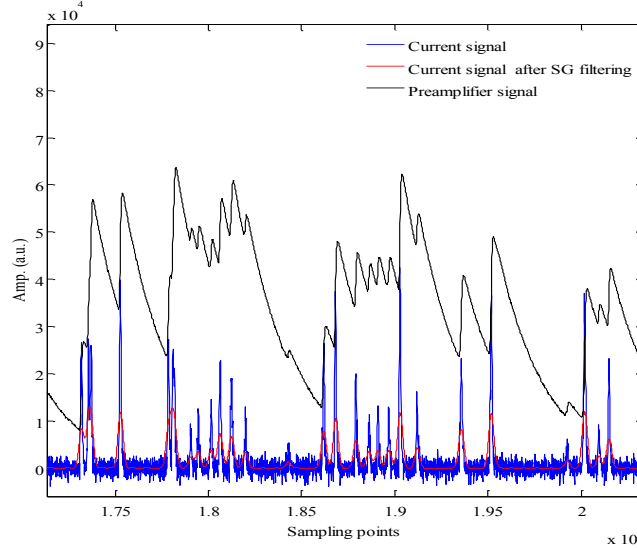


Figure 4.20 The deconvolution of pulses from an HPGe preamplifier.

4.2.2.2 Digital synthesis of exponential signals

Exponential signals in discrete time domain are defined as follows [35]:

$$y(n) = \begin{cases} a^n, & n \geq 0 \\ 0, & \text{otherwise} \end{cases} \quad (4)$$

Where a is a constant, n is sampling point. All samples $y(n)$ have constant values if a is equal to 0 or 1. $y(n)$ is a decaying exponential signal if a is greater than 0 but less than 1. If a is greater than 1, $y(n)$ is a growing exponential signal. If a is less than 0, $y(n)$ alternates between positive and negative numbers. For the signal from an HPGe preamplifier, a is greater than 0 but less than 1.

From the equation (4), the ratio of two consecutive values of an exponential signal can be expressed as follows:

$$\frac{y(n+1)}{y(n)} = \frac{a^{n+1}}{a^n} = a, n \geq 0 \quad (5)$$

Using the equation (5), a recursive form for an exponential signal can be expressed as

$$y(n+1) = y(n) \times a \quad (6)$$

The initial condition for the equation (6) is

$$y(n) = 1 \text{ and } y(n) = 0 \text{ for } n < 0.$$

The purpose of the exponential signal synthesis is to find a linear time-invariant recursive system which generates an exponential signal in response to an input signal $x(n)$. The recursive form for the system can be present as

$$y(n+1) = y(n) \times a + x(n) \quad (7)$$

From the equation (7), the impulse response of the recursive system is

$$h(n) = h(n-1) \times a + \delta(n), n \geq 0 \quad (8)$$

It is obvious from the equation (8) that the impulse response is an exponential signal, which grows or decays in time depending on the constant a . Figure 4.21 shows the synthesized exponential pulses from the detector current signals using the equation (7).

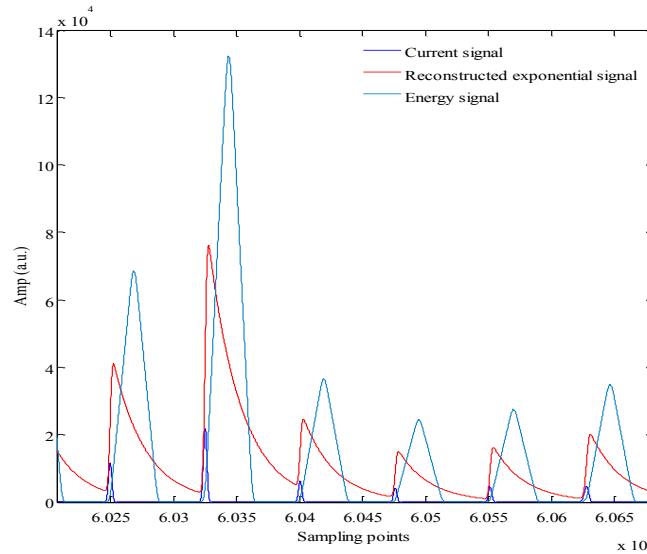


Figure 4.21 Digital synthesis of exponential pulses from the detector current signals.

The recursive algorithm can be easily implemented in digital circuit. It only requires three functional blocks: a delay/register, a multiplier and an adder. The output signal is delayed by one clock unit and then multiplied by the constant a . The multiplication result is then added to the input signal to produce next output signal. The recursive system will produce exponential signals that are either growing or decaying depending on the constant a in response to a unit impulse $\delta(n)$. The growth and decay rates are determined by the magnitude of the multiplication coefficient which is the exponential base of the produced exponential signal. Because the detector current signal is not a delta function, the output signals from the recursive system have a short rise time, as shown in Figure 4.21.

4.2.2.3 The effect of the deconvolution and synthesis on energy resolution

It was observed that only small discrepancy exist between the reconstructed exponential pulses and the preamplifier signals. To study the possible impact of the deconvolution and synthesis on energy resolution, the reconstructed pulses were shaped to obtain the energy information using the traditional trapezoidal filtering approach. In the trapezoidal filtering, there were two channels shaped in parallel, i.e. energy and time channels. The energy signal was shaped with a long shaping time to perform energy measurement. The time signal shaped with shorter shaping time was used to detect the time-of-arrival of each event and perform pile-up rejection. If a pulse arrives within $2*L+K$ (L : rise time, K : flat top time) after the previous pulse, both pulse will be

rejected to have an energy spectrum with good energy resolution. To reduce the impact of ballistic deficit on energy resolution, the flat top of the trapezoidal filter needs to be longer than the charge collection time. To find the appropriate flat top time empirically, the charge collection time for each event was first estimated using the recursive algorithm for digital pulse shaping (V. Jordanov).

The above deconvolution method could also be used to make an estimation of the charge collection time. Due to large noise was restored in the deconvolution, a large threshold was required to avoid possible false trigger. Compared to the pulse shaping method to find the charge collection time, the deconvolution method is easy to implement in digital circuit and the resource utilization is small. The disadvantage is that pulses with amplitude comparable to noise level may not be triggered. The small pulses were then not used to find the collection time. After obtaining the information about the charge collection time, various rise times in the slow channel for energy measurement were used to find the optimal rise time. Once the optimal shaping time was obtained, the traditional trapezoidal filtering method was used to obtain energy spectra and then compare the energy resolution achieved from the original and reconstructed pulses. In the energy spectrum reconstruction, the same pile-up rejection method was applied. It was observed that there was almost not degradation in energy resolution because of the deconvolution to find the detector current signals and the synthesis of exponential pulses.

4.2.2.4 The impact of the background noise on energy resolution

In the energy spectrum reconstruction from the synthesized exponential pulses, no data was added to the detector current and noise signal so far, which will be necessary in the de-randomization process to make sure the time interval between two successive current signals be equal or large than the $2*L+K$ (L is the rise time, K is the flat top time) [36]. It was found that the assumption that the noise restored from the deconvolution is not correlated is not correct. When the background noise was used to de-randomize the current signals, very large degradation in energy resolution was observed. This resolution will be worse at higher input count rate. To overcome this challenge the Savitzky-Golay (SG) filter was first used to process the deconvolved current signal. As shown in the Figure 7, the signal-to-noise was significantly improved and the peak location remains after the SG filtering. One disadvantage is that the pulse time domain increases because the SG filtering doesn't change the peak area but reduces the peak amplitude. However, the time is still much smaller compared to normal shaping time used in the traditional trapezoidal filtering (i.e. a few hundred nanoseconds vs ~ten microseconds). This means the pile-up is only limited by the charge collection time. In this case, the throughput rate could be greatly improved, especially at ultra-high count rate.

4.2.2.5 Implementation of the algorithm on high-rate HPGe data

The major steps used in the new algorithm are described here in detail. First, the deconvolution method (Equation 3) is used to obtain the detector current signals from the preamplifier pulses. Because the restoration of the current signal will inevitably cause restoration

of noise and it was found that the way to de-randomize the current signal by adding the background noise will significantly affect energy resolution, the SG filter is used to smooth the deconvolved signals before de-randomization. The SG filtering can be easily implemented in Matlab using the function `sgolayfilt(x,k,f)`, where k is the polynomial order, f is the frame size. In this work, the parameters k and f in the function `sgolayfilt(x,k,f)` were set at 1 and 9, respectively. The effect of the parameters on energy resolution will be further studied. The next step is the de-randomization process that is the key to greatly improve throughput rate using the new algorithm.

The basic idea of the de-randomization is that the time interval between the two successive current signals must be equal or large than the $2*L+K$ after the de-randomization, where K and L are the shaping parameters in the traditional trapezoidal filtering [36]. The current signals after the de-randomization are then used to synthesize exponential pulses using the recursive Equation (7). The last step is to obtain the energy information of each pulse from the exponential signals using the traditional trapezoidal filtering method. The rise time and flat top time in the trapezoidal filtering were set at $9\ \mu\text{s}$ and $0.8\ \mu\text{s}$, respectively. The impact of the shaping parameters on energy resolution will be investigated in future. No pile-up rejection or recovery techniques were used in the filtering. Pile-up correction will be a major focus of future work. Potential solution will include statistical signal processing techniques.

Figures 4.22 and 4.23 show the reconstructed energy spectra from HPGe data using the new digital pulse processing algorithm. The energy resolution is about 2.5 keV at 662 keV at input count rate of 100 kcps. The output count rate is also 100 kcps because no pulse was rejected. The result means that throughput rate can be significantly improved without sacrifice in energy resolution. The algorithm was also applied to a high rate HPGe data (i.e. 300 kcps). Only slight degradation in energy resolution was observed (i.e. 3.1 keV vs 2.5 keV @ 662 keV). However, pile-up events can also be seen from the Figure 9. The pile-up phenomenon occurs only when gamma interacts with the detector within the charge collection process of previous event. Statistical signal processing techniques to recover the pile-up events will be investigated. Also, the new pulse processing algorithm will be applied to much higher count rate HPGe data (e.g. 1×10^3 kcps). The energy resolution and throughput rate will be studied and compared with results obtained using the Kalman filtering approach and the time-variant trapezoidal filtering method at such high count rate.

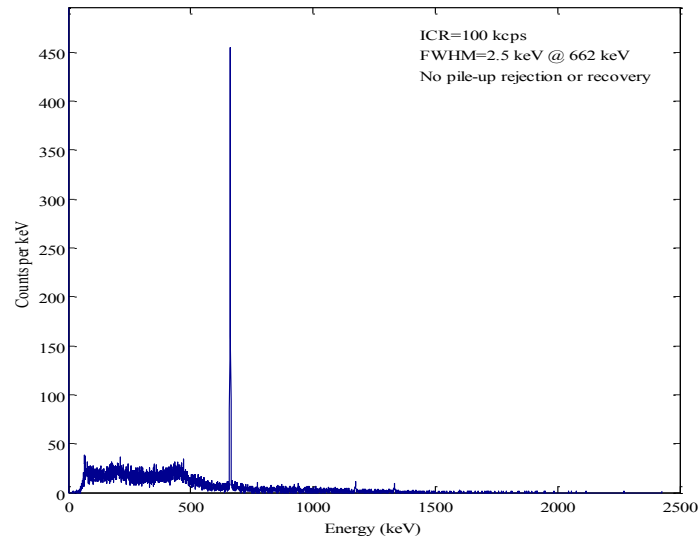


Figure 4.22 Energy spectrum reconstructed using the algorithm based on the de-randomization method (ICR=100 kcps).

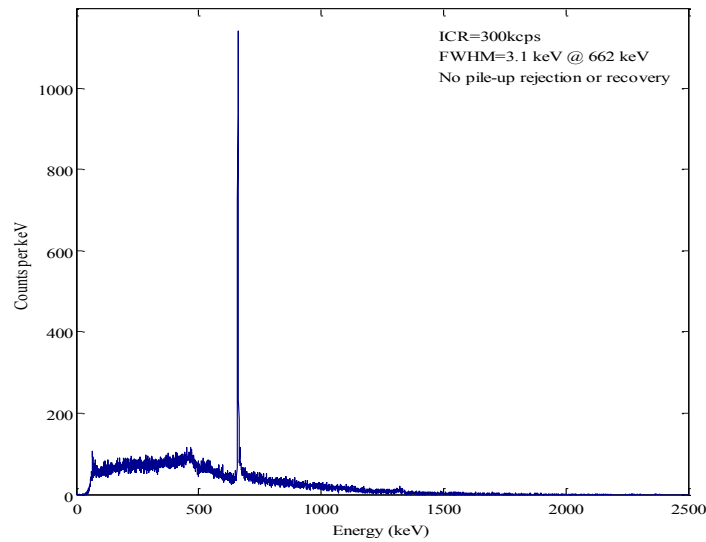


Figure 4.23 Energy spectrum reconstructed using the de-randomization method (ICR=300 kcps).

4.2.3 Kalman filtering

Development of advanced pulse processing algorithms is described in detail below. First, an introduction to Savitzky-Golay and Kalman filters is given. This is followed by the study on the state space model for preamplifier signal. Finally, energy spectra reconstructed using the Kalman filter were achieved without significant degradation in energy resolution.

4.2.3.1 Savitzky-Golay and Kalman filters

Savitzky-Golay filter is a digital filter used to increase signal-to-noise ratio without significantly distorting signal. This is achieved by fitting adjacent data points with a low-degree

polynomial using the method of linear least squares. When the data points are equally sampled, such as digitized data from an ADC converter, an analytical solution to the least-squares equations can be derived. A summary of the properties of the Savitzky-Golay filter is described below [37].

1. The odd-indexed coefficients of the impulse response function of this filter are all zero.
2. Moving average filter is a special case of Savitzky-Golay filter. They are the same when the order of polynomials in the Savitzky-Golay filter is zero and the length of approximation interval is equal to one. In the case of moving average filtering, although it can greatly reduce noise, useful signal is significantly smoothed out at the same time. In particular, signal cannot be preserved when the filter passes through peaks that are narrow compared to the filter width.
3. The impulse response function is symmetric since there are only even-indexed coefficients in the response function. As a result, the frequency response function is real.
4. The zeros of the system function are either on the unit circle of the z-plane or exist in complex conjugate reciprocal pairs. The zeros on the unit circle are responsible for the high attenuation in the stopband.
5. Frequency response in the passband is very flat.
6. Both the polynomial order and length of the impulse response function affect the nominal cut-off frequency (i.e. 3 dB).
7. The area under a peak remains after Savitzky-Golay smoothing. This property is heavily used in the development of advanced pulse processing algorithms.
8. The signal distortion and signal-to-noise improvement decrease as the polynomial order increases. Both of them increase as the length of the impulse response function increases. The optimal choice of polynomial order and the length of the impulse response function will be a compromise between signal distortion and noise reduction.
9. Savitzky-Golay filter can easily be implemented in Matlab using the function called `sgolayfilt(x,k,f)`. The parameter `k` is the polynomial order and must be less than the frame size `f`. The filter doesn't smooth data when `k` is equal to `f-1`. When `x` is a matrix, the function `sgolayfilt(x,k,f)` operates on each column of the matrix.

As an example of demonstrating these properties, Figure 4.24 shows the signal-to-noise ratio of a noisy current signal could be significantly improved after passing through the Savitzky-Golay filter.

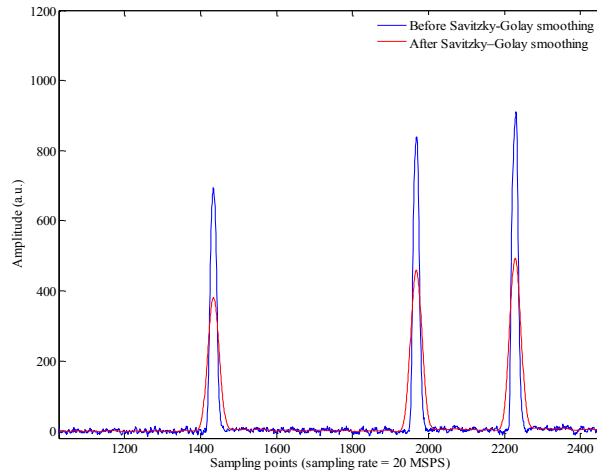


Figure 4.24 Comparison of a noisy current signal before and after Savitzky–Golay smoothing.

Kalman filter is a set of recursive equations that can be used to efficiently estimate the state of a process, in a way that achieves a minimum mean square error (MMSE). That means it is a MMSE estimator. This is true only when the state space model is linear and the noise in the model is Gaussian. In spite of the limit, Kalman filter has been found in numerous applications. A common application is in navigation for aircraft and spacecraft. Furthermore, Kalman filter is widely used in time series analysis, such as digital signal processing. It is also one of the main topics in robotics. Extensions to the normal Kalman filter have also been developed, such as the extended Kalman filter that works for a nonlinear model. In the extended Kalman filtering, the estimation is linearized around the current estimate using the partial derivatives of the process and measurement functions. The Jacobian matrix, similar to the Kalman gain in the Kalman filter, is evaluated with current predicted states.

The Kalman filter addresses the general problem of trying to estimate the state x of a discrete-time controlled process. The process is governed by the linear stochastic difference equation as shown below.

$$x_k = A_k x_{k-1} + B_k u_k + w_k$$

Where x_k is the state at time k and represented by a vector of real numbers. Usually, the state cannot be directly observed. A_k is the state transition matrix; B_k is the control matrix; w_k is the process noise which is assumed to have a Gaussian distribution with zero mean and covariance Q_k , $w_k \sim N(0, Q_k)$;

A measurement z of the state x at time k is made according to the equation below.

$$z_k = H_k x_k + v_k$$

Where H_k is the observation matrix which maps the state space into the observed space; v_k is the measurement noise which is assumed to be a white noise with covariance R_k , $v_k \sim N(0, R_k)$. The

Kalman filter is based on linear dynamic systems in discrete time domain. They are modeled on a Markov chain. There are two steps in the Kalman filtering, prediction and correction. In the prediction step, the Kalman filter predicts priori estimate for the next time step from current state variables along with their error covariance. When a new measurement is available, this estimate is updated to obtain an improved posteriori estimate. The update is performed using a weighted average. More weight is given to a priori estimate with higher certainty. Because of the recursive property of this filter, only the present measurement, previous state estimate and its uncertainty matrix are necessary to obtain the posteriori estimate for the next state variables. No history of observations or estimates is required, which can greatly reduce source utilization in hardware and/or software. A schematic view of Kalman filtering is shown in Figure 4.25. The time update predicts the next state using the current state estimate, while the measurement update corrects the estimate using the new available measurement at that time.

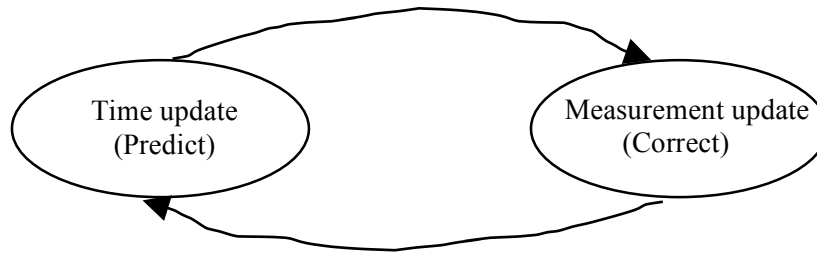


Figure 4.25 Illustration of the Kalman filtering (prediction and correction)

The popular equations for the time and measurement updates are shown below in details.

1. Predict

A prior state estimate $x_{k|k-1} = A_k x_{k-1|k-1} + B_k u_k$

A prior error covariance estimate $P_{k|k-1} = A_k P_{k-1|k-1} A_k^T + Q_k$

2. Correct

Kalman gain $K_k = P_{k|k-1} H_k^T (H_k P_{k|k-1} H_k^T + R_k)^{-1}$

A posterior state estimate $x_{k|k} = x_{k|k-1} + K_k (z_k - H_k x_{k|k-1})$

A posterior error covariance estimate $P_{k|k} = (I - K_k H_k) P_{k|k-1}$

As shown in the equations for time update, only the current state and covariance estimates are necessary to produce a prior estimate for the next state. A_k and B_k are the matrixes in the process equation at time k , Q_k is the covariance of the process noise. During the measurement update, the first step is to compute the Kalman gain at time k , K_k . Then a posteriori state estimate is generated by incorporating the latest measurement data. The final step is to obtain a posteriori error covariance estimate. This process is repeated when each time and measurement update is complete. This recursive property makes the Kalman filter more appealing compared with the Wiener filter, which is designed to obtain an estimate directly from all of the data instead of the current measurement.

4.2.3.2 State space model for preamplifier signal

The state space model used in the ADONIS system was studied this quarter for development of high-resolution high-throughput gamma spectroscopy [26, 28]. The highlight in the model is the introduction of a hidden semi-Markov variable r_k . The variable is equal to one during charge collection in a detector and zero otherwise. This is the key concept in the ADONIS system. All quantities, such as dead time, throughput rate and pile-up recovery, depends on an accurate estimation of this variable. Another important concept is the representation of preamplifier output by a state space model whose parameters rely on the indicator variable. This representation is a special case of jump linear Markov systems. The preamplifier output is first used to obtain noisy current signal denoted by y_k . This can be achieved by performing convolution of the measured signal and the preamplifier impulse response function. The current signal corrupted with noise is then the observation in the state space model. The noise is assumed to be blue with power spectral density $N(\omega) \propto \left(1 + \left(\omega/\omega_c\right)^2\right)$. The blue noise n_k can be treated as a white noise w_k^n with variance Q_n after passing through a digital filter with system function $H(z) = 1 - \alpha z^{-1}$, where α can be expressed as $e^{-T\omega_c}$, T is the sampling rate. A baseline noise b_k is also considered in the state space model to account for potential baseline shift. It is modelled as the integral of a white noise w_k^b with variance Q_b . The ideal detector current is represented by a state p_k , which should be zero without charge migration in a detector and any positive value otherwise. The ideal current can be modelled as a white noise w_k^p with variance Q_p when the indicator variable is equal to one. The variance Q_p is usually fixed at a large value. From the above descriptions, the jump linear Markov system can be summarized as follows:

$$\begin{cases} p_{k+1} = r_k w_k^p \\ b_{k+1} = b_k + w_k^b \\ n_{k+1} = -\alpha w_{k-1}^n + w_k^n \\ y_k = p_k + b_k + n_k \end{cases}$$

With the introduction of state vector $X_k = (p_k \ b_k \ n_k \ v_k)^T$ and $W_k = (w_k^p \ w_k^b \ w_k^n)^T$, where v_k is equal to w_{k-1}^n , the above jump linear Markov system can be described as a state space model as follows:

$$\begin{cases} X_{k+1} = F \cdot X_k + B \cdot W_k \\ y_k = H \cdot X_k \end{cases}$$

Where

$$F = \begin{pmatrix} 0 & 0 & 0 & 0 \\ 0 & 1 & 0 & 0 \\ 0 & 0 & 0 & -\alpha \\ 0 & 0 & 0 & 0 \end{pmatrix}, B = \begin{pmatrix} r_k & 0 & 0 \\ 0 & 1 & 0 \\ 0 & 0 & 1 \\ 0 & 0 & 1 \end{pmatrix}, H = (1 \quad 1 \quad 1 \quad 0).$$

4.2.3.3 Energy spectra reconstructed using the Kalman filtering method

The solution to the state space model can be optimally obtained with the knowledge of the indicator variable r_k . In reality, r_k needs also to be estimated. A way to reduce computation complexity is to use iterative method. The first step is to solve X_k by assuming that r_k is known. X_k can be optimally estimated using the Kalman filter. After an estimation of X_k is available, it will be used to update the variable r_k . The iteration process will be repeated until X_k and r_k are converged. This process can be greatly simplified when the signal-to-noise ratio is large enough. For example, single iteration is enough to differentiate the two states of variable r_k when gamma ray energy is greater than several standard deviations of noise. In our work, the Savitzky-Golay filter was first used to smooth the noisy current signal. The polynomial order and frame size in the function `sgolayfilt(x,k,f)` were set at 1 and 9, respectively. It was found that this step was useful to obtain a better estimation of the variable r_k . As shown in Figure 4.26 the indicator signal is zero in the absence of charge migration in a detector and non-zero otherwise. After X_k and r_k were predicted from the Kalman filtering, the Bryson-Frasier smoothing algorithm was used to provide a better estimation of X_k . It is a fix-interval backward smoothing by taking into account future samples. The smoothing was only applied on each slice of N samples rather than the whole data points. The noisy current signal after passing through filtering and smoothing is shown in Figure 4.27. The energy spectra reconstructed using the Kalman filtering and backward smoothing methods are shown in Figures 4.28 and 4.29. The HPGe data was provided by Canberra Industries. The input count rate was kept at ~ 100 kcps by adjusting the distance between the source and the detector. As shown in Figure 9, energy spectrum with good energy resolution (4.8 keV@ 662 Kev) and Gaussian shape peak was achieved without pile-up rejection or recovery. A reasonable energy resolution (5.9 keV @ 662 KeV) was accomplished without performing pile-up correction at input count rate of 300 kcps. However, as shown in Figure 4.29, a double peak due to pile-up is observed. Statistical signal processing techniques for pile-up recovery will be a major research area in our future work.

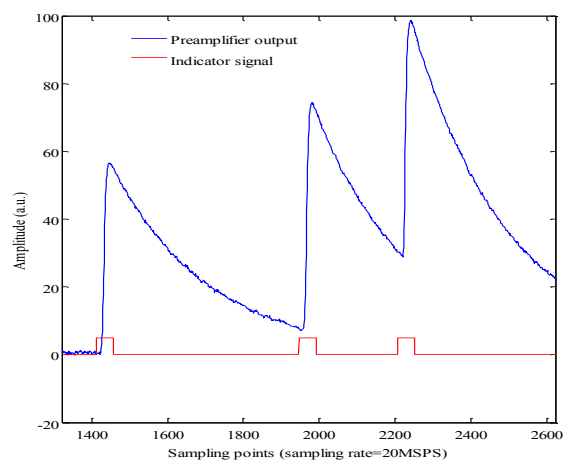


Figure 4.26 Preamplifier output and indicator signal (The indicator signal in the figure was scaled up by 5.)

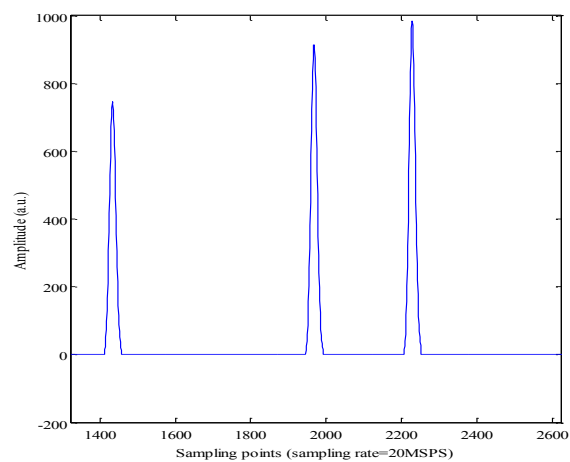


Figure 4.27 Noisy current signal after the filtering and smoothing.

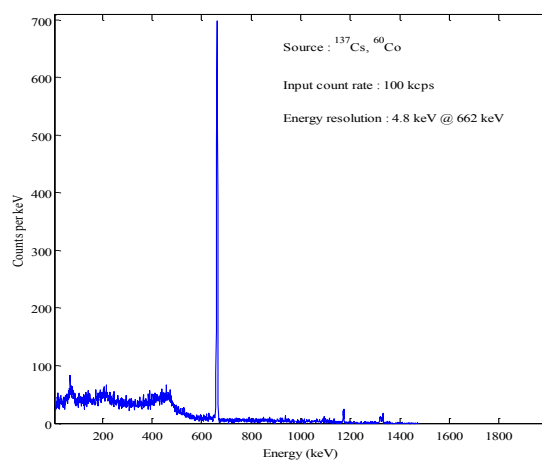


Figure 4.28 Energy spectrum reconstructed using the advanced digital pulse processing algorithm (ICR =100 kcps).

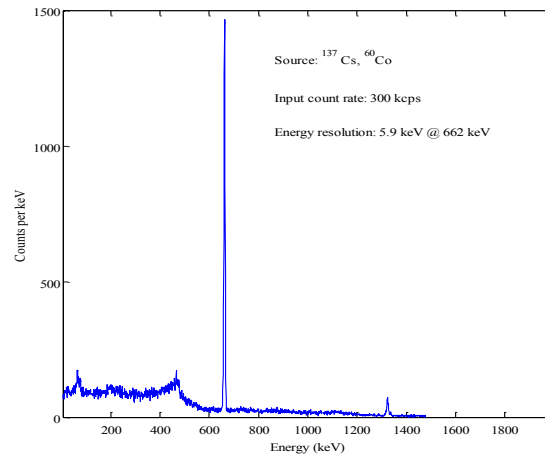


Figure 4.29 Energy spectrum reconstructed using the advanced digital pulse processing algorithm (ICR = 300 keps).

4.2.4 Time-variant trapezoidal filtering

In the traditional trapezoidal filtering, especially at high count rate, pile-up phenomenon is a major challenge in high-resolution high-throughput spectroscopy measurement. To obtain good energy resolution piled-up events are rejected at the expense of detection efficiency. It is highly desired to achieve high throughput rate while maintaining good energy resolution. The concept of time-variant trapezoidal filtering was tested to improve throughput rate without large sacrifice in energy resolution. The basic idea of the filtering approach is that several trapezoidal filters with different shaping times are implemented in parallel and the one with largest shaping time which can resolve pile-up events is used to perform energy measurement of corresponding pulses, as shown in Figure 4.30. The first step is to find the energy resolution at various shaping times. The flat top time was kept at 0.8 μs . As shown in Table 4.2, the best energy resolution achieved from the 100 keps HPGe data is 2.3 keV at 662 keV. The optimal rise time is 9 μs for the 100 keps data. Table 4.3 shows the energy resolution for the 300 keps data at different rise times. The best energy resolution was about 3.0 keV at 662 keV. The optimal rise time for the 300 keps data is smaller than that for the 100 keps data (i.e. 6 μs vs 9 μs). Tables 4.2 and 4.3 give the longest shaping time used in the time-variant trapezoidal filtering (i.e. 9 μs for the 100 keps data, 6 μs for the 300 keps data). As an illustration of time-variant trapezoidal filtering, Figure 1 shows the energy signals shaped from signals from an HPGe preamplifier using different rise times (i.e. 1-, 3-, 5 μs).

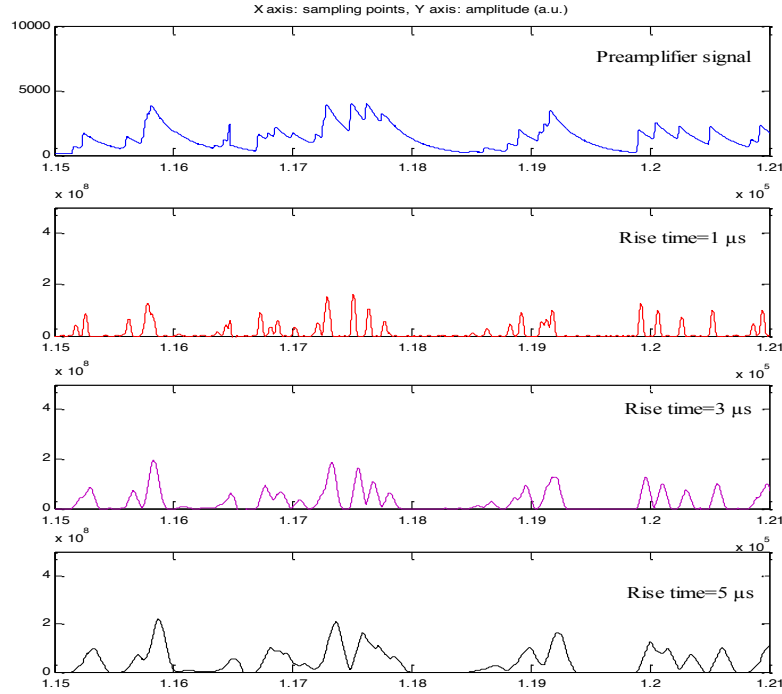


Figure 4.30 Trapezoidal filtering using different rise times (ICR=300 kcps).

Table 4.2 Energy resolution vs rise time (Input count rate =100 kcps).

Rise time (μs)	FWHM (keV)	Rise time (μs)	FWHM (keV)
1	5.6	7	2.5
2	4.5	8	2.4
3	3.7	9	2.3
4	3.3	10	2.7
5	3.1	11	2.9
6	2.7		

Table 4.3 Energy resolution vs rise time (Input count rate =300 kcps)

Rise time (μs)	FWHM (keV)	Rise time (μs)	FWHM (keV)
1	7.2	5	3.6
2	5.3	6	3.0
3	4.3	7	3.7
4	3.9		

Figures 4.31 and 4.32 show the energy spectra reconstructed from the 100 kcps and 300 kcps data using the time-variant trapezoidal filtering method. Table 4.4 shows the comparison between the results obtained using the traditional trapezoidal filtering and time-variant trapezoidal filtering methods. As shown in Table 4.4, the throughput rate was significantly improved without large sacrifice in energy resolution, especially at higher input count rate. For

example, the output count rate was increased from 87 kcps to 216 kcps using the time-variant trapezoidal filtering approach at input rate of 300 kcps. However, only slight degradation in energy resolution was observed (i.e. 4.2 keV vs 3.0 keV @ 662 keV). The benefit from the time-variant trapezoidal filtering method will be studied at much higher count rate (e.g. 1×10^3 kcps).

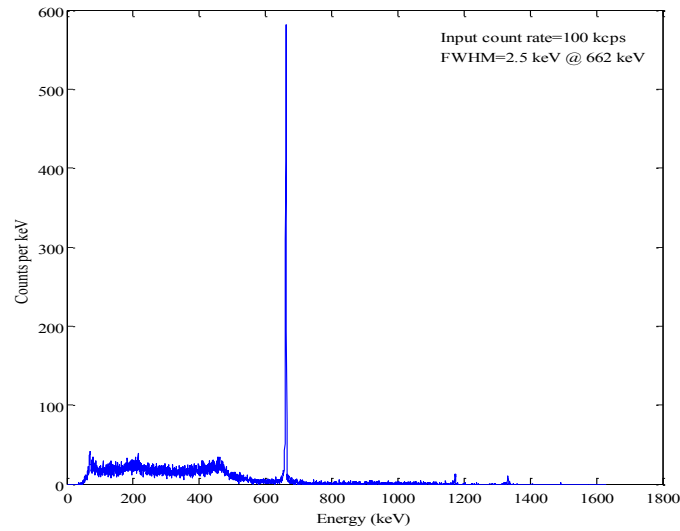


Figure 4.31 Energy spectrum reconstructed using the time-variant trapezoidal filtering method (ICR=100 kcps).

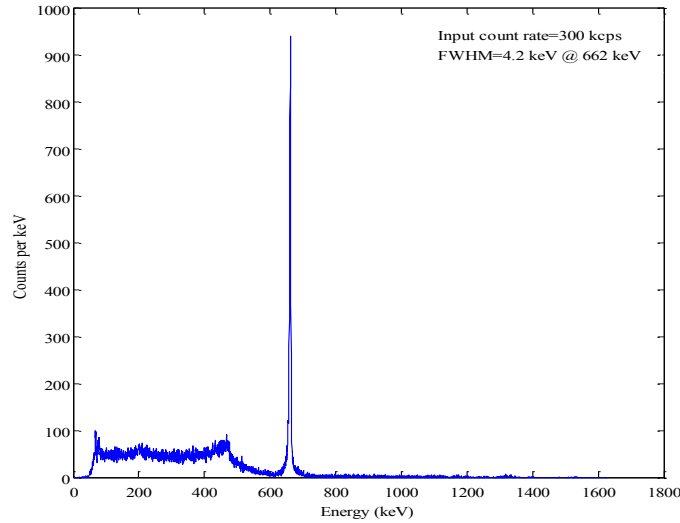


Figure 4.32 Energy spectrum reconstructed using the time-variant trapezoidal filtering method (ICR=300 kcps).

Table 4.4 Comparison between the traditional trapezoidal filtering and time-variant trapezoidal filtering.

	Input Count Rate (kcsp)	Output Count Rate (kcps)	FWHM (keV) at 662 keV
Traditional trapezoidal filtering	100	59	2.3
	300	87	3.0
Time-variant trapezoidal filtering	100	86	2.5
	300	216	4.2

5 Digital gamma spectroscopy system development on FPGAs

Off-line processing is not practical with high sampling rate and long data acquisition time. Storing all raw data acquired with digitizers of high sampling rate (e.g. ~ 50 MSPS) causes a storage overload problem in the case where the duration of an experiment lasts hours or even more. Real-time digital signal processing (DSP) techniques are much more attractive as the amount of information to be stored could be greatly reduced. Modern FPGAs possess high computational power and large amount of hardware resource including dedicated DSP modules. They offer a wide variety of possibilities for real-time DSP. The traditional trapezoidal filter was used in the development since it is a recursive algorithm and easy to implement. Two FPGA platforms were available for designing customized gamma spectroscopy systems. The first one included a National Instruments PXIe-7966R module and an adapter module 5761. The second platform consisted of a Xilinx ML605 Evaluation Kit and a 4DPS's FMC 151. More details about the platforms are described below.

5.1 National Instruments PXIe-7966R

5.1.1 Hardware description

With the introduction of the LabVIEW FPGA Module, LabVIEW graphical language can be used to program FPGAs from National Instruments. A PXIe-7966R FPPA module and an adapter module 5761 were purchased from this vendor. A picture of the hardware is shown in Figure 5.1. The PXIe-7966R is mainly designed for implementing digital filters, fast Fourier transform and custom signal processing. It has a faster speed grade of -2 when comparing to the PXIe-7965R, which is necessary to be compatible with high performance adapter modules. Peer-to-peer streaming technology is also included in this module to enable data transfer among multiple FPGA modules without sending data back and forth between PC and FPGA modules. The NI 5761 is a high-performance digitizer designed to digitize analog signal and send data to FPGA modules. Combination of the NI 5761 and PXIe-7966R provides an alternative to conventional analogical gamma spectroscopy. The major parameters of the PXIe-7966R and adaptor module 5761 are shown in Tables 5.1 and 5.2, respectively.



Figure 5.1 Hardware for the development of customized digital gamma spectroscopy system.

Table 5.1 The parameters of the NI FPGA module PXIe-7966R.

Item	Value	Item	Value
Model	NI PXIe-7966R	Number of DMA Channels	16
FPGA	Virtex-5 SX95T	Default timebase	40MHz
FPGA slices	14,720	Timebase Accuracy	± 50 ppm, 250 ps
FPGA DSP slices	640	Number of banks	2
FPGA memory	8,784 kbit	Maximum data rate	1.6 GB/s per bank
Onboard memory	512 MB	Data Transfers	DMA, programmed I/O

Table 5.2 The parameters of the NI adapter module 5761.

Item	Value	Item	Value
Number of channels	4	Digital data range	$\pm 8,191$
Resolution	14 bits	ADC part number	ADS62P49
Sample rate	250 MS/s	Input impedance	50 Ω , per connector
Bandwidth	500 MHz	Size	12.9 cm \times 2 cm \times 12.1 cm
Input range	1.23 V _{pk-pk}	Coupling	DC

5.1.2 Design procedures

The major steps involved in the design based on this platform are shown in Figure 5.2. It includes digitization of analog pulse, real-time digital pulse processing, data transfer from target to host PC and user interface design using LabVIEW. The analog pulses from PMT or preamplifier connected to a detector are digitized by the adapter module 5761 at sampling rate of 125 MSPS. These data are temporally stored in a target-scoped FIFO on the FPGA side after passing through the adapter module interface. They are then shaped with the traditional trapezoidal filtering method. Energy amplitude calculation and pile-up rejection are used to accurately obtain the energy information of each γ -ray pulse. The use of DMA engine is to transfer the energy data stored on a target-to-host DMA FIFO on the FPGA side to a target-to-host DMA FIFO on the host PC side. A real-time histogram of gamma energies will be displayed in the LabVIEW user interface as described below.

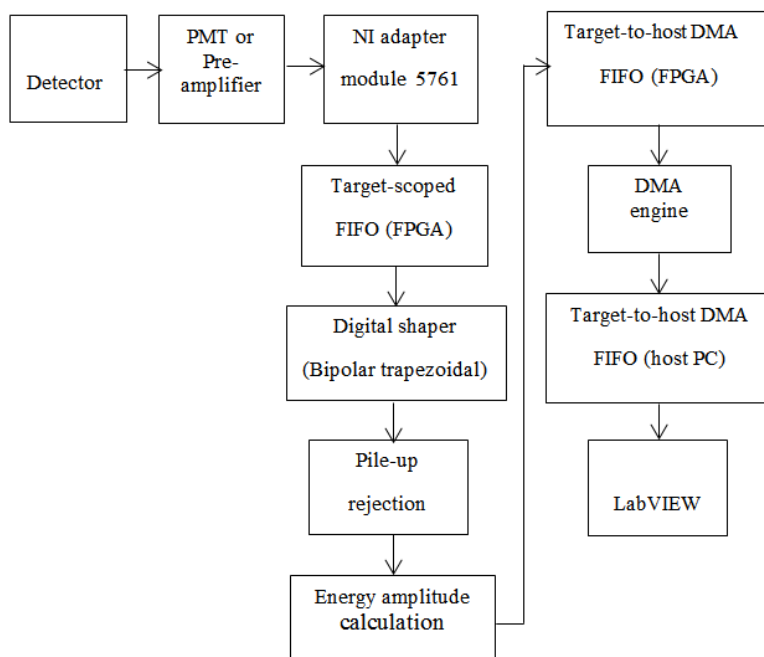


Figure 5.2 The block diagram of the customized digital γ -ray spectroscopy.

The measurement of γ -ray spectra with the customized γ -ray spectroscopy was controlled by the LabVIEW graphical user interface as shown in Figure 5.3. There are four analog input channels in the NI adapter module 5761. The AI Channel should be adjusted to the name of the analog input channel to which the signal from PMT or preamplifier was connected. The parameters of Record Size, Number of Elements, Timeout and Depth were used to avoid data overflow problems. The energy amplitude calculation and pile-up rejection were controlled by changing the values of the Cross1, Cross2 and Energy Threshold. The value of M was approximated by the product of the sampling rate used in the adapter module and the decay time constant of the analog input pulses.

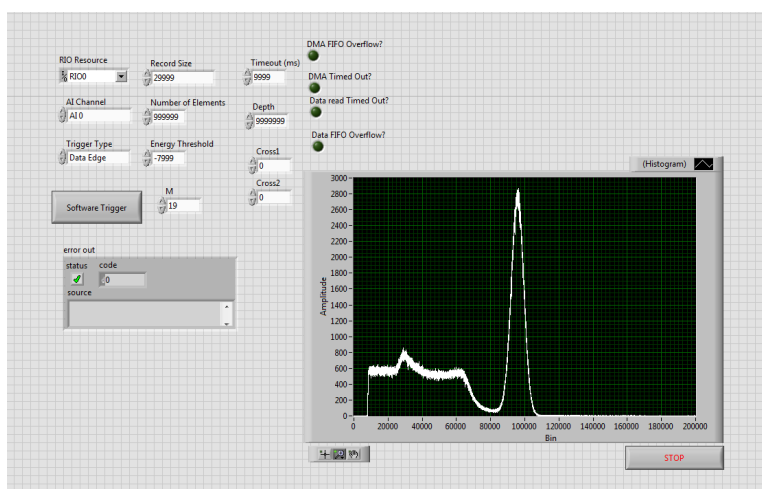


Figure 5.3 A LabVIEW graphical user interface for the customized γ -ray spectroscopy.

5.1.3 Results and discussion

The customized data acquisition system was tested using both a NaI detector and the HPGe detector. In the testing with the NaI detector, a Canberra Lynx system was also used for comparison purposes. The input count rate from the $1\ \mu\text{C}\ ^{137}\text{Cs}$ source used in the measurements was about 18 kcps. The shaping parameters used in the measurement with the two systems were $1\ \mu\text{s}$ respectively for rise time and flat top time. The energy resolution that the customized system achieved was 7% at 662keV as shown in Figure 5.4, which was comparable with that measured with the Canberra Lynx system, 6.8% at 662keV. A $5\ \mu\text{C}\ ^{137}\text{Cs}$ source was also used to test the capability of the system under a high input rate situation. The energy resolution was still around 7% at 662keV as shown in Figure 5.5.

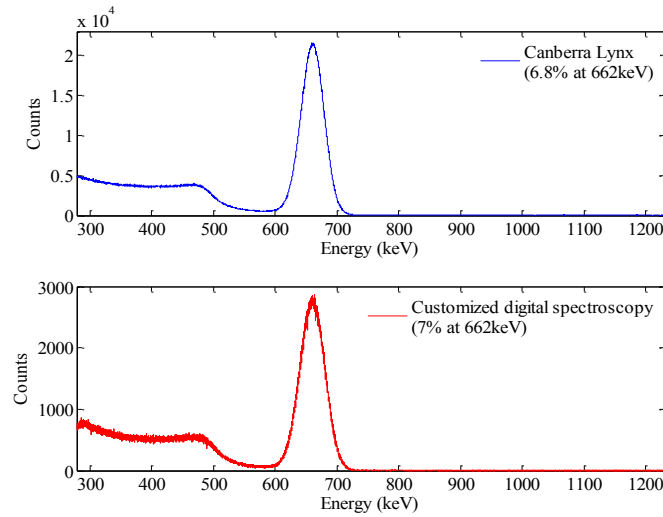


Figure 5.4 Comparison of the ^{137}Cs spectra measured with the Canberra Lynx system and the customized γ -ray spectroscopy ($1\ \mu\text{C}$).

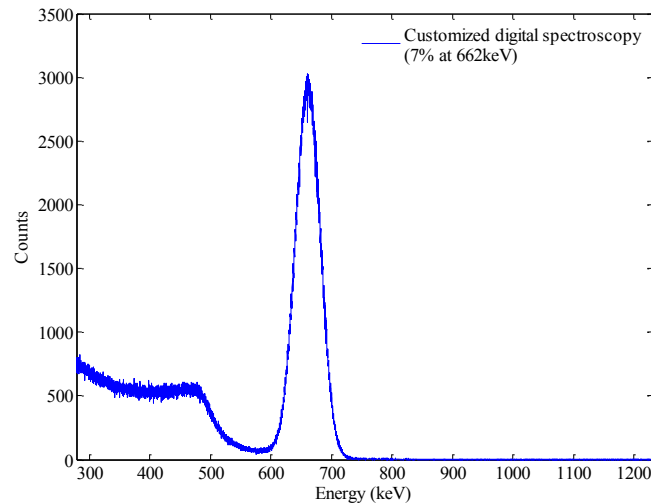


Figure 5.5 The ^{137}Cs spectra measured with the customized γ -ray spectroscopy ($5\ \mu\text{C}$).

Additional testing was then performed using the HPGe detector with the modified preamplifier. The same source $1\ \mu\text{C}\ ^{137}\text{Cs}$ was positioned close to the detector with input count rate of around 20 kcps. The energy resolution was 3.7 keV at 662 keV as shown in Figure 5.6. Under the same experimental setup and shaping parameters (rise time of 5.6 μs , flat top time of 0.8 μs), a better result (2.5 keV vs 3.7 keV @ 662 keV) was obtained from the data acquired with the NI PXIe-5122 in which its dynamic range could be adjusted as necessary through the LabVIEW program designed to control the data acquisition process. The degradation of energy resolution was due to the factor that the amplitude of the signal from the preamplifier was small ($\sim 20\ \text{mV}$) such that only a small portion of the ADC dynamic range of the adapter module was utilized. The energy resolution of the customized system could be improved by designing a signal conditioning board to utilize the full ADC range of the adapter module, maximizing the signal-to-noise ratio. Figure X shows the energy spectrum measured with the customized system using a $1\ \mu\text{C}\ ^{152}\text{Eu}$ source. As shown Figure 5.7, the major peak lines were identified in this spectrum.

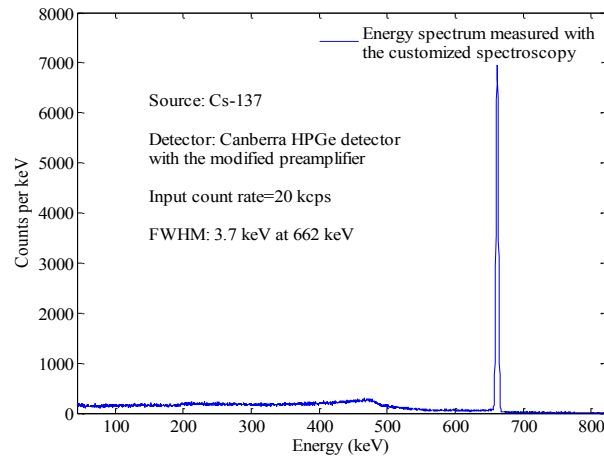


Figure 5.6 Energy spectrum measured with the customized system (HPGe detector).

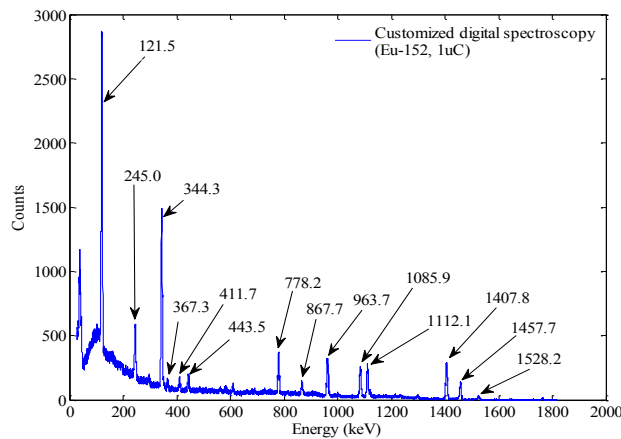


Figure 5.7 Energy spectra measured with the customized γ -ray spectroscopy developed on an HPGe platform (^{152}Eu).

5.2 Xilinx ML605 evaluation kit

5.2.1 Design flow

The hardware for the FPGA design included the Virtex-6 FPGA ML605 evaluation kit and 4DSP's FMC 151, as shown in Figure 5.8. More details about the hardware can be referred to <http://www.xilinx.com/products/boards-and-kits/ek-v6-ml605-g.html> and <http://www.4dsp.com/FMC151.php>.



Figure 5.8 Hardware ML605 evaluation kit and FMC151 for the FPGA design.

The FPGA design flow for the Virtex-6 FPGA is summarized as the following steps:

1. Creating wormhole, star and constellation with the StellarIP tool;
2. Generating an ISE project from the constellation;
3. Using the Xilinx System Generator to produce a VHDL file for DSP algorithm;
4. Downloading the bit file generated from the ISE foundation software to the Virtex-6 FPGA;
5. Optimizing the design to minimize source utilization.

In the design flow discussed above, star means a block that performs a specific task. Well-constructed stars can be reused in other FPGA designs. Wormhole is the connection between two stars. It comprises one or more signal channels in one or two directions. There are two types of wormholes used in this design, standard 4DSP wormhole and AXI4-streaming wormhole. The stars `sip_wh_in2axis_16b_out` and `sip_axis_16b_in2wh_out` are responsible for the data conversion between these two wormholes. A collection of stars is called constellation which can be used to create an ISE project for the FPGA design. An example of constellations created using the StellarIP tool is shown in Figure 5.9. The way the stars of the constellation communicate with each other is illustrated in Figure 5.10.

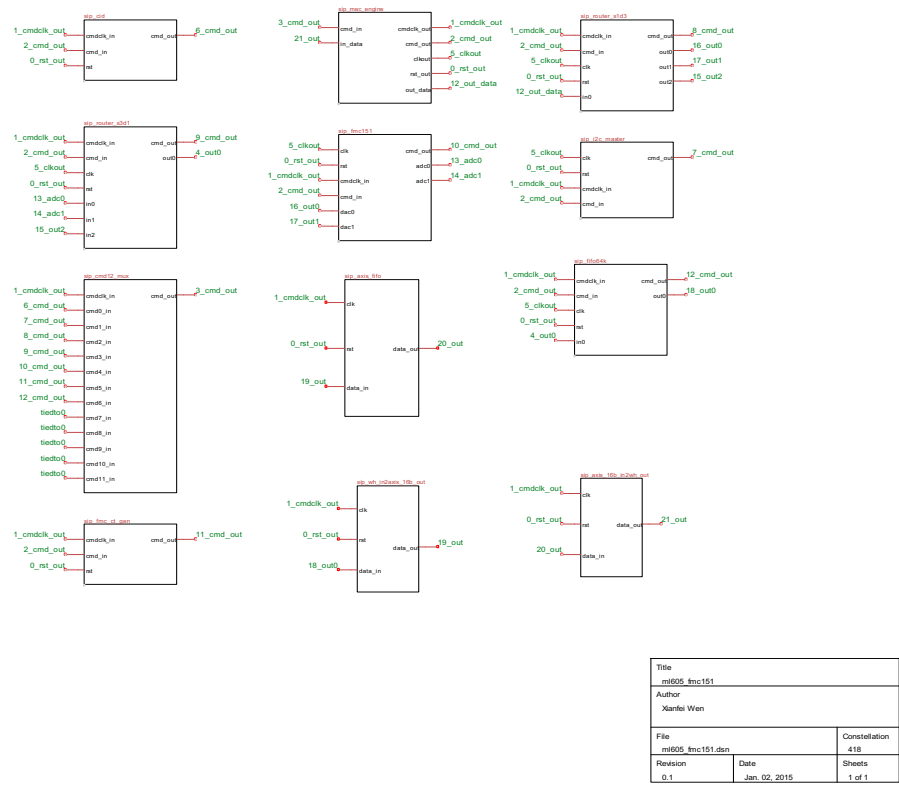


Figure 5.9 An example of constellation created with the StellarIP tool.

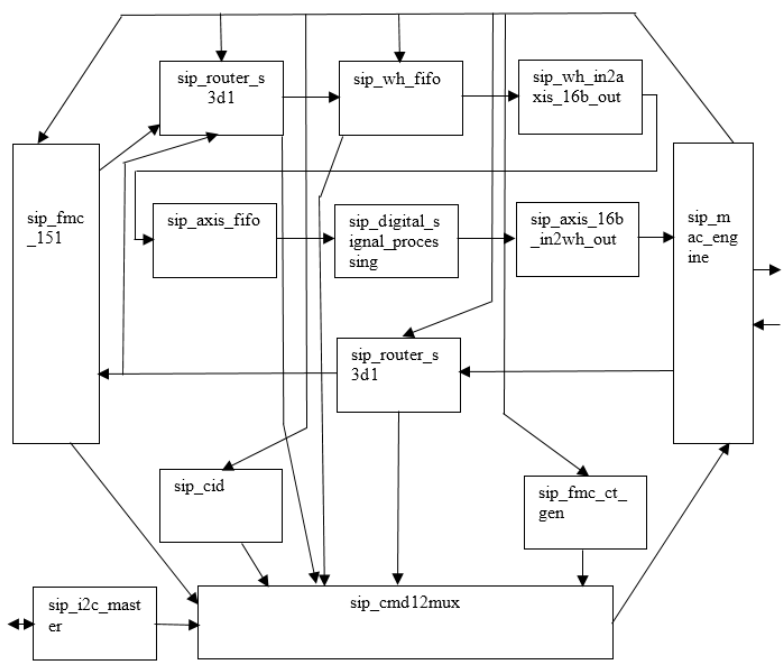


Figure 5.10 Illustration of the way the stars of a constellation communicate.

The functionality of each star is discussed below in detail.

sip_fmc_151: The sip_fmc_151 star controls the communication with the FMC 151 card. A small FIFO for each A/D channel and a waveform memory for each D/A channel are provided in this star to accommodate high bandwidth requirements. The sampled data from the two analog channels by the sip_fmc_151 star is sent to the sip_router_3d1 star. The data from the sip_router_1d3 star is transferred to the waveform memory for the D/A channels.

sip_router_3d1: This star routes data from the three inputs ports to the output port. Two of the three input ports are connected to the A/D channels. The other one is connected to one of the output channels of the sip_router_1d3 star.

sip_router_1d3: It routes data from the input port to the three output ports. One of the output ports is connected to the sip_router_3d1 star. The others are connected to the two D/A channels.

sip_cid: The sip_cid star holds all the information about the constellation created with the StellarIP tool. The information includes the constellation ID, star ID's address range, number of registers in each star, etc.

sip_mac_engine: The commands from the Ethernet MAC, such as read registers, are distributed by the sip_mac_engine star to transfer data to /from the host PC through the Ethernet cable. The global clock and reset signals are also generated by this star.

sip_cmd12mux: It merges the command outputs from all the stars to one single command and sends it to the sip_mac_engine star.

sip_wh_fifo: It routes data in the format of 64 bits from the input port to the output port. A FIFO in this star is used to buffer the data in case the data cannot be routed through fast enough.

sip_axis_fifo: It routes data in the format of 16 bits from the input port to the output port. A FIFO in this star is also used to buffer the data to avoid data loss.

sip_wh_in2axis_16b_out and **sip_axis_16b_in2wh_out:** They are two data conversion stars between two wormholes, 4DSP standard wormhole and AXI4-streaming wormhole. The 4DSP standard wormhole has 64 bits data with, where each data consists 4 continuous samples from one single analog channel. The data needs to be converted such that each data containing one sample from an A/D channel is ready to be sent for the signal processing. The protocol difference between the two types of wormholes is also addressed in the stars.

sip_digital_signal_processing: Digital signal processing, such as traditional trapezoidal shaping, can be implemented in this star.

sip_i2c: This star is used to monitor the voltage and temperature of the FMC 151 card.

After a constellation is accurately created, it is ready to generate an ISE project file with the StellIP tool. An example of ISE project produced with this tool is shown in Figure 5.11. There are several benefits from using this tool in FPGA design. First, a C/C++ head file containing the information about the constellation and stars is automatically generated. Second, an ISE project file, a top level VHDL file and a UCF file are also created to speed up the design cycle. Also, it is easy to separate the FPGA design into different stars which can perform specific functionality when creating a new constellation.

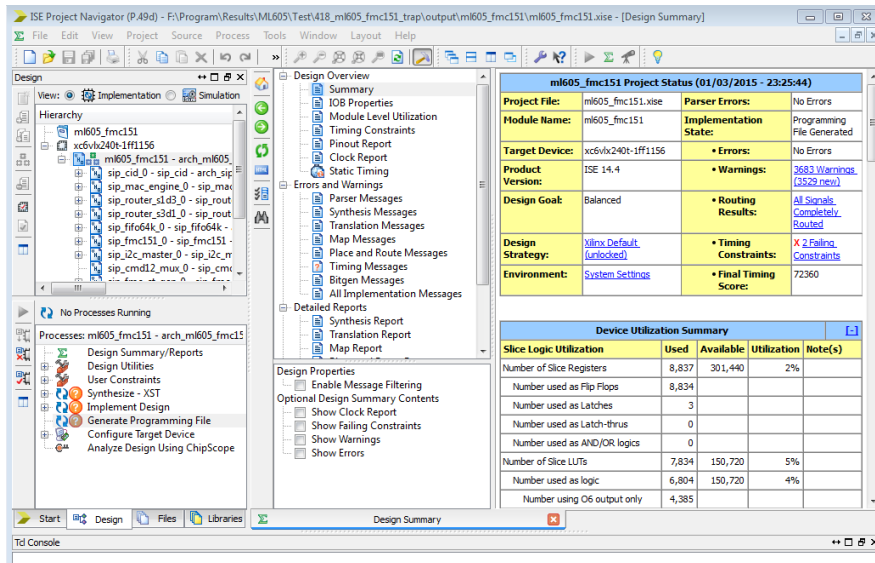


Figure 5.11 An example of ISE project generated using the StellarIP tool.

Although a system designer typically uses hardware description languages (e.g. VHDL or Verilog) to program FPGAs, the developer whose focuses are on the algorithms prefers a high-level descriptions language (e.g. C). It is usually a time-consuming process to translate an algorithm described in a language such as Matlab or C to HDL. The System Generator for DSP from Xilinx, Synplify DSP from Synopsys and the HDL Coder from Mathworks provide an easy way to implement advanced algorithms on FPGA. They can enable the use of model-based environment within the Mathworks Simulink for FPGA design. The Xilinx System Generator for DSP is used in this design. It is not necessary to have enough design experience with HDL when using the System Generator. Hundreds of blocks included in the Xilinx blockset are available to designers. These blocks provide an intuitive way to describe an algorithm even having certain complexity. VHDL and Verilog code generation from the System Generator are available for Virtex-4, Virtex-5, Virtex-6, Spartan-3, Spartan-3E and Spartan-6 FPGAs. The HDL codes are automatically bit-accurate and cycle-accurate generated. The gateway in and gateway out blocks make it easy to integrate these HDL files into an ISE project. A UCF file is also created by the System Generator. Figure 5.12 shows a model for the traditional trapezoidal filter built within the Mathworks Simulink. The three blocks as shown in Figure 5.12, System Generator token,

gateway in and gateway out blocks are necessary in every simulink model. The VHDL file was imported to the sip_digital_signal_processing star of the ISE project. As shown in Figure 5.13, the traditional trapezoidal filter was successfully implemented on the Virtex-6 FPGA in real-time using the FPGA design flow described above.

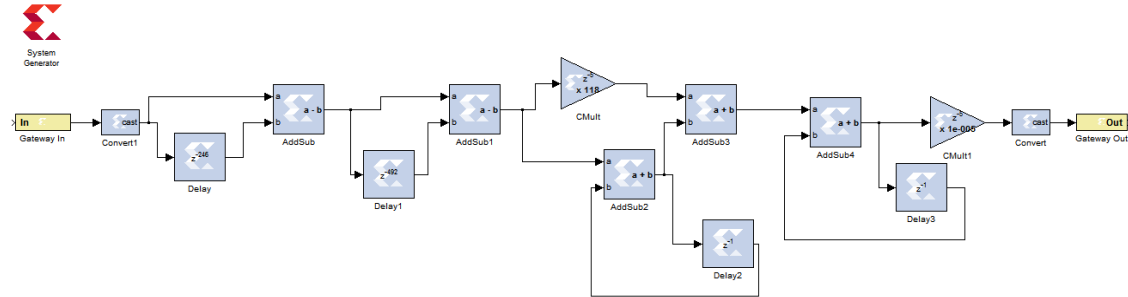


Figure 5.12 A simulink model for the traditional trapezoidal filtering.

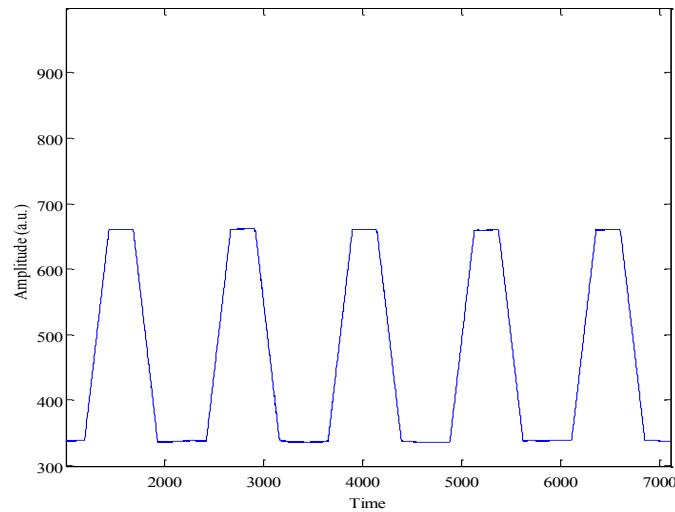


Figure 5.13 The traditional trapezoidal shaping on the Virtex-6 FPGA in real-time.

5.2.2 Results and discussion

The FPGA development based on the ML605 evaluation board and FMC 151 was tested using a NaI detector. The model number of the detector was Canberra Model 802. The size of the crystal was 2" by 2". The high voltage was provided by a NIM bin and set at positive 1500 V. In the measurements, a $5\mu\text{Ci } ^{137}\text{Cs}$ source was kept close to the detector to have an input count rate of ~ 18 keps. The anode signal was connected to the ADC channel B of the FMC 151. The signal was sampled at sampling rate of ~ 250 MSPS. The digitized data was temporarily stored in a small FIFO in the FMC 151 and then transferred to the evaluation board. The trapezoidal filter was implemented in the FPGA to extract energy information of gamma rays. The rise and flat top times used in the trapezoidal filtering were both set at $1\ \mu\text{s}$. The energy information was

transferred to PC via an Ethernet cable and stored in a hard drive in the format of text file. Figure 5.14 shows the energy spectrum measured using this customized system. As shown in Figure 5.14, reasonable energy resolution (7 % @ 662 keV) and Gaussian peak were achieved.

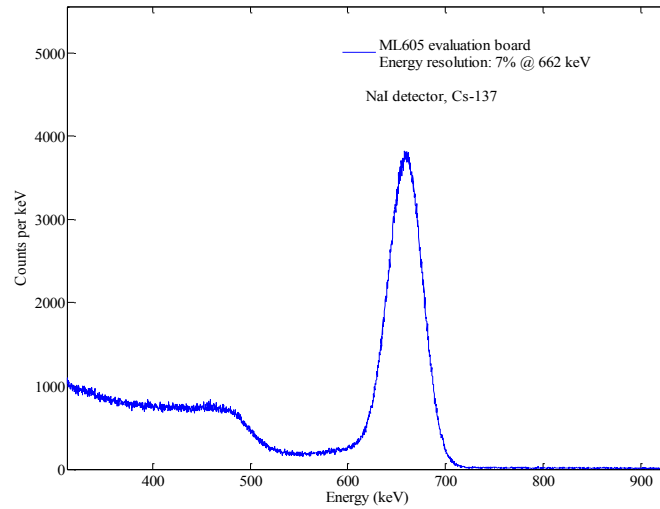


Figure 5.14 Energy spectrum measured with the FPGA platform based on the ML605 evaluation board and FMC 151.

6 Conclusions

In homeland security and nuclear safeguards applications, non-destructive techniques to identify and quantify special nuclear materials are in great demand. Although nuclear materials naturally emit characteristic radiation, their intensities and energies are normally low. Furthermore, these γ -rays could be buried in large background and intentionally shielded. Photofission technique based on measurement of delayed γ -rays was demonstrated in this work as an effective approach. High-energy delayed γ -rays ($E_\gamma > 3$ MeV) were measured in between linac pulses using independent data acquisition systems. A list-mode system was also developed to measure low-energy delayed γ -rays after irradiation. System design based on such technique is largely dependent on nuclear data, such as fission product yields. Although fission yields for neutron-induced fission of most nuclear materials (e.g. ^{232}Th , ^{235}U , ^{238}U , ^{239}Pu) were well studied and have already been available in various nuclear databases, such as the Evaluated Nuclear Data File (ENDF), published data on photofission product yields is rare. Photofission product yields of ^{238}U and ^{239}Pu were determined based on the delayed γ -ray spectra measured in between linac pulses and after irradiation. These photofission yields could contribute to nuclear data library. They can also provide valuable information for designing assay systems based on photonuclear techniques in homeland security and nuclear safeguards applications. The experimental outcomes were also compared with Monte Carlo simulation results. It was observed that some peak lines were measured in the experiments, however, they were not predicted by simulation or over-predicted/under-predicted. Also, some lines that were predicted by simulation were not observed in the measurements. The comparison demonstrated the capabilities and limitations of current available simulation packages and provided guidance for system design based on active interrogation techniques.

A major challenge in active interrogation is to perform spectroscopy measurements with high-resolution high-throughput at ultra-high rate. The two-folded approach was shown to effectively address this challenge. First, the modification to the HPGe preamplifier improved its high-rate performance in a pulsed photonuclear environment. At high linac repetition rate (e.g. 125 Hz), a standard preamplifier as used in this study would be paralyzed for $\sim 70\%$ of the time. Instead, a maximum live time of 66% can be achieved in theory after modification, due to the much reduced recovery time. Also, the significant reduction of baseline shift could be beneficial to many high-rate applications. For example, in used nuclear fuel assay, the input count rate can often reach 10^6 cps or higher. Thus a preamplifier with nominal tail time (i.e. 50 μs) would be easily saturated. However, as a result of the reduced tail time, the modified preamplifier could potentially be used to perform spectroscopy measurement and provide valuable information about used fuel assemblies. Second, the advanced digital pulse processing algorithms including the template-matching method, Kalman filtering, time-variant trapezoidal filtering and de-randomization technique were demonstrated to significantly improve throughput rate without large sacrifice in energy resolution at ultra-high input count rate. For example, using the de-randomization technique, energy resolution of 2.5 keV at 662 keV was achieved at input count

rate of 100 kcps. The output count rate was also 100 kcps since pile-up correction was not performed. The algorithm was also applied to the 300 kcps HPGe data. Without pile-up rejection or recovery, only slight degradation in energy resolution was observed (3.1 keV vs 2.5 keV @ 662 keV). Two customized digital gamma spectroscopy systems were developed in real-time on FPGAs (National Instruments FPGA module and Xilinx evaluation kit). The traditional trapezoidal filter was used in these system designs. With the advanced pulse processing algorithms and the FPGA platforms, real-time high-resolution high-throughput gamma spectroscopy systems could be developed. This could be an area for future study on photofission techniques for used nuclear fuel assay or many high-rate applications.

References

1. Nuclear nonproliferation, United States Government Accountability Office, 2005.
2. K. Murakami, Nuclear Safeguards Concepts, Requirements, and Principles applicable to Nuclear Security, July 2012.
3. IAEA Safeguards agreements and additional protocols, "Non-proliferation of nuclear weapons & nuclear security," 2005.
4. D. Reilly, et al., Passive Nondestructive Assay of Nuclear Materials, NUREG/CR-5550, 1991.
5. T. Gozani, "Active nondestructive assay - principles and applications," NUREG/CR-0602, 1981.
6. T. Gozani, "A review of neutron based non-intrusive inspection techniques.
7. P. Kerr, et al., "Active detection of small quantities of shielded highly-enriched uranium using low-dose 60-keV neutron interrogation," UCRL-CONF-223845, 2006.
8. M. Gmar et al., "Use of delayed gamma spectra for detection of actinides (U, Pu) by photofission," *Nucl. Instr. Meth. Phys. Res. A*, vol. 422, pp. 841-845, 1999.
9. D. Norman, et al., "Time-dependent delayed signatures from energetic photon interrogations," *Nucl. Instr. Meth. Phys. Res. B*, vol. 261, pp. 316-320, 2007.
10. J. Jones, et al., "Photonuclear-based, nuclear material detection system for cargo containers," *Nucl. Instr. Meth. Phys. Res. B*, vol. 241, pp. 770-776, 2005.
11. D. Beddingfield, et al., "Identification of fissile materials from fission product gamma-ray spectra," *Nucl. Instr. Meth. Phys. Res. A*, vol. 417, pp. 405-412, 1998.
12. T. Gozani, "Fission signatures for nuclear material detection," *IEEE Trans. Nucl. Sci.*, vol. 56, pp. 736-741, 2006.
13. K. Jordan, et al., "Detection of ^{235}U in hydrogenous cargo with differential die-away analysis and optimized neutron detectors," *Nucl. Instr. Meth. Phys. Res. A*, vol. 579, pp. 388-390, 2007.
14. R. Marrs, et al., "Fission-product gamma-ray line pairs sensitive to fissile material and neutron energy," *Nucl. Instr. Meth. Phys. Res. A*, vol. 592, pp. 463-471, 2008.
15. C. Hollas, et al., "Analysis of fissionable material using delayed gamma rays from photofission," LA-UR-86-3363, 1986.
16. D. Wehe, et al., "Observation of ^{238}U photofission products," *IEEE Trans. Nucl. Sci.*, vol. 53, pp. 1430, 2006.
17. http://en.wikipedia.org/wiki/Nuclear_fission_product
18. M. Kinlaw, et al., "Fissionable isotope identification using the time dependence of delayed neutron emission," *Nucl. Instr. Meth. Phys. Res. A*, vol. 562, pp. 1081-1084, 2006.
19. H. Rennhofer, et al., "Detection of SNM by delayed gamma rays from induced fission," *Nucl. Instr. and Meth. A*, vol. 652, pp. 140-142, 2011.
20. Nuclear Physics and Reactor Theory, DOE Fundamentals Handbook, Volume 2, 1993.
21. J. Meason, et al., "Photofission of ^{238}U induced by 17.5-MeV monoenergetic gamma rays," *Phys. Rev.* 142, 1966.

22. E. Jacobs, et al., "Product yields for the photofission of ^{238}U with 12-, 15-, 20-, 30-, and 70-MeV bremsstrahlung," *Phys. Rev. C* 19, 1979.
23. E. Jacobs, et al., "Product yields for the photofission of ^{235}U with 12-, 15-, 20-, 30-, and 70-MeV bremsstrahlung," *Phys. Rev. C* 21, 1980.
24. F. Carrel, et al., "New experimental results on the cumulative yields from thermal fission of ^{235}U and ^{239}Pu and from photofission of ^{235}U and ^{238}U induced by bremsstrahlung," *IEEE Trans. Nucl. Sci.*, vol. 58, pp. 2064-2072, 2011.
25. MCNPX Version 2.7.0 User's Manual, LA-CP-11-00438, 2011.
26. E. Barat, et al., "A bimodal Kalman smoother for nuclear spectrometry," *Nucl. Instr. Meth. Phys. Res. A*, vol. 567, pp. 350-352, 2006.
27. E. Barat, et al., ADONIS: a new system for high count rate HPGe spectrometry, *IEEE Nuclear Science Symposium Conference Record*, N30-6, 2006.
28. E. Barat, et al., "ADONIS: A New Concept of X/Gamma Pulse Analyzer," *ANIMMA Conference Record*, N210, 2009.
29. B. VanDevender, et al., "High-purity germanium spectroscopy at rates in excess of 10^6 events/s," *IEEE Trans. Nucl. Sci.*, vol. 61, pp 2619-2627, 2014.
30. J. Jones, "Detection of pulsed bremsstrahlung-induced prompt neutron capture gamma rays with a HPGe detector," *Proc. SPIE* 2867, 1997.
31. M. James, "MCNPX 2.7.X - new features being developed," *IEEE/NSS*, Orlando, FL, 2009.
32. V. Jordanov, et al., "Digital techniques for real-time pulse shaping in radiation measurement," *Nucl. Instr. Meth. Phys. Res. A*, vol. 353, pp. 261-264, 1994.
33. G. Gilmore, *Practical Gamma-ray Spectrometry*, John Wiley & Sons, 2nd Edition, 2008.
34. V. Jordanov, "Deconvolution of pulses from a detector-amplifier configuration," *Nucl. Instr. and Meth. A*, vol. 351, pp. 592-594, 1994.
35. V. Jordanov, "Exponential signal synthesis in digital pulse processing," *Nucl. Instr. and Meth. A*, vol. 670, pp. 18-24, 2012.
36. V. Jordanov, "Digital pulse de-randomization for radiation spectroscopy," Patent No.: US 6,369,393 B1, 2002.
37. R. Schafer, "What Is a Savitzky-Golay Filter?," *IEEE signal processing magazine*, 2011.

Appendices

A Publications and Presentations

Publications

1. Xianfei Wen, Haori Yang, "Photofission product yields of ^{238}U and ^{239}Pu with 22-MeV bremsstrahlung," *Nucl. Instr. Meth. Phys. Res. A*, 2016 (in revision).
2. Xianfei Wen, Dante Nakazawa, Mat Kastner, Jason Pavlick, Haori Yang, "Evaluation of a modified HPGe preamplifier for high-rate spectroscopy measurements in a pulsed photonuclear environment," *Nucl. Tech.*, vol. 194, 2016.
3. Xianfei Wen, Haori Yang, "Study on a digital pulse processing algorithm based on template-matching for high-throughput spectroscopy," *Nucl. Instr. Meth. Phys. Res. A*, vol. 784, pp. 269-273, 2015.
4. Xianfei Wen, John Kavouras, Dante Nakazawa, Haori Yang, "Simulation and measurement of delayed γ -rays after photon-induced fission," *Nucl. Instr. Meth. Phys. Res. A*, vol. 729, pp. 781-787, 2013.
5. John Kavouras, Xianfei Wen, Daren Norman, Dante Nakazawa, Haori Yang, "Pulsed photofission delayed gamma ray detection for nuclear material identification," *IEEE Nuclear Science Symposium Conference Record*, N1-35, 2012.

Presentations

1. Xianfei Wen, Dante Nakazawa, Haori Yang, "Simulation and measurement of cumulative photofission yields of ^{238}U and ^{239}Pu ," *IEEE Nuclear Science Symposium and Medical Imaging Conference*, San Diego, California, 2015.
2. Xianfei Wen, "Measurement and simulation of delayed γ -rays from photofission," *invited talk*, Dartmouth College, Hanover, New Hampshire, 2015.
3. Xianfei Wen, Haori Yang, "Active interrogation technique based on photofission for used nuclear fuel assay," *Oregon State University Engineering Research Expo*, Portland, Oregon, 2015.
4. Xianfei Wen, Dante Nakazawa, Mat Kastner, Haori Yang, "A high-throughput high-resolution gamma spectroscopy system for the measurement of delayed γ -rays after photon-induced fission," *IEEE Nuclear Science Symposium and Medical Imaging Conference*, Seattle, Washington, 2014.
5. Xianfei Wen, Dante Nakazawa, Haori Yang, "Study on a digital pulse processing algorithm based on template-matching for high-throughput spectroscopy," *Symposium on Radiation Measurements and Applications*, Ann Arbor, Michigan, 2014.
6. Xianfei Wen, John Kavouras, Haori Yang, "Active interrogation techniques for special nuclear material detection," *CANBERRA Users' Group Meeting*, Salt Lake City, Utah, 2013.
7. Haori Yang, John Kavouras, Xianfei Wen, Dante Nakazawa, Daren Norman, "Pulsed photofission delayed gamma ray detection for nuclear material identification," *IEEE Nuclear Science Symposium and Medical Imaging Conference*, Anaheim, California, 2012.